Ollscoil na hÉireann, Corcaigh

National University of Ireland, Cork

Modelling and growth of boron containing alloys of III-Nitrides for their application in the Ultraviolet range

Thesis presented by

Thomas O'Connor, B.Sc.

for the degree of

Doctor of Philosophy

University College Cork

School of Engineering

Head of School/Department: Prof. Jorge Oliveira

Supervisor: Prof. Peter James Parbrook

Co-supervisor: Dr. Stefan Schulz

2023

TABLE OF CONTENTS

Declaration

This is to certify that the work I am submitting is my own and has not been submitted for another degree, either at University College Cork or elsewhere. All external references and sources are clearly acknowledged and identified within the contents. I have read and understood the regulations of University College Cork concerning plagiarism and intellectual property.

Name: THOMAS O'CONNOR

Signature: _____

Date: _____

Acknowledgements

First and foremost, I would like to thank my supervisor Prof. Peter Parbrook for giving me the opportunity to pursue a PhD in the III-Nitride group at Tyndall National Institute. I truly appreciate all of his time, guidance and unwavering support throughout my past four years. It truly was an honour working with a person of his calibre. To my co-supervisor Dr. Stefan Schulz, I want to express my gratitude for his advice and encouragement which has been indispensable to me throughout my journey. I would like to give a special thanks to Dr. Vitaly Zubialevich, one of the most hardworking, intelligent and interesting people I have ever met and for all of his support during my PhD.

Many thanks to all my group members that I have been working with throughout the four years for their help and support. Especially Dr. Pietro Pampili, Sandeep Singh, Peter Milner and Robert Finn.

I would like to thank Dr. Miryam Arrendondo and Dr. Praveen Kumar at Queen University Belfast for their contribution and collaborations, particularly for the transmission electron microscope measurements of our samples.

I would also like to thank Dr. Fatima Gunning and Dr. Robert Sheehan for allowing me to work with her group during the summers of my undergrad and for making me realise the opportunities that were available to me.

Next, I would like to thank my family. I would not be at this point today if it were not for my parents. They supported me and my education throughout my life for which I am incredibly grateful. My sister Helena, thanks for all the support and encouragement over the last few years.

I would also like to thank my friends both from Cork and Kilkenny. In particular Craig, Alex, Glav, Danny, Cian, Jack and Connor. For all the distractions with hiking, cycling, mountain biking, running, boxing, gigging and other events we were involved in.

Lastly but not least, I would like to express my gratitude to the Science Foundation Ireland for funding my research.

Abstract

III-Nitride semiconductor materials such as AlN, GaN, InN and their alloys, can emit light from the infrared to the deep ultraviolet region. Strong polarisation fields and significant differences in the optimum growth conditions for these binary compounds, make it difficult to understand these materials. BN is a relatively new material in this group which has the potential to improve strain engineering, increase the flexibility of bandgap engineering along with reducing the overall polarisation charge when alloyed with other III-Nitride materials.

In this work, the Schrödinger equation was solved for a single quantum well system consisting of $B_xGa_{1-x}N$/ $Al_yGa_{1-y}N$ and to understand the impact BN had on the wavefunction overlap along with the emission energy.

Incorporation of wz-BN with GaN thin layers appears to prevent plastic relaxation of these layers with respect to their substrate and at higher temperatures resulting in phase separation of the material. A mechanism for recognising this clustering of boron atoms in the material is proposed using X-ray diffraction is presented.

B(Al)GaN/AlGaN multiple quantum wells (MQWs) were grown and excited by photoluminescence (PL), and emission wavelengths between 328-349 nm were obtained. The incorporation of the lowest amounts of wurtzite-BN appears to result in a redshift and an improvement in the PL emission intensity of the material. However, this benefit comes at the cost of nanovoids/ nanopits forming in the material under the growth conditions used. Nanomasking effects dominate for the smallest levels of BN incorporation, with higher degrees of disorder, propagating into the barrier regions, being observed as the B/III ratio increased, as well as a reduction in the PL intensity. To our knowledge, this is the first report of both a ternary and quaternary B(Al)GaN/AlGaN MQW stacks grown by MOCVD on a *c*-plane AlN/sapphire templates for UV emission.

List of Publications:

- Peter. Milner, Vitaly Z. Zubialevich, Thomas O'Connor, Davinder Singh, Brian Corbett and Peter J. Parbrook . "*BAlGaN LED emitting at 350 nm*"

Presentations (Oral and Poster):

- Thomas O'Connor, Vitaly Zubialevich, Stefan Schulz, Peter Parbrook. "*III-Nitride materials containing Boron alloys for UV emission*", **IPIC Industry Workshop Day**, University College Cork, March **2020** (Poster)
- Thomas O'Connor, Vitaly Zubialevich, Stefan Schulz, Peter Parbrook. "*Prospects for Boron containing alloys for UV-LEDs*", **IPIC Industry Workshop Day**, Online, March **2021** (Poster)
- Thomas O'Connor, Vitaly Zubialevich, Stefan Schulz, Peter Parbrook. "*Prospects for Boron containing alloys for UV-LEDs*", **Photonics Ireland**, Online, June **2021** (Poster)
- Thomas O'Connor, Vitaly Zubialevich, Stefan Schulz, Peter Parbrook. "*Prospects for Boron containing alloys for UV-LEDs*", **Photonics Integration Advanced Data Storage (PIADs) Conclave**, Online, June/July **2021** (Poster, Winner)
- Thomas O'Connor, Vitaly Zubialevich, Praveen Kumar, Miryam Arredondo-Arechavala, Stefan Schulz and Peter Parbrook. "*Effect of boron incorporation on the luminescence and structural properties of $B_xAl_yGa_{1-x-y}N$/ AlGaN MQWs for UV emitters*", **Tyndall Poster Competition**, Tyndall National Institute, July **2022** (Poster)
- Thomas O'Connor, Vitaly Zubialevich, Stefan Schulz and Peter Parbrook. "*Growth and characterisation of MQWs containing BN with AlGaN barrier*", **Photonics Integration Advanced Data Storage (PIADs) Conclave**, Glasgow, Scotland, June **2022**
- Thomas O'Connor, Pietro Pampili, Vitaly V. Zubialevich, Peter Parbrook. "*Optical, strain and surface analysis of BGaN thin films grown by MOCVD on GaN and AlN templates*", **International Conference on Metal Organic Vapor Phase Epitaxy (ICMOVPE XX),** Stuttgart, Germany, July **2022**

- Thomas O'Connor, Vitaly Zubialevich, Stefan Schulz, Peter Parbrook. "*Growth and characterisation of MQWs of BGaN with AlGaN barrier*", **European Material Research Society (E-MRS)**, Warsaw, Poland, September **2022** (Awarded UKNC Scholarship)
- Thomas O'Connor, Vitaly Zubialevich, Peter Parbrook. "*Growth and characterisation of MQWs of BAlGaN with AlGaN barrier*", **International Workshop on Nitride Semiconductors (IWN)**, Berlin, Germany, September **2022**
- Thomas O'Connor, Vitaly Zubialevich, Praveen Kumar, Miryam Arredondo, Stefan Schulz and Peter Parbrook. "*Properties of $B_xAl_yGa_{1-x-y}N$/ AlGaN multiple quantum wells for ultraviolet emission*", **United Kingdom Nitride Consortium (UKNC)**, Bristol, United Kingdom, January **2023**
- Thomas O'Connor, Vitaly Zubialevich, Praveen Kumar, Miryam Arredondo, Stefan Schulz and Peter Parbrook. "*Effect of boron incorporation on the luminescence and structural properties of $B_xAl_yGa_{1-x-y}N$/AlGaN MQWs for UV emitters*", **SPI Photonics West**, San Francisco, California, USA, January/February **2023**

Abbreviations

CBO	Conduction band offset
CCD	Charge coupled detector
ccp	cubic closed packed
CVD	Chemical vapor deposition
DLD	Deep level defect
FDM	Finite difference method
FWHM	Full-width half maximum
H	Hexagonal
HAADF	High annular angle dark field
hcp	hexagonal closed packed
HH	Heavy hole
HVPE	Halogen vapor phase epitaxy
IQE	Internal quantum efficiency
LED	Light emitting diode
LH	Light hole
LT	Low temperature
MBE	Molecular beam epitaxy
MO	Metalorganic
MOCVD	Metalorganic chemical vapor deposition
MOVPE	Metalorganic vapor phase epitaxy
MQW	Multiple quantum well
NBE	Near band edge
PL	Photoluminescence
PLE	Photoluminscence excitation
PMT	Photomultiplier tube
$\boldsymbol{P_{pz}}$	Piezoelectric polarisation
$\boldsymbol{P_{sp}}$	Spontaneous polarisation
QB	Quantum barrier
QCSE	Quantum confined stark effect
QW	Quantum well
RHEED	Reflection high energy electron diffraction

RMS	Root mean squared
RSM	Reciprocal space map
RT	Room temperature
SEM	Scanning electron microscope
TE	Transverse electric
TEB	Triethylboron
TEM	Transmission electron microscope
TM	Transverse magnetic
TMAl	Trimethylaluminium
TMGa	Trimethylgallium
UV	Ultraviolet
VBO	Valence band offset
WZ	Wurtzite
XRD	X-ray diffraction
ZB	Zincblende

1 INTRODUCTION

1.1 Application and demand for Ultraviolet LEDs

According to the analysis of the market trends, the demand for ultraviolet (UV) devices is increasing exponentially as seen in **Figure 1-1**.

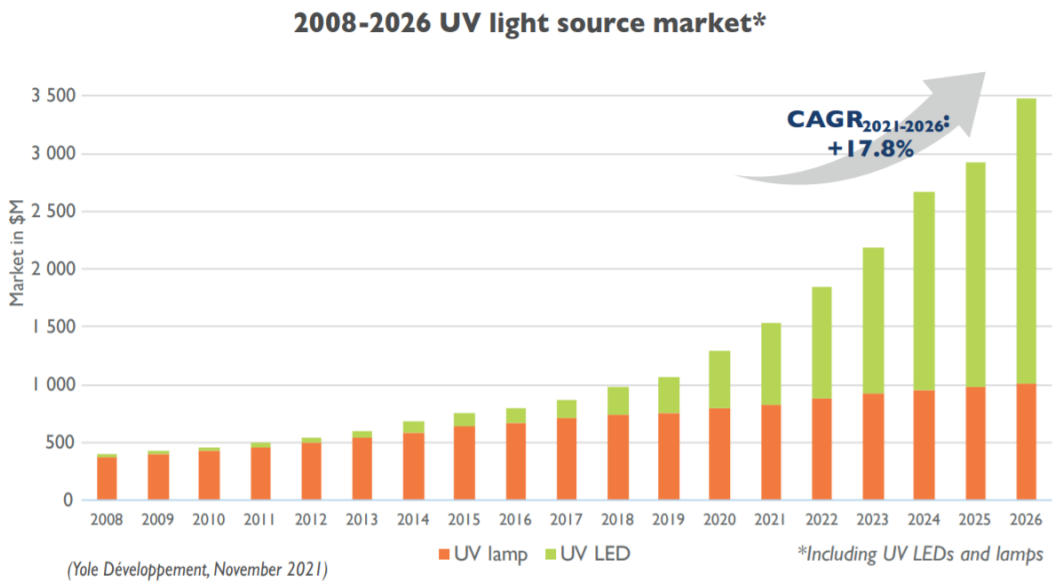

Figure 1-1. 2008-2026 UV LED Device Market Size (Chip & Package) in $M[1].

In 2008 the overall UV market was worth $400 million, with $20 million associated with UV LEDs. By 2019 the $1 billion milestone was reached for UV LEDs alone, a sharp increase due to the demand for UV LEDs for curing and disinfection applications. The COVID-19 pandemic created further demand for these devices, leading to an increase of 30% in just one year. The market has a projected estimate of around $3.5 Billion in 2026.

The market is no longer dominated by traditional UV sources such as mercury, xenon and deuterium lamps. Traditional UV lamps have many disadvantages when compared to UV-LEDs; they are large and bulky, require large operating voltage, have short lifespan, produce multiple wavelength emission peaks and require a turn-on/heat-up time. UV-LEDs in contrast are extremely robust; they are compact, environmentally friendly, have much longer lifetimes and can be turned on and off instantaneously without warm-up time. Although, the future for the UV LED industry is incredibly

bright, a significant amount of work is required to increase the optical power efficiency and reduce the price of these devices. The full potential of UV LEDs is yet to be reached as there are many challenges that they possess in their growth and fabrication. Some of these challenges will be discussed in this thesis over the traditional sources, making them a key area of research.

In today's world, there has been a large increase in the demand for an efficient and compact ultraviolet emitting device. The UV spectrum can be divided into three regions; UVA (400 - 320 nm), UVB (320 - 280 nm) and UVC (< 280 nm), and each of these regions contains different applications as seen in **Figure 1-2**.

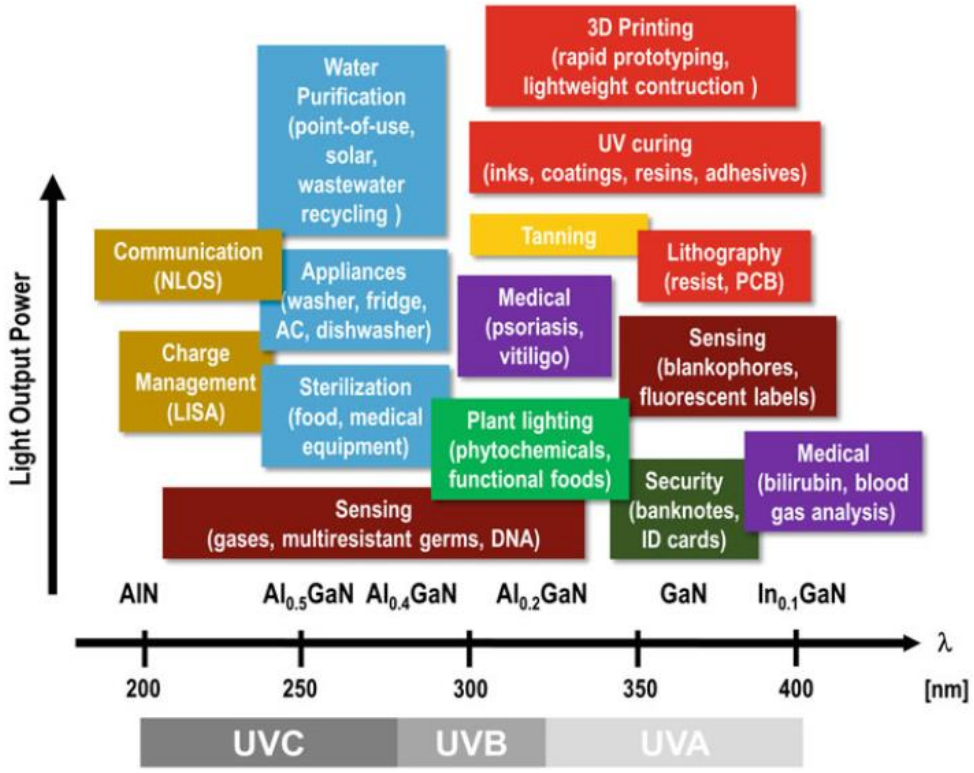

Figure 1-2. Application of Ultraviolet devices[2].

In the longer wavelength UVA region (λ>365 nm) applications include curing of inks, paints, coating resins, polymers and adhesives as well as 3D-printing for rapid prototyping and lightweight construction[2]. These commercial LEDs are already available with reasonable performance as this was the main market share for UV LEDs in 2008-2018. However, below 365 nm the challenges to produce an efficient UV LED increases dramatically. There are many significant applications for such a device in

the biomedical and biological areas, where the biomolecules such as flavins, elastin, collagen, porphyrins, lipopigments and nicotinamide adenine dinucleotide contain strong absorption bands in the UVA range[3].

A device operating in this region can induce fluorescence through the absorption of UV radiation, thus indicating the presence of the molecule[4]. Other applications for UVA emitters include the detection of blankophores and fluorescent labels as well as blood gas analysis and light therapy[5].

In the UVB region, in addition to the biofluorescence of molecules such as pyridoxine and tryptophan (also seen in **Figure 1-2**), some other key applications include phototherapy, in particular the treatment of skin diseases such as psoriasis and vitiligo[6,7]. A UVB LED emits in a narrow spectral range thus providing a potentially effective treatment of the condition without damage from exposure to shorter wavelengths. UVB LEDs are also used in the horticulture sector for plant growth lighting. The UVB LEDs can interact with the plant's metabolism and photosynthesis rate depending on the type and strain of the plant[8].

Disinfection of drinking water and wastewater treatment is the highest volume application for emitters in the UVC spectral range. The effective disinfection of water requires a wavelength between the UVB and UVC region (~250-282 nm)[9], which currently uses chlorine to kill bacteria and fluorine to prevent tooth decay. Chemicals such as chlorine are carcinogenic and thus harmful to humans. Also, the approach of adding chemicals does not kill all parasites such as Giardia and Cryptosporidium, both of which can cause diarrhoea and lead to death[10]. By using a UV source, the use of these harmful chemicals can be avoided while the bacteria and parasites can still be inactivated. UV light is absorbed by the water molecules and deactivates the micro-organisms by disrupting their DNA and preventing them from reproducing. Since the micro-organisms are unable to reproduce, they are unable to cause infection. The demand for efficient germicidal lamps has increased with the discovery of Severe Acute Respiratory Syndrome Coronavirus-2 (SARS-CoV-2) also commonly known as Covid-19. The spreading of the micro-organisms in the air can be prevented in a similar method as previously discussed. In addition, the sterilization of medical equipment,

home appliances and various surfaces in the food industry would benefit greatly from UVC-LEDs.

Data storage is also another key application for a device operating in the UV. CD, DVD and Blu-ray discs all operate using a laser diode and detector at a wavelength of 780, 650 and 405 nm respectively. This allows for data storage of 0.7, 4.7 and 25 GB respectively[11]. If an efficient laser diode operating in the ultraviolet was created then further improvement in data storage could be made[12].

As seen in **Figure 1-2** numerous applications exist for UV LEDs, but the current LEDs also need to be more efficient[2]. Compared to visible LEDs, producing highly efficient UV-based LEDs is difficult. UV emitting InGaN/GaN MQWs have weak carrier confinement and InGaN/AlGaN MQWs have severe quantum confined stark effect[13]. The choice of metal contact also plays a key role. Silver which is used in blue LEDs[14], is strongly absorbing for $\lambda<350$ nm[15]. In contrast, Al allows for good reflection in the UV but is a poor ohmic contact with *p*-doped materials[16]. Two further issues are the internal quantum efficiency (IQE) and also the extraction efficiency.

In the case of IQE, one effect is the issue of high dislocation density, where carriers can diffuse to threading dislocation cores and then recombine non-radiatively[17,18]. It has been shown that UV GaN based LEDs are more susceptible to dislocations than visible InGaN based LEDs[19,20]. This is due to the In atoms' random position within the crystal lattice, creating localised potential variations that are large enough to localise the carriers. This prevents carriers from reaching dislocations which would result in non-radiative recombination[21,22].

In this context it is worth searching for alternative alloys with the potential of addressing some of the listed issues. Boron has the benefit of being a small atom and therefore has the potential to create localised states that could reduce the diffusion length[23] and hence improve emission. Moreover, boron nitride is a high band-gap material, potentially preserving a high band-gap[24,25]. This issue may be particularly of interest in the UVA/UVB (300-340 nm) region as the lack of any natural substrate leads to an efficiency “gap” here[2].

For UVC it is known that extraction efficiency is a particular challenge, and one aspect is that emission from the surface of the device can become forbidden[15]. The crystal field split off sub band, begins to have a higher band than the light hole and heavy hole bands. This can reduce the extraction efficiency from 90% in visible LEDs to less than 10% for UVC LEDs[2,26]. This is further discussed in the theoretical **Section 2.1.1**, nevertheless due to time constraints, I was unable to carry out our experiments in the UVC range and this thesis will not discuss further results in the UVC range while addressing boron incorporation experiments.

In summary, there are many appliances and challenges for a device emitting in the UV region and this is where III-Nitride materials will play a key role in the near future.

1.2 Outline of thesis

This thesis involves results from both a theoretical and experimental aspect for B-containing III-Nitride materials. In both cases, the work was carried out with financial support from Science Foundation Ireland via a joint award with the Engineering and Physical Sciences Research Council-Centre of Doctoral Training.

In the remainder of **Chapter 1**, the principal properties of III-Nitride materials which include the crystal structure, polarisation, bandstructure, emission properties etc. will be discussed.

Chapter 2 describes the simulation techniques that were performed during the initial part of my research as a preparatory study to help understand the impact BN has on the active region of UV devices. The finite difference method was used to solve the one-dimensional Schrödinger equation. A single quantum well (QW) of BGaN with AlGaN quantum barriers (QB) was constructed to understand the effect BN had on the wavefunction overlap along with the emission energy of the material.

Chapter 3 focuses on the main experimental techniques that are mentioned in this thesis. Metalorganic vapour phase epitaxy is the main epitaxial method used in this work and is explained in detail along with a summary of other deposition methods. The structural, optical and morphology techniques used in this thesis are also discussed in this chapter. These include X-ray diffraction, photoluminescence,

photoluminescence excitation, scanning electron microscopy and transmission electron microscopy.

Chapter 4 deals with the growth of 120 nm thin layers of BGaN grown under compressive and tensile strain with varied temperatures. This initial study was pursued to see if it was possible to incorporate BN in our reactor. The surface morphology and structural properties of these thin layers were analysed. The presence of clustering was identified and a method to determine the B content is proposed.

Chapter 5 deals with the growth of a ternary and quaternary multiple quantum well (MQW) stack. Initially, a 5 MQW ternary stack consisting of $B_xGa_{1-x}N$/ $Al_{0.15}Ga_{0.85}N$ was grown with low B contents under varied temperatures and carrier gas. The emission from the MQW stacks was analysed along with the structural properties. The surface morphology for all the B-containing samples contained pits on the sample surface. To try and remove this pitting effect the growth of a quaternary MQW stack was completed consisting of $B_x(Al_{0.05}Ga_{0.95})_{1-x}N$/ $Al_{0.15}Ga_{0.85}N$.

In the final section of this thesis, the main conclusions of this research will be summarized, and possible areas for future work will be outlined based on the work completed in this thesis.

1.3 III-Nitride materials

III-V materials are crucial in optoelectronic fields due to their direct bandgaps and ability to tune that bandgap over a wide wavelength range. They consist of elements from the third and fifth groups of the periodic table. A subset of this group, which can reach the infrared, visible and UV spectral regions, using ternary and quaternary alloys is known as the III-Nitrides. A clear distinction between III-V and III-N materials lies in their normally different crystal structure.

1.3.1 Crystal structure

A crystal is a solid material where the atoms are arranged in a highly ordered manner to create a repeating pattern. This pattern consists of repeating unit cells. Inside these

unit cells, the III-Nitride molecules contain a tetrahedral geometry as seen in **Figure 1-3**, where a_i denotes the bond length.

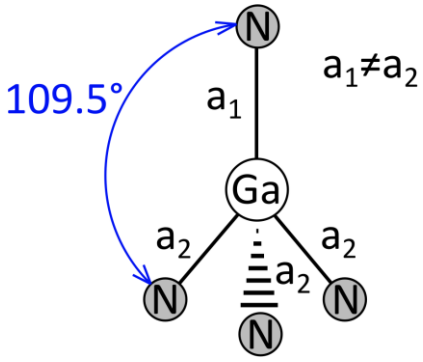

Figure 1-3. Tetrahedral coordination system for GaN.

III-Nitrides can either form the hexagonal wurtzite (WZ) or cubic zincblende (ZB) crystal phase. The difference in these crystal structures originates in their stacking sequence. WZ III-N materials contain an embedded hexagonal stacked sequence consisting of nitrogen and group-III atoms and this results in the A, B, A, B... stacking in the (0001) direction. The main structure focused on in this thesis is the WZ structure, with its hexagonal closed-packed (hcp) structure. This is in contrast to the zincblende structure which contains the cubic closed packing (ccp) structure consisting of the A, B, C, A, B, C.. sequence in the (111) direction. A schematic of both these stacking sequences can be seen in **Figure 1-4 (a),(b)**.

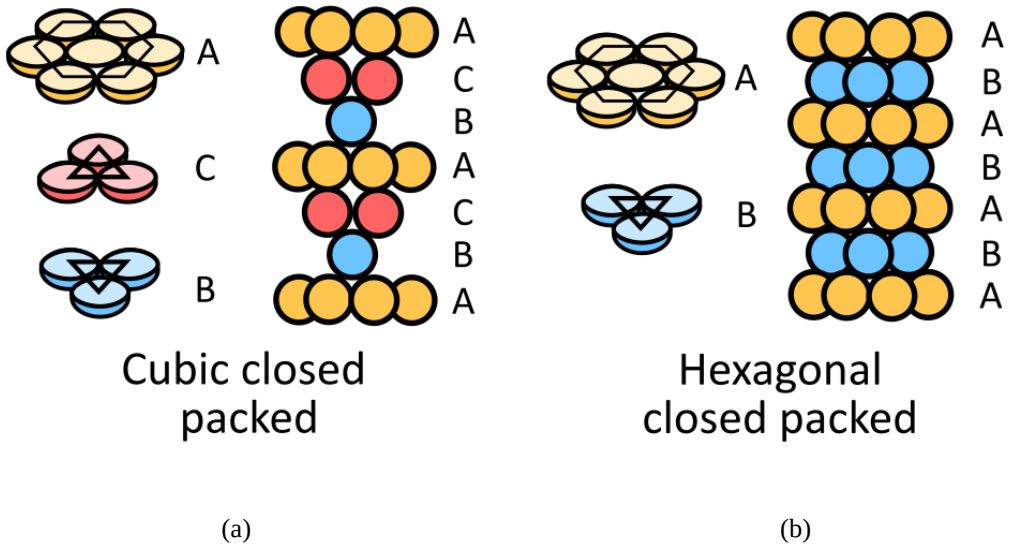

(a) (b)

Figure 1-4. Stacking sequence for a (a) cubic closed packed system and (b) hexagonal closed.

The WZ crystal structure for III-Nitride materials as seen in **Figure 1-5**, can be described by the two lattice parameters, *a* and *c*.

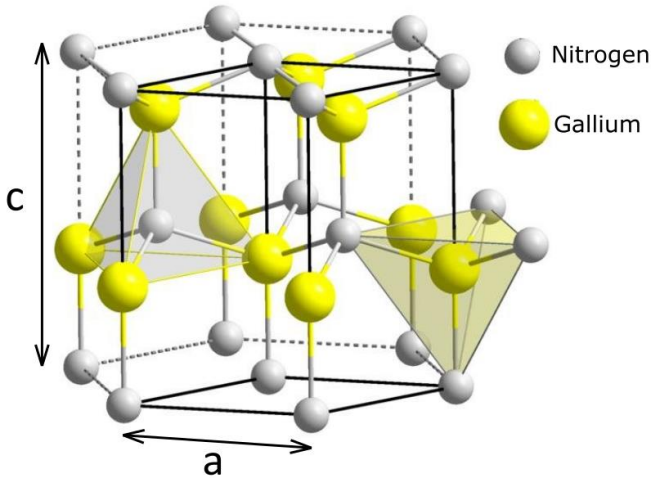

Figure 1-5. Crystal structure of wurtzite III-nitride materials. Picture modified from Ref. [27].

Under ambient conditions (i.e. room temperature; standard pressure), the *a* and *c* lattice parameters for the III-Nitrides can be seen in **Table 1-1**. The ideal c/a ratio of the lattice constant c_0 and a_0 for a hcp structure is 1.633[28].

Table 1-1. Lattice constants of wurtzite BN, AlN, GaN and InN at ambient condition.

	***a* (Å)**	***c* (Å)**	***c*/ *a***
BN	2.534[29]	4.189[29]	1.653
AlN	3.112[30]	4.982[30]	1.601
GaN	3.189[30]	5.185[30]	1.626
InN	3.545[30]	5.703[30]	1.609

The Miller indices *h*,*k*,*l* are often used to represent the nature of reticular planes. Each set of planes may be labelled by the inverse of the intercepts of *x*, *y* and *z*. A single plane and family of planes are often denoted by (h,k,l) and $\{h,k,l\}$ respectively. Different family planes for a simple cubic system can be seen in **Figure 1-6**.

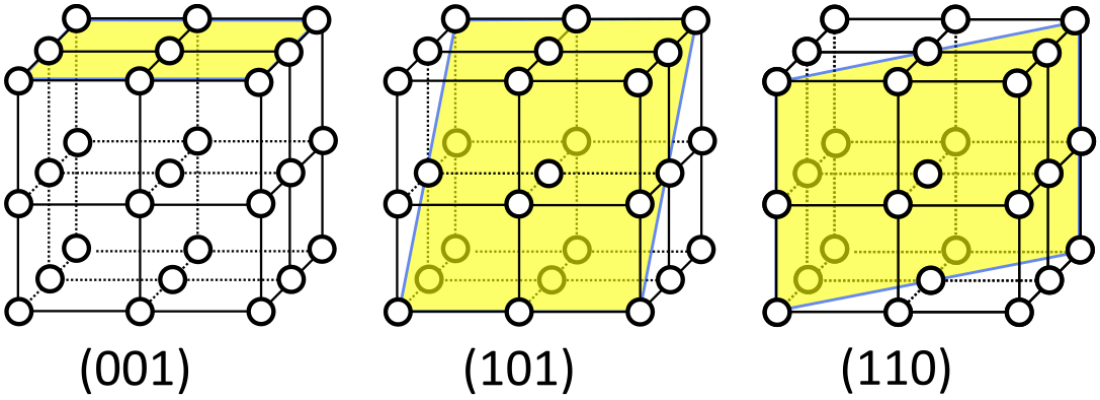

Figure 1-6. (001), (101) and (110) family lattice planes are shown for a simple cubic lattice.

In the case of WZ hexagonal crystal structures, Miller Bravais notation is used (h, k, i, l) where h, k, i, l are identical to the Miller indices with the additional index $i = -(h + k)$. Different family planes for a hexagonal crystal structure can be seen in **Figure 1-7**.

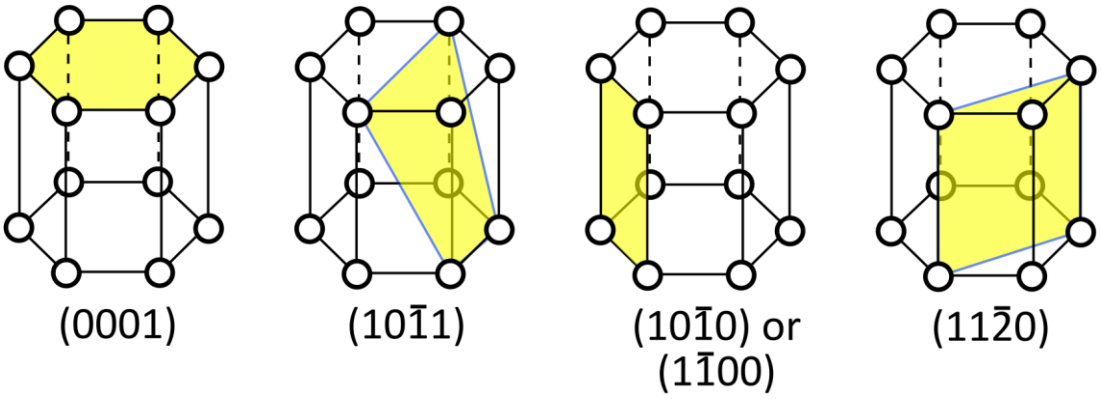

Figure 1-7. Schematic view of the (0001), (10$\bar{1}$1), (10$\bar{1}$0) and (11$\bar{2}$0) wurtzite crystal family lattice planes.

All the materials grown in this thesis were on the (0001) *c*-plane or polar plane which contains a polarisation field which can align along the [0001] or [000$\bar{1}$] directions. More details about the polarisation field will be discussed below. The non-polar *m* and *a*-plane are along the (10$\bar{1}$0) and the (11$\bar{2}$0) planes respectively which are inclined at 90° to the *c*-plane. At an inclination between these planes i.e. 0-90° are the semi-polar planes e.g. the (1011)[31].

1.3.2 Bandstructure of III-Nitrides

The standard III-Nitride materials include aluminium nitride (AlN), gallium nitride (GaN) and indium nitride (InN) which contain a direct bandgap energy of 6.0 eV[32], 3.51 eV[33] and 0.6 eV[33] respectively, at room temperature. A schematic of III-N along with the III-V emission wavelengths, bandgap energies and lattice constants can be seen in **Figure 1-8**.

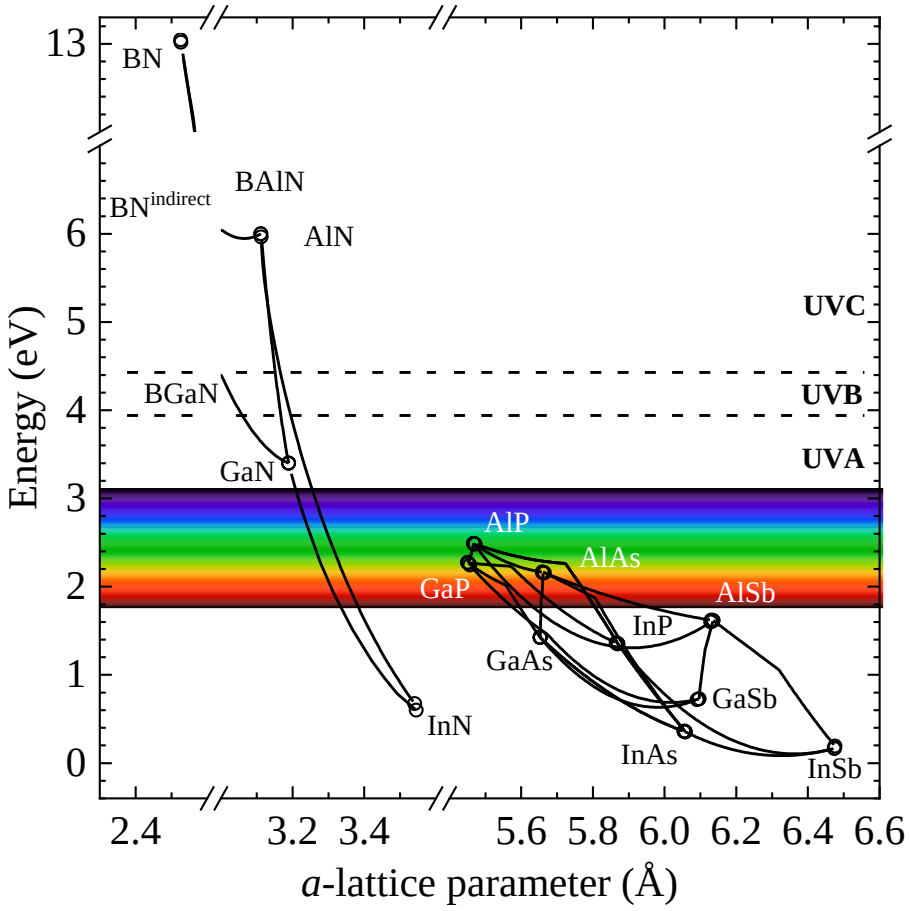

Figure 1-8. Bandgap energy versus lattice constant for III-Nitride alloys with bandgap bowing[24,25,30,34–38].

Vegard's law is often used to predict the physical properties of semiconductor alloys which uses a linear function of the parameters of the semiconductor components at their endpoints[39]. However, the bandgaps of III-Nitride alloys do not follow the linear Vegard's law but have a degree of deviation often referred to as "bowing"[40].

Boron nitride (BN) is a relatively new material when compared to the standard III-Nitride materials. The thermodynamically most stable structure of BN is a hexagonal layered structure similar to that of graphene. However, BN can also exist in many alternative phases such as the wurtzite, zincblende[41,42] etc. WZ-BN can only be achieved under specific boundary conditions[43]. WZ-BN is an indirect bandgap material with a bandgap energy of 6.7[25] eV and *a*-lattice constant of 2.534 Å[29]. A bandgap energy of 13.2 eV BN was used in this work which corresponds to the BN eigenstate energy that most resembles the conduction band minimum of GaN, along with a bowing parameter of 8.68 eV (which is only accurate for a boron incorporation <20%)[25].

1.3.3 Direct and indirect bandgaps

As mentioned previously, standard III-Nitride materials contain a direct bandgap in comparison to WZ-BN which is an indirect bandgap material. Different energy bands lie in the conduction and valence band and are calculated in "*k-space*" (momentum space) in which the energy of the crystal orbital wavelength determined by the phase of the atomic orbitals throughout the crystal, is inversely related to the wavevector *k*.

The unit cell of a structure in *k*-space is often referred to as the Brillouin zone with the first Brillouin zone in *k*-space centred around the Γ point. The bandstructure for different wurtzite materials can be compared by examining the first Brillouin zone as seen in **Figure 1-9**, with the symmetry points Γ, A, K, M, L and H seen in **Table 1-2**.

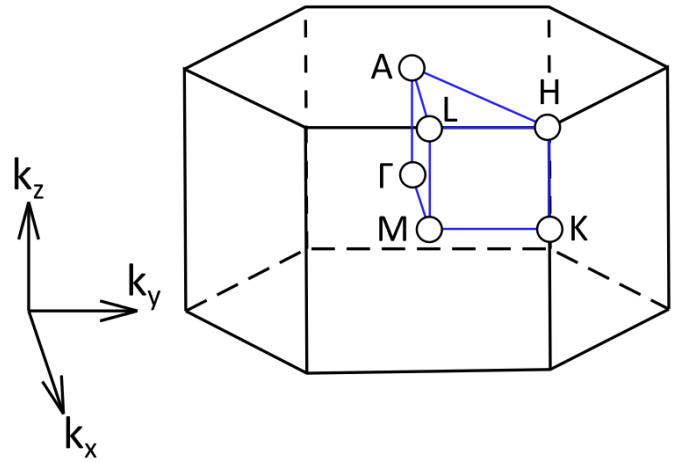

Figure 1-9. Brillouin points on a wurtzite lattice[44]

Table 1-2. The first Brillouin zone of a wurtzite lattice[45]

Symmetry points $(\boldsymbol{u}, \boldsymbol{v}, \boldsymbol{w})$	$[\boldsymbol{k_x}, \boldsymbol{k_y}, \boldsymbol{k_z}]$
Γ: (0,0,0)	[0,0,0]
A: $\left(0,0,\frac{1}{2}\right)$	$\left[0,0,\frac{\pi}{c}\right]$
K: $\left(\frac{2}{3},\frac{1}{3},0\right)$	$\left[\frac{4\pi}{3a},0,\frac{\pi}{c}\right]$
M: $\left(\frac{1}{2},0,0\right)$	$\left[\frac{4\pi}{3a},0,\frac{\pi}{c}\right]$
L: $\left(\frac{1}{2},0,\frac{1}{2}\right)$	$\left[\frac{\pi}{a},-\frac{\pi}{a\sqrt{3}},\frac{\pi}{c}\right]$
H: $\left(\frac{2}{3},\frac{1}{3},\frac{1}{2}\right)$	$\left[\frac{4\pi a}{3},0,\frac{\pi}{c}\right]$

The distance between the different Brillouin points are $\overline{\Gamma A} = \frac{\pi}{c}$, $\overline{\Gamma K} = \frac{4\pi}{3a}$, $\overline{\Gamma M} = \frac{2\pi}{a\sqrt{3}}$ and $\overline{MK} = \frac{2\pi}{3a}$.

A direct bandgap is when the maximum of the valence band and minimum of the conduction band contains no shift in the momentum vector, as a result, the emission of a photon occurs when an electron drops from the conduction band and recombines with a hole in the valence band. This is often referred to as radiative recombination. This is in contrast to an indirect bandgap, where a phonon is emitted along with a photon due to the requirement for conservation of momentum resulting in an indirect transition. A simple schematic of direct and indirect bandgap transitions with single bands can be seen in **Figure 1-10**.

The energy gap of III-Nitride materials is often determined from the wavelength of the exciton lines. A free exciton (FX) is when a hole is bound to an electron through the Coulombic interaction. Three main excitons exist in WZ III-Nitride materials; A exciton FX(A), B exciton FX(B) and C exciton FX(C). The presence of the FX(A) can be indicative of high-quality GaN[46]. The energy of these excitons can also vary depending on the strain of the material[47,48].

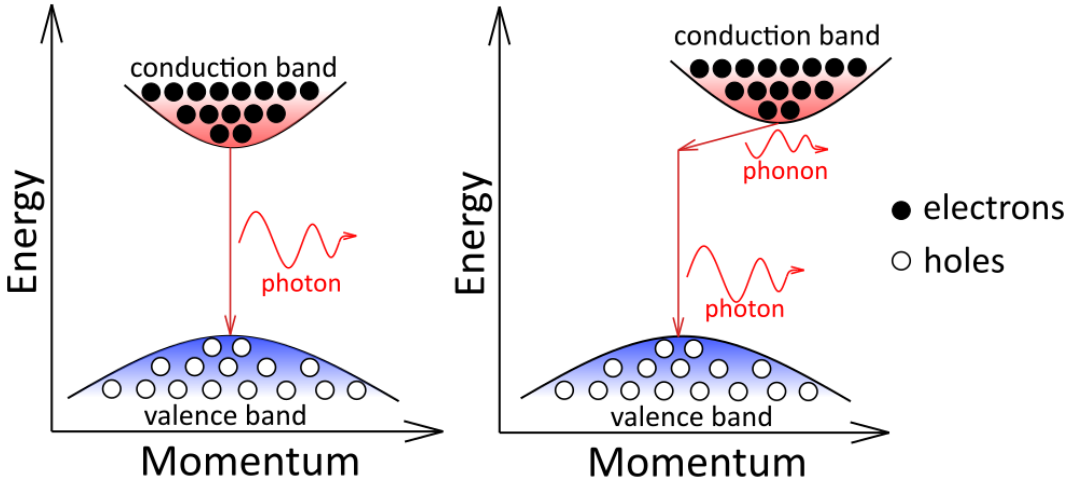

(a) (b)

Figure 1-10. (a) Direct and (b) indirect bandgap transitions

The spin-orbit (Δ_{SO}) and crystal field (Δ_{CR}) valence band splitting in GaN can be derived from the FX(A), FX(B) and FX(C) lines which results in a threefold degeneracy[49]. The relative position of these bands can be approximated using the quasi-cubic model developed by Hopfdeld *et al.*[50] as seen in **Equation 1-1** where E_A, E_B, E_C denote the excitonic energies.

$$E_{\pm} = \frac{1}{2}\left((\Delta_{SO} + \Delta_{CR}) \pm \left[(\Delta_{SO} + \Delta_{CR})^2 - \frac{8}{3}\Delta_{SO}\Delta_{CR} \right]^{\frac{1}{2}} \right)$$

$$E_+ = (E_C - E_A) \qquad E_- = E_B - E_A \qquad \text{1-1}$$

This splitting of the valence band for III-Nitride material can be seen in **Figure 1-11** for the direct bandgap semiconductor of GaN.

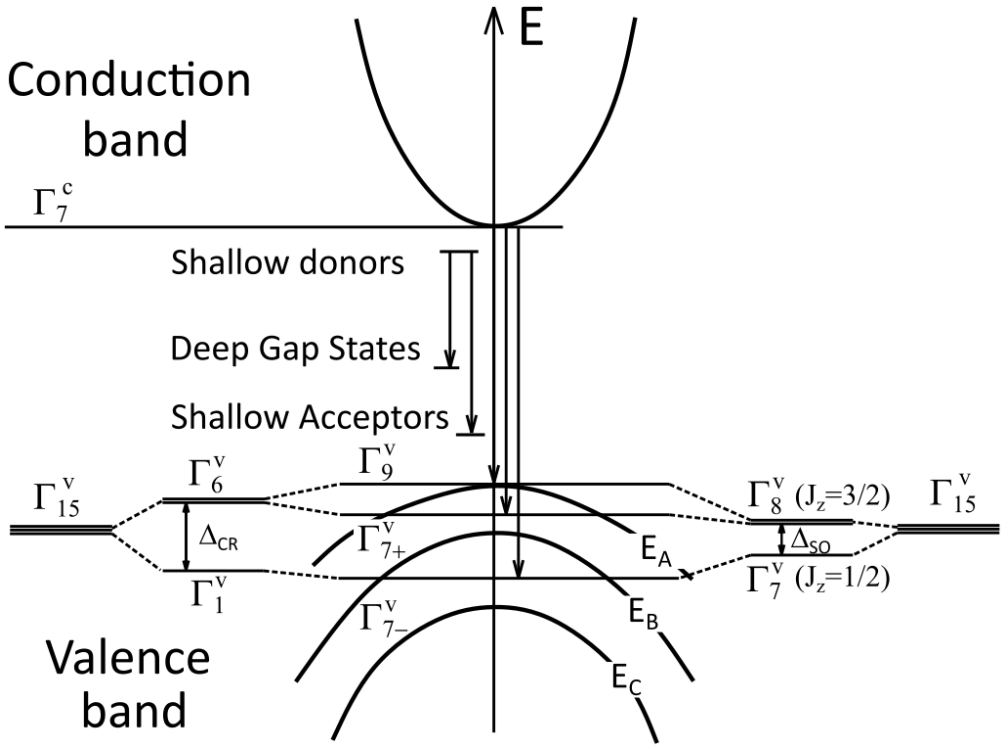

Figure 1-11. Schematic illustration of the electronic band structure of wurtzite GaN at the Γ-point of the first Brillouin zone[51]

The conduction band minimum of GaN is located at the centre of the Brillouin zone (Γ-point where k=0) and contains a Γ_7-symmetry[52] with a quantum number $J_z = \frac{1}{2}$. For GaN, the impact of Δ_{SO} results in the splitting of the valence band or Γ_{15}^v line into Γ_8^v and Γ_7^v with a separation of 0.014 eV[53]. The crystal-field splitting Δ_{CR} leads to the separation of the Γ_{15}^v into Γ_6^v and Γ_1^v with a separation of 0.019 eV[53]. The Γ_6^v band is further split into three sub-bands Γ_9^v, Γ_{7+}^v and Γ_{7-}^v in the valence band.

The positive Δ_{CR} splitting in GaN results in the formation of the Γ_9^v or heavy hole (HH) band, the Γ_7^v or light hole band (LH) band and the Γ_7^v or the crystal field split off hole band. The optical transition from the Γ_9^v band and the conduction band produces light polarisation perpendicular to the *c*-axis ($E \perp c$) and thus results in transverse electric (TE) polarised light.

This is in contrast to AlN, where a large negative Δ_{CR}= -0.164 eV[53] results in the Γ_7^v band being above the Γ_9^v band. As a result, this negative field splitting results in the optical transition from the Γ in the conduction band to produce light polarisation

parallel to the *c*-axis ($E \parallel c$) and thus results in transverse magnetic (TM) polarised light.

The difference in ordering of the valence bands for AlN ($\Gamma_{7vbm}^{v} \rightarrow \Gamma_{9}^{v} \rightarrow \Gamma_{7}^{v}$) compared to GaN ($\Gamma_{9vbm}^{v} \rightarrow \Gamma_{7+}^{v} \rightarrow \Gamma_{7-}^{v}$) as a result of the FX(A), FX(B) and FX(C), results in a difference in the optical and polarisation properties of the emitted light i.e. a polarisation switch in their properties as seen in **Figure 1-12**.

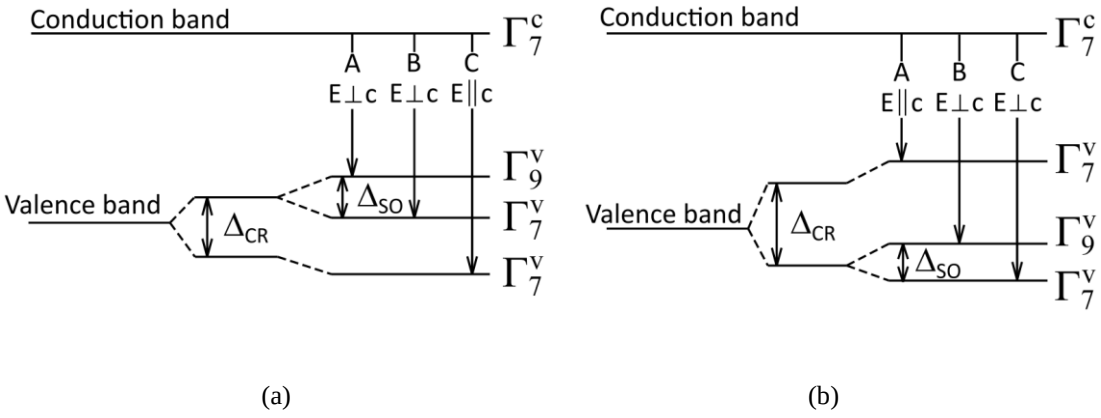

(a) (b)

Figure 1-12. Optical transitions between different valence bands to conduction band at the Γ-point due to crystal field and spin-orbit splitting for (a) GaN and (b) AlN[54]

The degree of polarisation is zero at the point where the three valence sub-bands Γ_9^v, Γ_{7+}^v and Γ_{7-}^v become degenerate. A large variation in the literature can be found for the Al concentration at which this switching between TE and TM polarised light occurs for emitting AlGaN layers. Different factors can impact the switching point such as strain and thickness of the material[55–58] as it impacts the bandstructure of the material.

Temperature also has an impact on the bandgap energy and can be described by the Varshni equation[59] as seen in **Equation 1-2** where $E_g(0)$ and $E_g(T)$ are the bandgap energy at a temperature T = 0 K and at a particular temperature T respectively.

$$E_g(T) = E_g(0) - \frac{\alpha T^2}{\beta + T} \qquad 1\text{-}2$$

The Varshni parameters are denoted by α and β which depend on the material properties. The Varshni parameters for GaN vary between $\alpha = 0.73 \rightarrow 1.08$ meV·K^{-1}

and $\beta = 700 \rightarrow 836$ K[48,60–64]. In the case of AlN, the values vary for $\alpha = 1.7 \rightarrow 2.63$ meV·K^{-1} and $\beta = 1462 \rightarrow 2082$ K[47,48,64–68].

Different III-Nitride materials contain their own unique energy gaps, resulting in a difference in the conduction band offsets (CBO) and valence band offsets (VBO). The main III-Nitride CBO and VBO used in this thesis can be seen in **Figure 1-13** where the valence band maximum of GaN is set as the zero point.

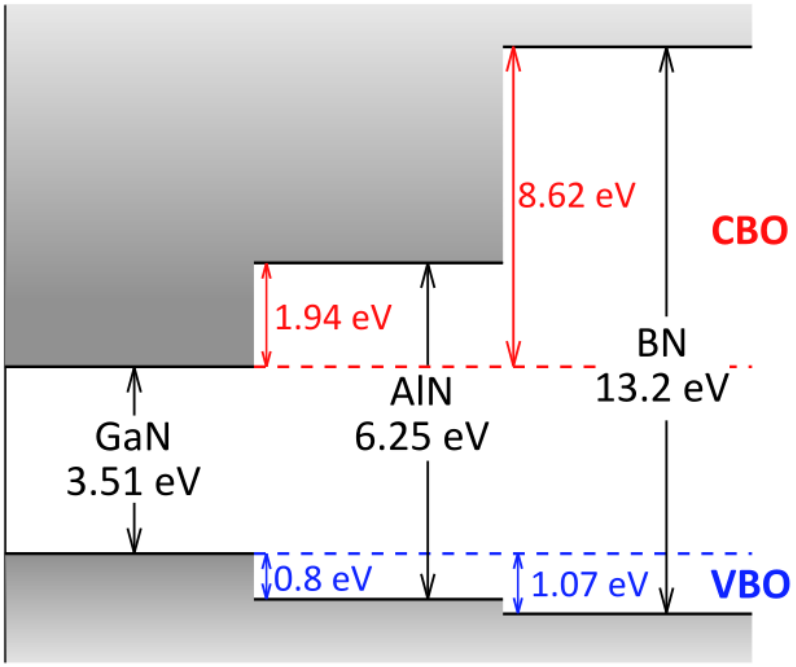

Figure 1-13. Conduction band and valence band offsets for III-Nitride materials[25,53,69,70]

The data for the bandgap and band offsets for B containing alloys is somehow limited due to the challenges in material preparation and characterisation. AlQatari *et al.*[71] showed by X-ray photoelectron spectroscopy (XPS) that a VBO of 0.3 eV existed between $B_{0.125}Ga_{0.875}N$ and GaN. Mickevičius *et al.*[72] showed a similar VBO of 0.3 ± 0.2 using XPS for epilayer of $B_{0.012}Ga_{0.988}N$/GaN. Theoretical techniques such as density function theory[73,74] along with different approximations results in a variation of the VBO of BN and GaN in the range of 0.3 to 1.21 eV[71,75,76]. In our work, a VBO of 0.85 eV was chosen as seen in Dreyer *et al.*[70] as it provides a value that is around the average of possible values seen in the theoretical literature.

1.3.4 Quantum wells

A common structure grown during epitaxy is a quantum well (QW). A QW consists of a (lower bandgap) material being sandwiched between layers of a different material (which contains a higher bandgap energy). This results in confinement within the well as seen in **Figure 1-14**.

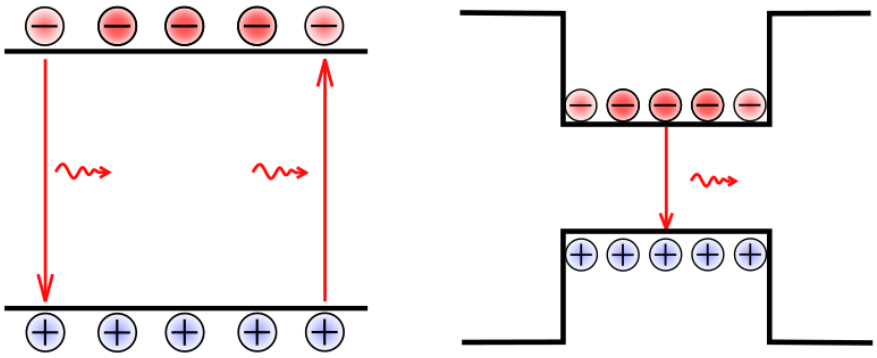

Figure 1-14. Schematic showing the impact a quantum well has on the electrons and holes.

The transition energy in a QW material (E_g) can be calculated using **Equation 1-3** where e_1 and hh_1 are the confinement energies of the electron and holes.

$$E_{e_1-hh_1} = E_g + e_1 + hh_1 - E_B - eF_W l_w \qquad 1\text{-}3$$

The exciton binding energy (E_B) is defined as the energy required to separate an electron-hole into free charge carriers, where an exciton is an electron bound to a hole via the Coulomb interaction. F_w denotes the electric field in the QW and l_w is the QW thickness. This term is often referred to as the quantum confined Stark effect and results in a redshift in the transition energy in QW structures. This effect was initially reported by Miller *et al*[77] and will be discussed in the next section.

1.3.5 Polarisation

The WZ crystal structure for III-Nitride material contains a spontaneous polarisation in the absence of external electric fields along the $[000\bar{1}]$ direction. This charge originates from the deviation of the ideal tetrahedral coordination system (as seen in **Figure 1-3**) and ionicity of the crystal due to the difference in electronegativity of the

group III and Nitrogen elements. Polarisation is an intrinsic property of the WZ III-Nitride materials which have a large impact on the performance of the LEDs[78].

The difference in electronegativity between two elements $(\Delta\chi)$ can be either ionic $(\Delta\chi > 1.7)$ or polar covalent $(0.5 < \Delta\chi < 1.7)$. In the case of the III-Nitride materials, nitrogen contains a large electronegativity and as a result, GaN $(\Delta\chi \approx 1.2)$, AlN $(\Delta\chi \approx 1.4)$, InN $(\Delta\chi \approx 1.2)$ and BN $(\Delta\chi \approx 1)$ all contain polar covalent bonds.

As a result, each unit cell contains a non-zero dipole momentum along the $[000\bar{1}]$ direction as seen in **Figure 1-15**, where the blue dashed line and red arrow denote the unit cell and dipole moment respectively.

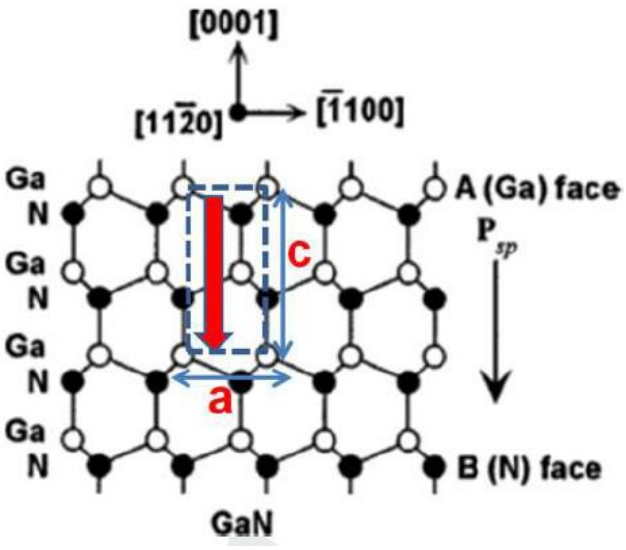

Figure 1-15. Crystal structure for GaN, with unit cell, dipole moment and lattice parameters *a* and *c*[28]

This polarisation charge is often referred to as the spontaneous polarisation (P_{sp}) charge[79] and the values for III-Nitride materials can be seen in **Table 1-3**.

Table 1-3. Spontaneous polarisation of wurtzite BN, GaN, InN and AlN

	BN	**GaN**	**InN**	**AlN**
$P_{sp}/\ C \cdot m^2$	-0.012[70]	-0.035[80]	-0.053[80]	-0.090[80]

The growth of the same or different crystalline materials on top of one another is often referred to as homoepitaxy or heteroepitaxy respectively and will be discussed in detail in **Chapter 3**. Heteroepitaxy is common when working with III-Nitride materials which results in mechanical stress, inducing a charge known as the piezoelectric polarisation (P_{pz})[79]. This charge arises due to a lattice mismatch between the two materials. Biaxial compressive stress $(\epsilon > 0)$ reduces the *a*-lattice parameter and increases the *c*-lattice parameter. This change in lattice constants induces the P_{pz} in the opposite direction of the P_{sp}. In contrast, when a material is under tensile stress $(\epsilon < 0)$ a reduction is observed in the *c*/*a* ratio, hence the P_{sp} and P_{pz} are in the same direction and are additive[81]. A schematic illustrating the distortion of the lattice can be seen in **Figure 1-16**.

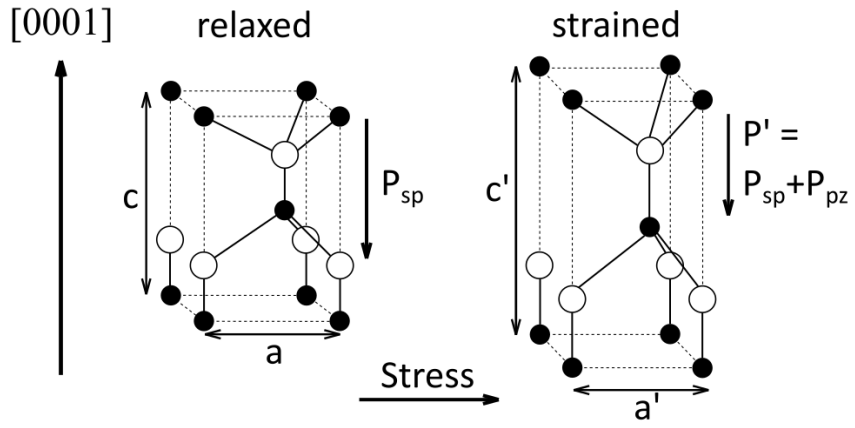

Figure 1-16. Impact of crystal deformation on polarisation

A combination of both the P_{sp} and P_{pz} charge results in the quantum confined Stark effect (QCSE) being present which results in a reduction in the wavefunction overlap and redshift of the emission spectrum as seen in **Figure 1-17**.

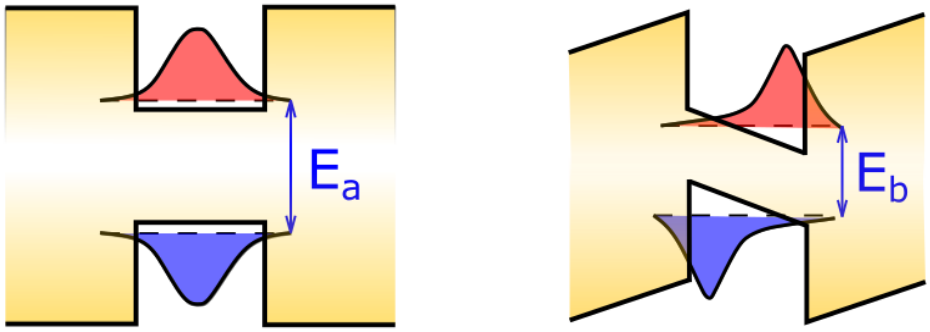

(a) (b)

Figure 1-17. Quantum well (a) without and (b) with a polarisation-induced field present

The impact of compressive and tensile stress can be seen in **Figure 1-18** the interface charges are denoted by $\sigma^{+/-}$.

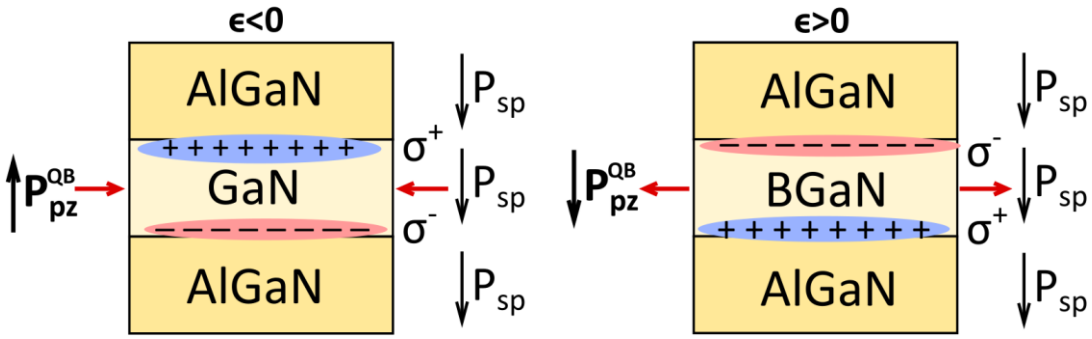

(a) (b)

Figure 1-18. Polarisation direction for an in-plane (a) compressive strain GaN/ AlGaN and (b) tensile strain BGaN/ AlGaN QW

1.3.6 Excitonic and intrinsic emission

Optical transitions in III-Nitride materials can be divided into extrinsic and intrinsic transitions. Intrinsic transitions are intrinsic to the material. Examples include free excitons (which is a bound electron-hole pair), phonon replicas (which are due to an exciton and lattice vibration) and free-to-free transitions (which are due to an electron unbound to an atom). Extrinsic transitions in contrast originate in the material from defects and impurities. Examples of extrinsic transitions include free-to-bound,

bound-to-bound etc. The main optical transition processes in WZ-GaN can be seen in **Figure 1-19**[82]. A bound exciton exists when an exciton is bound to a defect or vacancy. As the temperature increases this bound exciton acquires enough energy to break free from the defect/vacancy.

With WZ III-Nitride materials, the valence band is split by crystal field splitting and spin-orbit interactions, as seen in **Figure 1-11**. The free excitons associated with the band splitting are often denoted as FX(A), FX(B) and FX(C) excitons. The origin of these excitons are; FX(A) = $\Gamma_7^C - \Gamma_9^V$ (associated with the heavy hole state), FX(B) = $\Gamma_7^C - \Gamma_{7+}^V$ (associated with the light hole state) and FX(C) = $\Gamma_7^C - \Gamma_{7-}^V$ (associated with the crystal field splitting state).

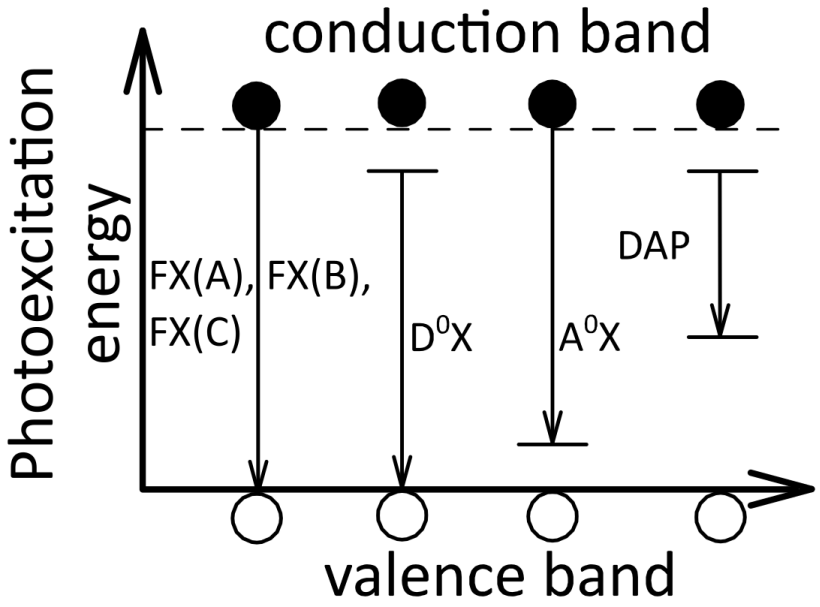

Figure 1-19. Extrinsic and intrinsic optical processes in GaN

In **Figure 1-19**[82], a free exciton bounded to a neutral donor (D^0) results in the photoluminescence emission line (D^0X). An exciton bounded to a neutral acceptor (A^0) can result in the emission line A^0X and a bound-to-bound transition or donor-acceptor pair is denoted by DAP.

1.3.7 Lattice matching

The growth of two different materials on top of one another results in different strains/relaxation in the material. The lattice mismatch (f) between the substrate (a_{sub}) and the grown layer (a_{layer}) can be calculated using **Equation 1-4**[83]**.**

$$f = \frac{a_{sub} - a_{layer}}{a_{sub}} \qquad 1\text{-}4$$

As the thickness of the grown layer increases, the elastic strain energy in the material also increases and can eventually result in dislocations forming in the material.

Dislocations are imperfections that can develop in the crystal structure of materials and play an important role in defining material mechanical characteristics. The main types of dislocations include edge, screw and mixed dislocations. These dislocations differ in several ways, including their geometry and how they affect material properties. The Burgers vector $(\overline{b})$ or the slip vector represents the magnitude and directions of the lattice distortion[84].

Edge dislocation

If the $\overline{b}$ is perpendicular to the dislocation line, then an edge dislocation is formed. Edge dislocations arise when an extra half-plane of atoms is added to the crystal structure, resulting in the dislocation line, a step-like structure as seen in **Figure 1-20(b)**.

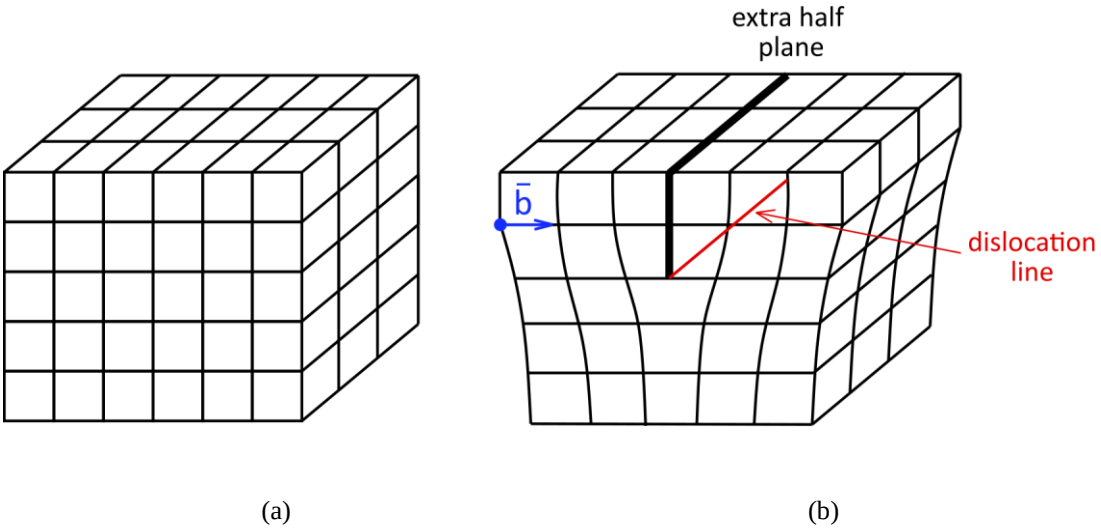

Figure 1-20. Atomic lattice (a) before and (b) after edge dislocation formation

Screw dislocation

If the $\overline{b}$ is parallel to the dislocation line, a screw dislocation is formed. The atomic model of a screw dislocation is an extra half plane as seen in **Figure 1-21(a)** where the right side (R) slips with respect to the left side (L).

The slip line defines a boundary on the slip plane into a front (F) and back (B) side. The slip line represents the boundary line which is our dislocation line. If the slip is only confined to the front side, not the back. In **Figure 1-21(a)** the slip is defined on the F side and not the B, and if the slip is equal to the distance of one interplanar spacing then **Figure 1-21(b)** is obtained[84]. The parallel planes perpendicular to the dislocation line join to form a continuous spiral ramp (or screw shape) also referred to as a helicoidal surface with a dislocation line as its axis.

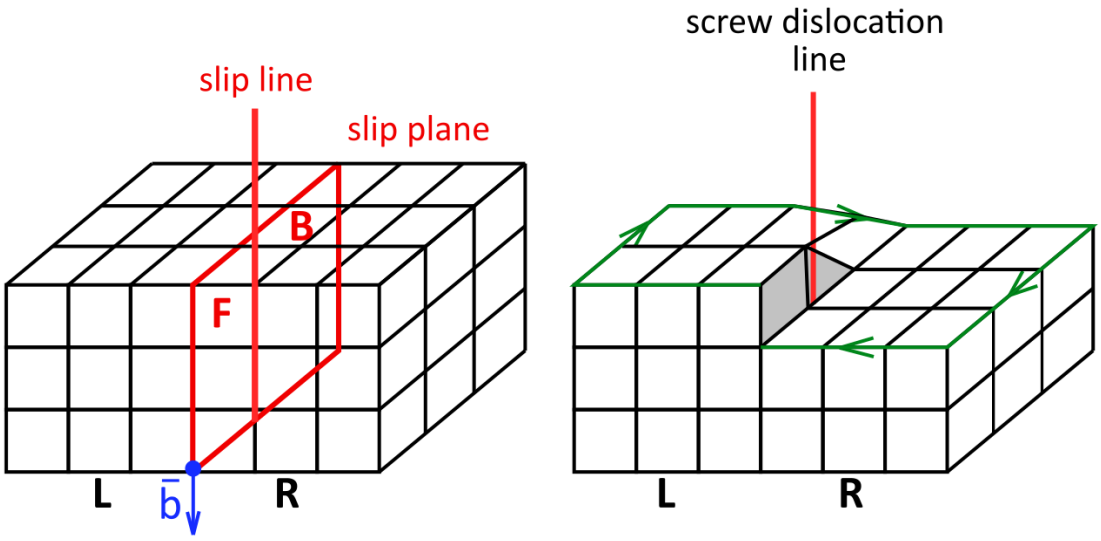

(a) (b)

Figure 1-21. Atomic lattice (a) before and (b) after screw dislocation formation

Mixed dislocation

If the $\overline{b}$ is not parallel or perpendicular to the dislocation line, then a mixed dislocation is formed i.e. $\overline{b}$ is at some angle to the dislocation line. Mixed dislocations usually contain a mixture of the characteristics of both edge and screw dislocations.

In the case of epitaxial growth of polar (0001) oriented GaN, a large density of threading dislocations occur with a direction line perpendicular to the (0001) interface. These dislocations are the *a*-type $\frac{1}{3}[11\bar{2}0]$ edge, *c*-type $[0001]$ screw and (*a*+*c*)-type $\frac{1}{3}[11\bar{2}3]$ mixed dislocations[85].

2 THEORETICAL WORK ON BORON CONTAINING III-NITRIDE HETEROSTRUCTURES

In this chapter, an introduction is given into the theoretical work that other groups have achieved with the alloying of B containing III-Nitride materials. Key simulation methods and methodologies that aided in the understanding and guiding of the experimental work later in this thesis are also discussed.

2.1.1 Theoretical literature work

WZ-BN contains many unique parameters in terms of its large bandgap energy bowing parameter when alloyed with other III-Ns, small lattice constants, dissimilar (to conventional III-Ns) piezoelectric coefficients (e_{31}, e_{33})[24,25], elastic constants (C_{13}, C_{33})[29], spontaneous polarisation (P_{sp}) when compared to the conventional III-N[24,25,29,70,86] and as a result, numerous potential applications for the material exist. WZ-BN may help in terms of strain engineering, resulting in a reduction in the quantum-confined Stark effect (QCSE) which could potentially lead to an overall increase in the internal quantum efficiency (IQE).

As mentioned in **Section 1.3.3** the topmost valence band for III-Nitride materials can vary. In the case of AlN the ordering of this sub band results in the emission of TM mode perpendicular to the c-axis[87]. BN contains a unique crystal field splitting energy (Δ_{CR}) of 333 meV[88] when compared to the standard III-Nitrides (Δ_{CR}^{GaN}= 0.019eV[53]and Δ_{CR}^{AlN} = -0.164 eV[53]) and as a result, will alter the topmost valence sub band which could help improve the efficiency of UV devices. Park, Ahn *et al*[89]. showed for a BAlGaN/ AlN QW with an Al content of 0.7 and boron content of <0.01, the characteristic of the topmost valence band is dominated by the light hole (LH) band and not the conventional heavy hole (HH) band. Thus, resulting in an emission intensity three times larger than the conventional QW emission. Park *et al.*[88] have shown that a boron incorporation of less than 50% in a BAlGaN/AlN QW structure, can be used as a TE-polarised light source resulting in a high efficiency for DUV device. The potential for TM emission with low extraction efficiency is a major issue in the conventional AlGaN based designs.

Park *et al.*[90] showed that small incorporations of BN into the active region of optoelectronic devices result in an improvement in the spontaneous emission coefficient for BGaN/ AlN compared to AlGaN/ AlN QWs. Xing *et al.*[91] reported from their simulation work that an undoped BGaN electron blocking layer (EBL) increased the effective barrier height along with reducing the polarisation-induced electric field. This resulted in a slope efficiency (which is the ratio between the output to input power) of 289% and a 51% lower threshold current (which is the point stimulated emission dominates over spontaneous), than that of highly doped AlGaN. Strain engineering with BN can also improve the reflectivity and lattice matching of distributed Bragg reflectors for both the visible and UV range[92,93].

Thus, there are advantages of incorporating BN with III-Nitride material. In this chapter, the one-dimensional Schrödinger equation is solved for a single quantum well (SQW) of BGaN/ AlGaN to see the impact BN has on the material in terms of the wavefunction overlap along with the emission energy. Polarisation, strain and offset potentials are included in our calculation.

2.2 One-dimensional Schrödinger equation

The one-dimensional Schrödinger equation which was used in this work can be seen in **Equation 2-1**. Since we are interested in establishing a general framework, a position-independent effective mass is applied otherwise strain and built-in field corrections will have to be applied. This means that the effective mass in the well and the barrier are identical and is a common approach in dealing with III-N QW materials[94–96].

$$\left\{-\frac{\hbar^2}{2m}\frac{\partial^2}{\partial x^2} + U_{v/c}^{off}(z) + q\cdot\phi^{pol}(z) + S_{v/c}(z)\right\}\Psi(z) = E\Psi(z) \qquad 2\text{-}1$$

The notation for the terms above is; $-\frac{\hbar^2}{2m}\frac{\partial^2}{\partial x^2}$ is the kinetic energy term, $U_{v/c}^{off}(z)$ is the offset potential for the valence and conduction band (which were already discussed in **Chapter 1**), q denotes the elementary electron charge, $\phi^{pol}(z)$ is the polarisation potential and $S_{v/c}(z)$ is the strain component for the valence and

conduction band. The term $\hbar = 6.626 \times 10^{-34}$ J · Hz^{-1} is Planck's constant. Due to a small difference in the effective masses for AlGaN and GaN and a low incorporation of boron in the QW (which will be discussed further below), the values associated with GaN were used in our calculations where $m_h = 1.876$[97] and $m_e = 0.209$[97] were used for the holes and electrons respectively. Each component in **Equation 2-1** above will be discussed in this chapter.

2.2.1 Band alignment

A heterostructure of interest in this thesis is a QW which uses differences in the valence and conduction band alignment of the well and barrier material to confine carriers in one direction i.e., along the wurtzite *c*-axis. The main values used to calculate the conduction band offset $\left(U_c^{off}\right)$ and valence band offset $\left(U_v^{off}\right)$ potentials were previously shown in **Figure 1-13**. The two main band alignments classification of heterostructures in this work are type-I or type-II[98] as seen in **Figure 2-1**.

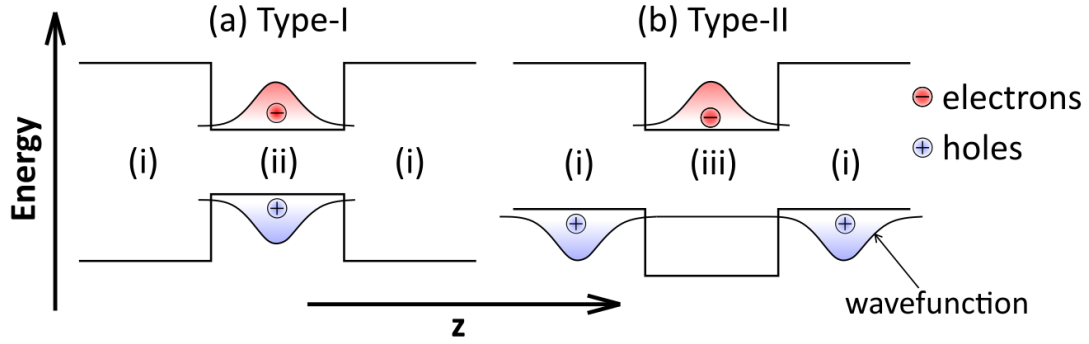

Figure 2-1. Examples of a double heterostructure containing (a) type-I and (b) type-II band alignment.

Carrier confinement occurs for both the electrons and holes in type-I band alignment (**Figure 2-1 (a)**), due to the bandgap of (ii) sitting entirely inside bandgap. As a result, a confining well is formed for both the electrons and holes. If only one of the carriers, i.e. the electrons are confined, then a type-II band alignment forms due to the different conduction and valence band alignments (**Figure 2-1 (b)**). Since radiative recombination is dependent on the overlap of the electron and hole wavefunctions[2], type-I band alignment is normally used for LED devices.

The use of heterostructures is beneficial for the confinement of carriers and manipulation of the emission wavelength. However, the use of two different binary or alloy materials in general leads to a lattice mismatch. For example, the *a*-lattice constant of GaN and AlN differs by approximately 2%. This lattice mismatch will result in strain effects in the active region of for instance an AlGaN/ GaN LED[99].

2.2.2 Elasticity

In III-Nitride structures, the impact of strain can modify the material properties along with the electronic structure and as a result alters the carrier confinement (which was discussed in the previous section). Properties such as the valence band maxima, conduction band minima[100] and the effective masses[101] can be impacted by strain.

A second-rank tensor as seen in **Equation 2-2**[102,103] can be used to describe strain component (ε_{ij}) in the material where the i^{th} and j^{th} component denote the change in position along the i-direction due to a deformation along the i^{th} direction.

$$\varepsilon = \begin{pmatrix} \varepsilon_{xx} & \varepsilon_{xy} & \varepsilon_{xz} \\ \varepsilon_{yx} & \varepsilon_{yy} & \varepsilon_{yz} \\ \varepsilon_{zx} & \varepsilon_{zy} & \varepsilon_{zz} \end{pmatrix} \qquad 2\text{-}2$$

Voigt notation[104] can be used to rewrite the tensor as seen in **Equation 2-3**, where $\varepsilon_{xx} = \varepsilon_1$, $\varepsilon_{yy} = \varepsilon_2$, $\varepsilon_{zz} = \varepsilon_3$, $2\varepsilon_{yz} = \varepsilon_4$, $2\varepsilon_{xz} = \varepsilon_5$ and $2\varepsilon_{xy} = \varepsilon_6$.

$$\varepsilon = (\varepsilon_1 \;\; \varepsilon_2 \;\; \varepsilon_3 \;\; \varepsilon_4 \;\; \varepsilon_5 \;\; \varepsilon_6)^{\dagger} \qquad 2\text{-}3$$

It is assumed that the strained material can be formed by small deformations in the unstrained material. Therefore, the initial strain can be rewritten in terms of the relative difference between the lattice constant of the strained material and host material as seen in **Equation 2-4**[105]. It is assumed that the tensor above can be simplified by neglecting the shear strain in the system and assuming a QW system and therefore setting the off-diagonal components to zero i.e. $\varepsilon_{ij} \underset{i \neq j}{\longrightarrow} 0$.

$$\varepsilon = \begin{pmatrix} \frac{a_0 - a}{a} & 0 & 0 \\ 0 & \frac{b_0 - b}{b} & 0 \\ 0 & 0 & \frac{c_0 - c}{c} \end{pmatrix} \quad 2\text{-}4$$

In the tensor above, the terms a, b and c are the lattice constants of the strained material and the terms a_0, b_0 and c_0 are the host material. In WZ III-Nitride materials, $a = b \neq c$ and as a result $\varepsilon_{11} = \varepsilon_{22}$. For a QW system, it is assumed that the QW is strained to match the in-plane *a*-lattice constant of the unstrained QB (host material). The QW then relaxes along the *c*-direction (out of plane)[30,106].

As a result, the out-of-plane strain component (ε_{33}) can be rewritten in terms of the *a*-lattice constant and the strain along the *c*-direction which minimises the elastic energy of the system as seen in **Equation 2-5**[30].

$$\varepsilon_{33} = -2\frac{C_{13}}{C_{33}}\varepsilon_{11} \quad 2\text{-}5$$

The terms C_{ij} are the elastic constants and can be calculated using a linear interpolation of the relevant binary materials. The in-plane strain component also known as the biaxial strain component is defined as $\varepsilon_{11} = \frac{a_B - a_W}{a_W}$ where a_B and a_W is the QW (strained material) and QB (host material) lattice constant. The *a*-lattice constants for along with the elastic constants for III-Nitride materials can be seen below in **Table 2-1**.

Various literature results can be found for both the *a* and *c* lattice constants ranging from 2.520 to 2.558 Å and 4.170 to 4.228 Å, respectively.[70,107–111] The elastic constants (C_{ij}) also vary in literature from 61 to 74 Pa for C_{13} and 1020 to 1077 Pa for C_{33}[107,108,112]. In our work, the values were based on Sheerin *et al*[29]. as it provides a value that is around the average of possible values seen in literature.

Table 2-1. Elastic constants along with lattice constants for III-Nitride materials.

	AlN	GaN	BN	InN
a/ Å	3.112[30]	3.189[30]	2.534[29]	3.545[30]
c/ Å	4.982[30]	5.185[30]	4.189[29]	5.703[30]
C_{13}/ Pa	108[30]	106[30]	64[29]	115[30]
C_{33}/ Pa	373[30]	398[30]	1113[29]	92[30]

An interesting observation is that WZ-BN contains a much smaller C_{13} and much larger C_{33} component when compared to the standard III-Nitrides. This will result in a reduction in the $\frac{C_{13}}{C_{33}}$ ratio when alloying with BN. Further to this, consider a BGaN QW grown on AlN, the smaller *a*-lattice constant of BN (as seen in **Table 2-1**) will result in a reduction in the ε_{11} component for low B incorporation. This will result in an overall reduction in the strain in the system thus resulting in a reduction in the piezoelectric polarisation field (which was discussed in **Section 1.3.5** and will be discussed further in **Section 2.2.4**) and could lead to an improvement in radiative recombination[113] for low BN content in the QW.

2.2.3 Strain effects

The strain-dependent part of the electron (S_c) and hole (S_v) Hamiltonian was calculated using the equation found in Fonoberov *et al.*[53] as seen in **Equation 2-6** where it was assumed that the well material was strained to the barrier and contains no shear strain.

$$S_v = \varepsilon_{11}(l_1 + m_1) + m_2\varepsilon_{33}$$

$$S_c = 2a_{ct}\varepsilon_{11} + a_{cz}\varepsilon_{33} \qquad 2\text{-}6$$

The conduction band deformation potentials for the out-of-plane and in-plane strain are denoted by a_{ct} and a_{cz}. The term ε_{ij} denotes the strain tensor components as

previously discussed above. Finally, the terms l_1, m_1 and m_2 are composed of the valence band deformation potentials (D_i) as seen in **Equation 2-7**[94].

$$l_1 = D_1 + D_4 + D_5$$

$$m_1 = D_2 + D_4 - D_5$$

$$m_2 = D_1 + D_3 \qquad 2\text{-}7$$

The deformation potentials for the III-Nitride materials can be seen in **Table 2-2**. These values were also taken from Sheerin *et al.*[29] due to the limited literature reports.

Table 2-2. Valence and conduction band deformation potentials for III-Nitride materials.

	AlN	GaN	BN	InN
a_{cz} / eV	-	-8.6[29]	-3.33[29]	-
a_{ct} / eV	-	-6.22[29]	-21.42[29]	-
$a_{cz} - D_{1/}$ eV	-4.31[114]	-6.03[29]	-2.36[29]	-3.62[114]
$a_{ct} - D_{1/}$ eV	-12.11[114]	-8.98[29]	-24.44[29]	-4.60[114]
D_1/ eV	-	-2.56[29]	-0.97[29]	-
D_2/ eV	-	2.76[29]	3.02[29]	-
D_3/ eV	9.12[114]	5.38[29]	2.71[29]	2.68[114]
D_4/ eV	-3.79[114]	-2.95[29]	-2.74[29]	-1.74[114]
D_5/ eV	-3.23[114]	-2.8[29]	-4.05[29]	-2.07[114]

2.2.4 Polarisation

As mentioned previously in **Chapter 1**, the spontaneous and piezoelectric polarisation exists when working with WZ III-Nitride materials. The piezoelectric polarisation can

be written as seen in **Equation 2-8** assuming that the *c*-plane QW system contains no shear strain.

$$P_{pz}\,\hat{z} = (\varepsilon_1 e_{31} + \varepsilon_2 e_{32} + \varepsilon_3 e_{33})\hat{z} \qquad 2\text{-}8$$

The terms ε_i and e_{ij} represent the strain tensor components and the piezoelectric tensor components respectively. Using the piezoelectric polarisation (**Equation 2-8**) and out-of-plane strain component (**Equation 2-5**), a simplified equation can be seen in **Equation 2-9**.

$$P_{pz} = P_{pz}^{W}\hat{z} = 2\varepsilon_1\left(e_{31} - e_{33}\frac{C_{13}}{C_{33}}\right)\hat{z} \qquad 2\text{-}9$$

Using Poisson's equation as seen in **Equation 2-10** and assuming that there are no free charges in the system and the permittivity of the medium (ε) is spatially constant, the polarisation potential (ϕ^{pol}) can be calculated. The term P denotes the total polarisation i.e. $P_{sp} + P_{pz}$.

$$-\varepsilon\left(\nabla^2\phi^{\mathrm{pol}}\right) = \rho_{pol} = -\nabla \cdot P \qquad 2\text{-}10$$

By assuming a one-dimensional QW system, using the boundary conditions of zero field in the QB as $z \to \pm\infty$, then **Equation 2-11** can be obtained[30]**.**

$$\phi^{pol}(z) = \left(\frac{P_{sp}^{W} - P_{sp}^{B} + P_{pz}^{W}}{2\epsilon_0\epsilon_r^{W}}\right)(|z| - |z-h|) \qquad 2\text{-}11$$

Polarisation was assumed to be along the growth direction (*c*-axis) and strain was only applied in the basal plane. It was assumed that the QW begins at $z = 0$ and ends at $z = h$ thus resulting in a QW thickness of h. The term $\varepsilon = \varepsilon_0\varepsilon_r^{w}$ where ε_0 and ε_r^{w} denotes the permittivity of the free space and relative permittivity of the well. The relative permittivity values for the III-Nitride materials used in this work can be seen in **Table 2-3**, along with $\varepsilon_0 = 8.85 \times 10^{-12}\mathrm{F}\cdot\mathrm{m}^{-1}$.

Table 2-3. Relative permittivity of III-Nitride materials.

	AlN	GaN	BN	InN
ϵ_r	8.5[115]	9.6[115]	6.65[116]	15.3[115]

As seen previously WZ-BN contains different elastic and lattice constants (**Table 2-1**) when compared to the standard III-Nitrides. This unique aspect of BN also occurs in both the spontaneous and piezoelectric components which will be discussed next.

2.3 Correct polarisation constants when working with B-III-Nitrides

The theory of Berry-phase[117] is the main method to calculate the polarisation, by starting with a predefined reference frame. In the Berry phase theory of polarisation, absolute polarisation is not accessible and only differences in polarisation between two states of an insulating material are focused on[118] i.e. a centrosymmetric structure P_{CS} (which contains inversion symmetry and thus no polarisation present) and non-centrosymmetric P_{non-CS} counterpart.

The calculation of the P_{sp} and P_{pz} components (e_{33} and e_{33}) requires the choice of a reference structure, which in the case of WZ III-Nitride materials has originally chosen to be the [111]-oriented zincblende (ZB) structure[119–121]. The ZB reference frame was the initial approach used in the late 90s by Bernardini, Fiorentini and Vanderbilt[119]. For the ZB-reference frame, you take the ZB structure oriented along the [111] direction which looks similar to the [0001] oriented WZ system when looking at the first atomic nearest neighbour (as seen in **Figure 2-2**[122] **(a)** and **(b)** respectively).

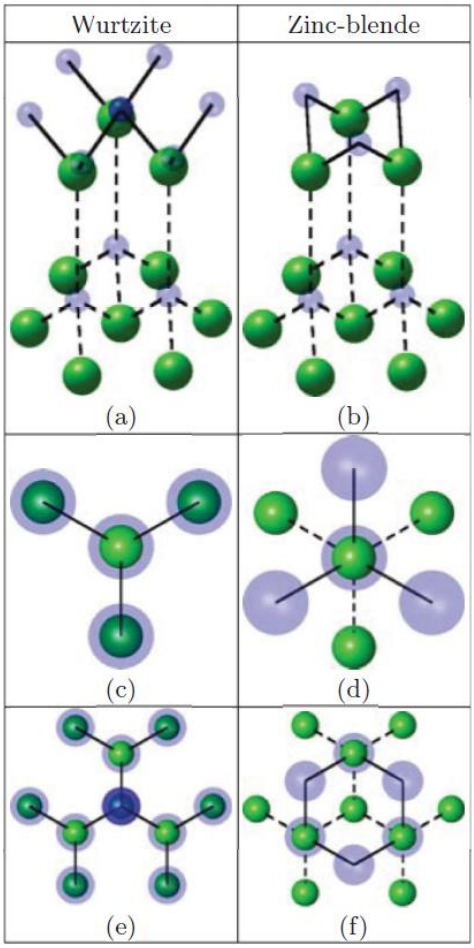

Figure 2-2. The wurtzite and (b) zinc-blende crystal structures where the z-direction is parallel to the *c*-axis and [111] direction respectively. The "eclipsed" and "staggered" dihedral conformations for wurtzite and zinc-blende are displayed in (c) and (d), respectively. The top view of [0001]-wurtzite and [111]-(zinc-blende).

The initial ZB structure corresponds to an unstrained crystal structure which is centrosymmetric (P_{CS}). If you look at the second nearest neighbour 9/12 have identical positions and 3 are different (which can be easily seen in the plan view of **Figure 2-2 (e)** and **(f)**). If you rotate these 3 atoms adiabatically, to go from the [111] ZB structure to the WZ structure which contains a charge i.e. non-centrosymmetric or P_{non-CS}, the corresponding change in polarisation is the required value as seen in **Equation 2-12**.

$$\Delta P = P_{non-CS} - P_{CS} \qquad 2\text{-}12$$

This is the method used for calculating the polarisation in the ZB reference frame i.e. P_{sp}^{ZB} and the 'proper' piezoelectric components e_{31}^{prop} and e_{33}^{prop}.

For the hexagonal (H) reference frame, it is proposed that starting with the WZ structure is the correct method for calculating the polarisation[80]. The WZ structure contains a $P6_3mc$ space group whereas the two-dimensional H structure contains a $P6_3/mmc$ space group[123] as seen in **Figure 2-3 (a)** and **(b)** respectively.

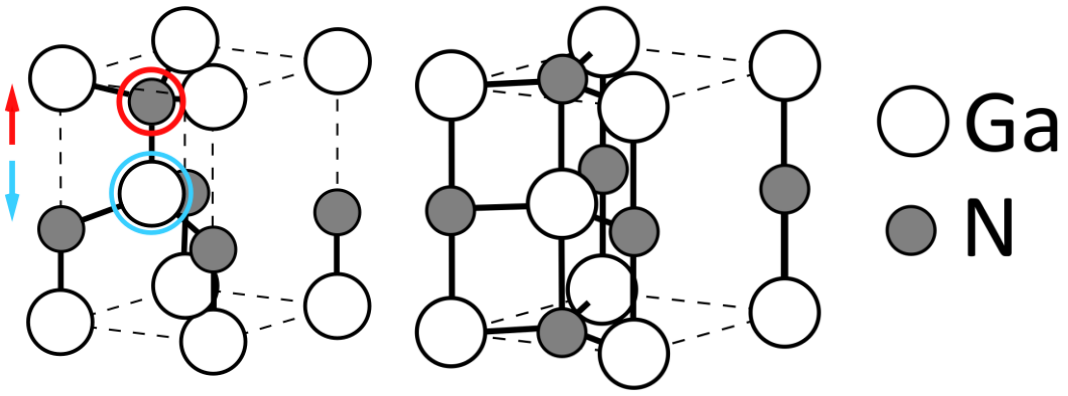

(a) (b)

Figure 2-3. Space group $P6_3mc$ and $P6_3/mmc$ corresponding to wurtzite and 2-dimensional layered hexagonal unit cells respectively.

Starting with the WZ structure **Figure 2-3 (a)** a single atom is moved up (denoted by the red circle) and another atom is moved down (denoted by the blue circle) i.e. going from a non-centrosymmetric system to a centrosymmetric system. These atoms are then moved back adiabatically to their original positions. Again, the corresponding change in polarisation is the required value as seen in **Equation 2-12**. This is the method for calculating the polarisation in the H reference frame i.e. P_{sp}^{H} and the 'improper' piezoelectric components e_{31}^{imp} and e_{33}^{imp}.

In both reference frames the e_{33} component has no alteration i.e. e_{33}^{imp} is the same as e_{33}^{prop}[124,125]. The values for the $P_{sp}^{ZB/\,H}$, $e_{31}^{prop/\,imp}$ and e_{33} constants and their different reference frames can be seen in **Table 2-4**.

Table 2-4. Polarisation constants for the zincblende P_{sp}^{ZB}, e_{31}^{prop}, e_{33} and the hexagonal reference frame P_{sp}^{H}, e_{31}^{imp}, e_{33}.

	AlN	GaN	BN	InN
P_{sp}^{ZB}/ C·m^{-2}	-0.090[80]	-0.035[80]	-0.012[69,70]	-0.053[80]
e_{31}^{prop}/ C·m^{-2}	-0.676[80]	-0.551[80]	0.282[69,70]	-0.604[80]
P_{sp}^{Href}/ C·m^{-2}	1.351[80]	1.312[80]	2.174[69,70]	1.026[80]
e_{31}^{imp}/ C·m^{-2}	-2.027[80]	-1.863[80]	-1.892	-1.63[80]
e_{33}/ C·m^{-2}	1.569[80]	1.020[80]	-1.068[69,70]	1.238[80]

The e_{31}^{imp} constant can be calculated using the formula $e_{31}^{imp} = e_{31}^{prop} - P_{sp}^{H}$ as seen in Dreyer *et al.*[80]

An interesting observation for the ZB reference frame (which contains the components P_{sp}^{ZB}, e_{31}^{prop} and e_{33}), is that WZ BN e_{31}^{prop} and e_{33} component both contain an opposite sign when compared to the other e_{31}^{prop} and e_{33} III-Nitride binary materials as seen in **Table 2-4**. For III-Nitride materials alloyed with BN, this results in a sign switch for the e_{31}^{prop} component as the incorporation of BN increases. However, this is not the case for the e_{31}^{imp} component which is used in the H reference frame. Further to this, increasing the B incorporation into III-Nitride materials also results in a sign switch for the e_{33} component which impacts both the H and ZB reference frame. All of these changes in sign in turn influence the polarisation sheet charge ($\sigma_b^{ZB/Href}$) which will be discussed further below.

Standard alloys of the III-N materials such as AlGaN/ GaN and InGaN/ GaN, show little difference when looking at the polarisation sheet charge as seen in **Equation 2-13** for ZB or H reference frames as seen by Dreyer *et al.*[80] This is not the case when alloying with BN.

$$\sigma_b^{ZB/H} = \Delta P_{sp}^{ZB/H} - 2\varepsilon_1 \left(e_{31}^{prop/imp} - e_{33} \frac{C_{13}^W}{C_{33}^W} \right) \quad 2\text{-}13$$

The $\Delta P_{sp} = P_{sp}^B - P_{sp}^W$ and $P_{pz}^{ZB/H} = 2\varepsilon_1 \left(e_{31}^{prop/imp} - e_{33} \frac{C_{13}^W}{C_{33}^W} \right)$ components of the polarisation were plotted separately first as seen in **Figure 2-4 (a)** and **(b)** for a $B_xGa_{1-x}N$/ GaN interface in the H and ZB reference frame respectively. It was assumed that the barrier material was unstrained and the QW was under tensile strain.

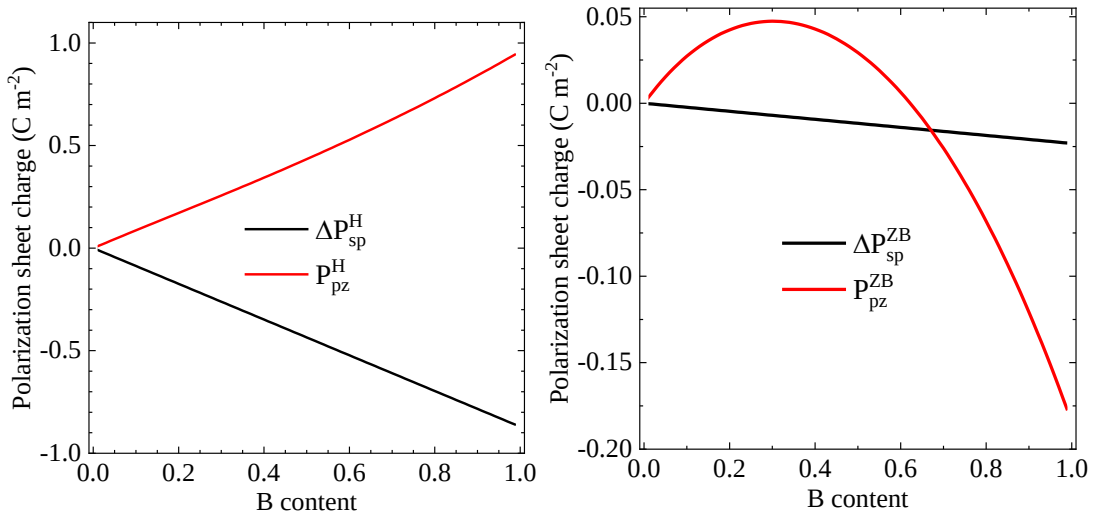

(a) (b)

Figure 2-4. Polarisation sheet charge components at the BGaN/ GaN interfaces, calculated using either the (a) H reference structure and e_{31}^{imp}, or the (b) ZB reference structure and e_{31}^{prop}.

As expected, using a linear interpolation for the spontaneous polarisation contribution (i.e. ΔP_{sp}^H and ΔP_{sp}^{ZB}) as seen in both **Figure 2-4 (a)** and **(b)** resulted in a straight line. The straight-line behaviour is also similarly seen in **Figure 2-4 (a)** for the P_{pz}^H component in the hexagonal reference frame. The magnitude of both the ΔP_{sp}^H and P_{pz}^H component seems to be similar in the H reference frame. This is not the case in the ZB reference frame where the contribution from the P_{pz} component seems to dominate over the majority of the ΔP_{sp} component. Further to this, a turning point also exists at ~0.3 for the P_{pz}^{ZB} component as seen in **Figure 2-4 (b)**. In the case of the P_{pz}^{ZB} component, initially, both the e_{31} and $-e_{33}\frac{C_{13}}{C_{33}}$ are additive. However, as BN

incorporation increases a sign switch occurs for the e_{31}^{prop} which can also be seen as the turning point in the plot.

The polarisation sheet charge (σ_b) density can be calculated using **Equation 2-13** where $P_{pz}^{ZB/H} = 2\varepsilon_1 \left(e_{31}^{prop/imp} - e_{33}\frac{C_{13}^W}{C_{33}^W}\right)$. A plot of the corresponding polarisation sheet charge for $B_xGa_{1-x}N$/ GaN can be seen in **Figure 2-5** assuming that the GaN region was unstrained and using the values from **Table 2-1** and **Table 2-4**.

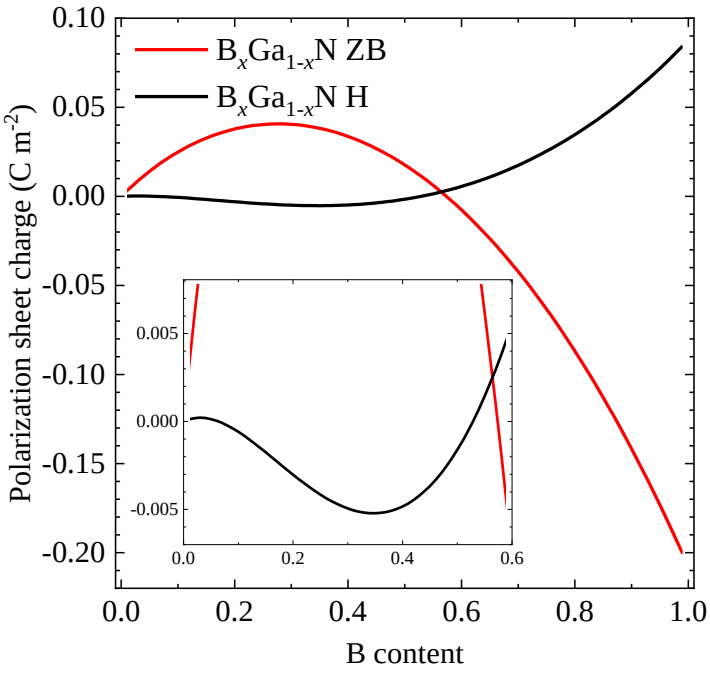

Figure 2-5. Polarisation sheet charges at the BGaN/ GaN interface are calculated using either the ZB reference structure and e_{31}^{prop}, or the H reference structure and e_{31}^{imp}.

From **Figure 2-5**, it is clear that the BGaN ZB and H reference frames contain very different polarisation sheet charges as a function of the boron content. In the ZB reference frame, a turning point exists at around B content of ~0.3. The origin of this turning point was discussed in the previous paragraph. Two turning points exist in the H reference frame at B contents of 0.03 and 0.35. Initially, the P_{sp} component dominates up to 0.03, then the negative P_{pz} component takes over due to the large e_{31}^{imp} component. Finally, the P_{sp} dominates again for B contents above 0.35. This

opposition between the ΔP_{sp} and P_{pz} component results in a much smaller polarisation sheet charge for B contents up to 0.6 when compared to the ZB case.

As a result, the H reference frame values i.e. P_{sp}^{H} and e_{31}^{imp} were the main values used for the simulation work in this thesis as the use of the ZB reference frame leads to incorrect values when working with B containing III-Nitride alloys.

2.4 Wavefunction overlap and emission energy

The finite different method (FDM) was used to solve the Schrödinger equation. The numerical technique is described in more detail in the **Appendix** to this thesis. A smaller QW is more beneficial as it results in a lower polarisation potential drop (as seen in **Figure 2-6** using **Equation 2-11**), thus resulting in a larger emission energy[126,127].

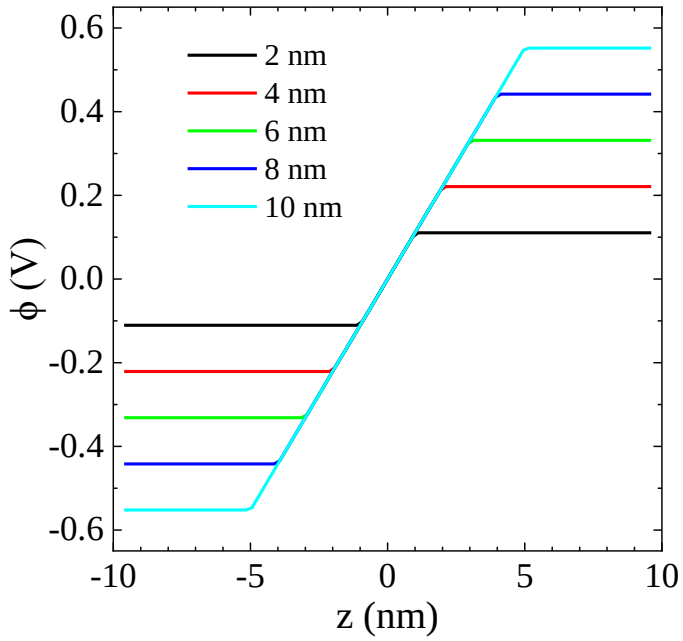

Figure 2-6. Polarisation potential for a GaN/ $Al_{0.15}Ga_{0.85}N$ SQW with varied QW size.

As our end goal is to grow the material in our reactor (which will be discussed later on in the thesis), the minimum thickness of the quantum well experimentally is also limited. Therefore a 2.5 nm SQW of $B_xGa_{1-x}N$/ $Al_yGa_{1-y}N$ was used. The FDM in one dimension was sufficient for our work as 3D would be computationally heavy.

As previously mentioned in **Section 1.3.3**, a different valence band and conduction band ordering exists between III-Nitride materials. Type-I band alignment is the desired band alignment for LEDs. The offset potential $U_{v/c}^{off}$ for both the conduction and valence band can be calculated using both $U_c^{off} = CBE^{QB} - CBE^{QW}$ and $U_v^{off} = VBE^{QW} - VBE^{QB}$ respectively. The energy gap bowing parameter b^{AlGaN} = 0.94 eV[35] and b^{BGaN} = 8.68 eV[25] is implemented in the conduction band (as seen in **Equation 2-14**) and a linear interpolation of the bulk materials is used for the valence band.

$$E_{gap}^{AlGaN} = 6x + 3.51(1-x) - 0.94x(1-x)$$

$$E_{gap}^{BGaN} = 13.2x + 3.51(1-x) - 8.68x(1-x) \qquad 2\text{-}14$$

Therefore, when a value of $U_{v/c}^{off} > 0$ is obtained for both the U_c^{off} and U_v^{off} then there is confinement in the well. The conduction and valence band offset potential were initially plotted for $B_xGa_{1-x}N$/ $Al_yGa_{1-y}N$ with varied Al (*y*-axis) and B (*x*-axis) content along with the strain component $S_{v/c}$ (**Equation 2-6**) as seen in **Figure 2-7 (a)** and **(b)**, to observe where type-I band alignment fails.

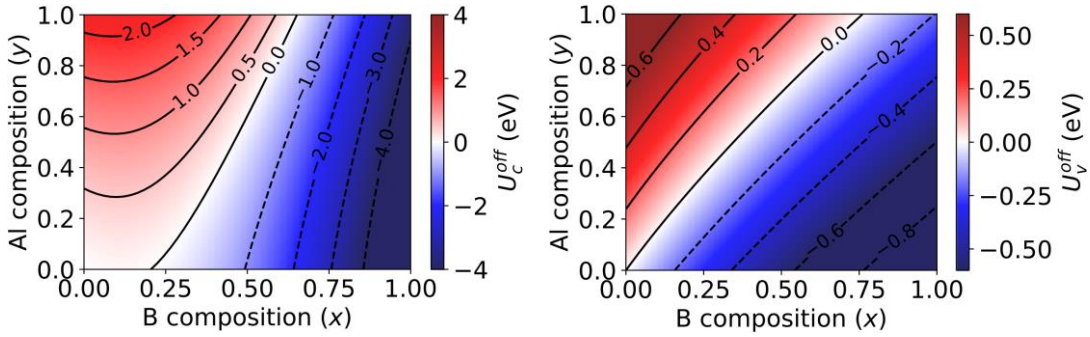

(a) (b)

Figure 2-7. (a) Conduction band and (b) valence band offset potentials for $B_xGa_{1-x}N$/ $Al_yGa_{1-y}N$.

The inclusion of the bowing parameter in the conduction band offset potential calculation results in a bending as seen by the '0.0' black line. A maximum boron incorporation of ~0.5 can be used in the QW to ensure that confinement still occurs in

the conduction band as seen in **Figure 2-7 (a)**. The choice of Al and B content in the QB and QW respectively can also result in Type-I and Type-II band alignment in the valence band as seen in **Figure 2-7 (b)**. As a results caution should be used when selecting the amount of Al and B in the QB and QW respectively.

The basal strain component $\varepsilon_{xx} = \frac{a_b - a_w}{a_w}$ was also plotted to understand where the QW and QB were closely lattice matched as seen in **Figure 2-8**.

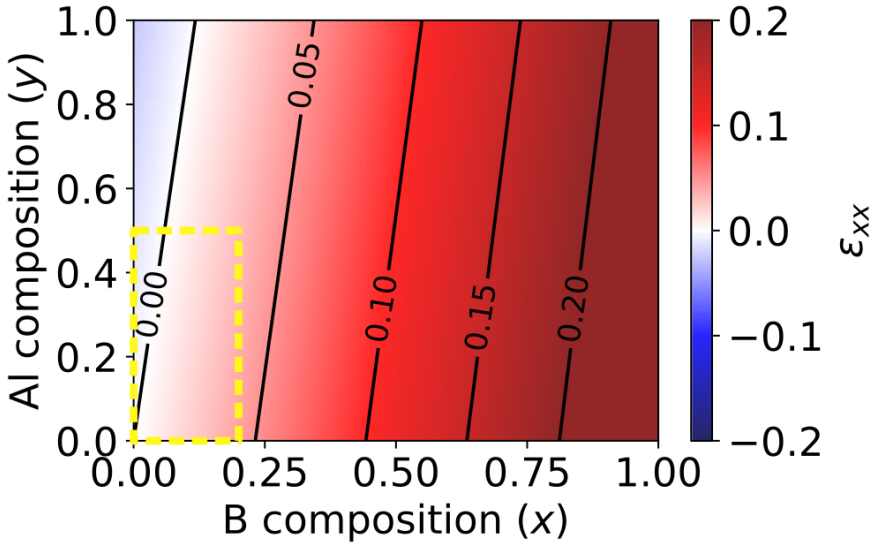

Figure 2-8. Basal strain component for $B_xGa_{1-x}N$/ $Al_yGa_{1-y}N$.

The blue and red region in the plot above denotes where the QW is under compressive and tensile strain, respectively. As a result, the region denoted in the yellow box was focused on in our theoretical work which corresponds to a maximum Al and B content of 0.5 and 0.2 in the QB and QW respectively.

The ΔP_{sp} and P_{pz}^{w} components were also plotted separately for the $B_xGa_{1-x}N$/ $Al_yGa_{1-y}N$ system as seen in **Figure 2-9**. From the results, using an Al content of 0.15 in the QB, a zeroing of the ΔP_{sp} and P_{pz} can be obtained for a BN content of <0.01 and slightly above 0.01 respectively.

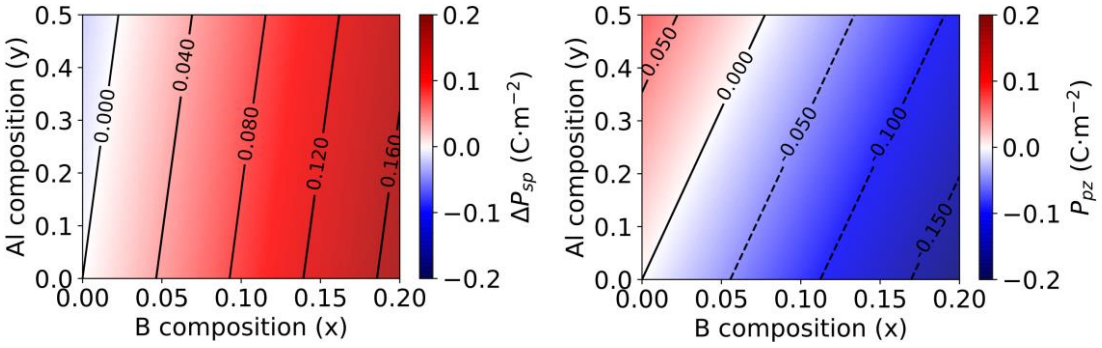

(a) (b)

Figure 2-9. Theoretical (a) ΔP_{sp} and (b) P_{pz}^{W} for $B_xGa_{1-x}N$/ $Al_yGa_{1-y}N$.

This initial reduction in polarisation with the addition of boron was also noted from the wavefunction overlap $\Psi^{overlap}$ for a $B_xGa_{1-x}N$/ $Al_yGa_{1-y}N$ SQW of 2.5 nm as seen in **Figure 2-10**. As mentioned previously, FDM was used to solve the Hamiltonian in matrix form. The energy eigenvalues and eigenvectors are calculated from the Hamiltonian. The diagonal eigenvalues along with the corresponding eigenfunction/ wavefunction can then be plotted. The electron (Ψ_e) and hole (Ψ_h) wavefunctions were then used to calculate the $\Psi^{overlap}$ as seen in **Equation 2-15**.

$$\Psi^{overlap}(z) = |\langle \Psi_h | \Psi_e \rangle|^2 = \left| \int_{-\infty}^{\infty} \Psi_h^* \Psi_e \, dz \right|^2 \qquad 2\text{-}15$$

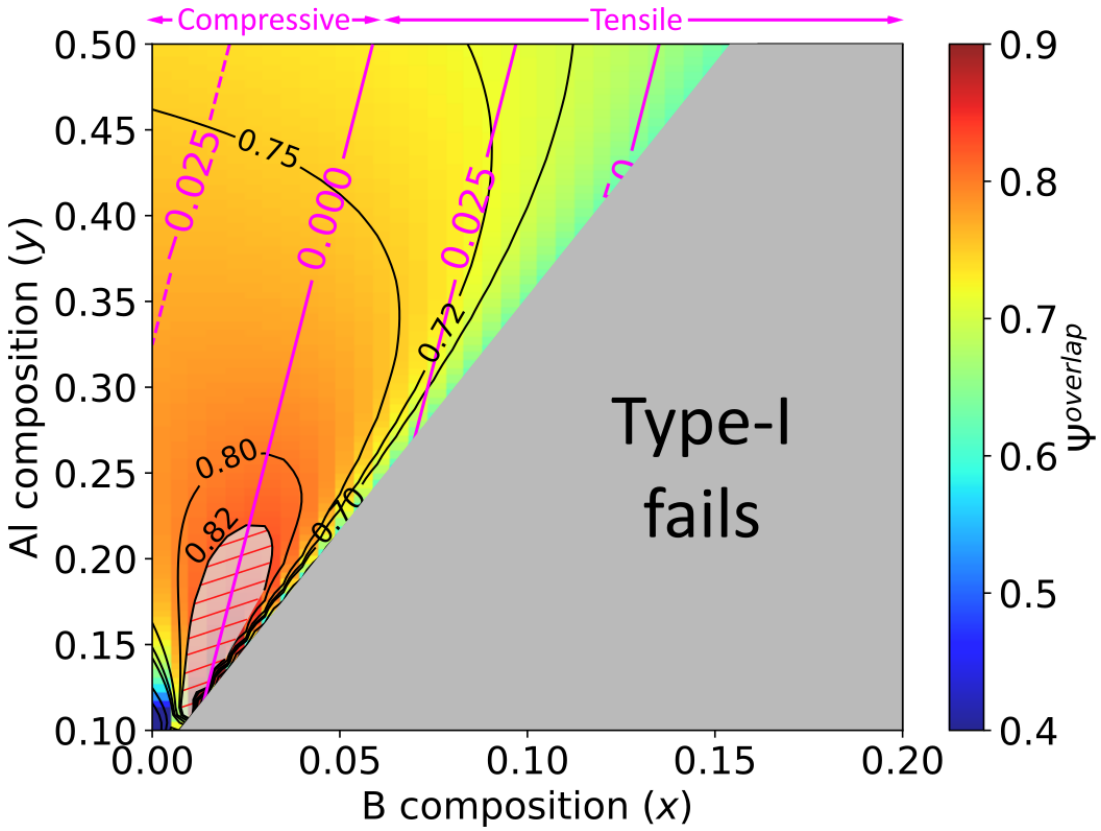

Figure 2-10. Wavefunction overlap for a 2.5 nm SQW of $B_xGa_{1-x}N$/ $Al_yGa_{1-y}N$.

The diagonal magenta lines represent the lattice mismatch between the materials. The region of interest is highlighted in white and red dashed lines which is associated with low Al incorporation in the QB and low B in the QW. The area highlighted in white with red dashed lines is also where the two materials are closely lattice-matched which is more beneficial for experimental growth. The results indicate an Al content of ~0.15 in the QB along with a B content of ~0.01 are the optimum conditions for the highest wavefunction overlap. An increase of ~10% was observed for a $B_{0.01}Ga_{0.99}N$/ $Al_{0.15}Ga_{0.85}N$ SQW when compared to a standard GaN/ $Al_{0.15}Ga_{0.85}N$.

The incorporation of BN appears to have little effect on the emission energy of the SQW as seen in **Figure 2-11**.

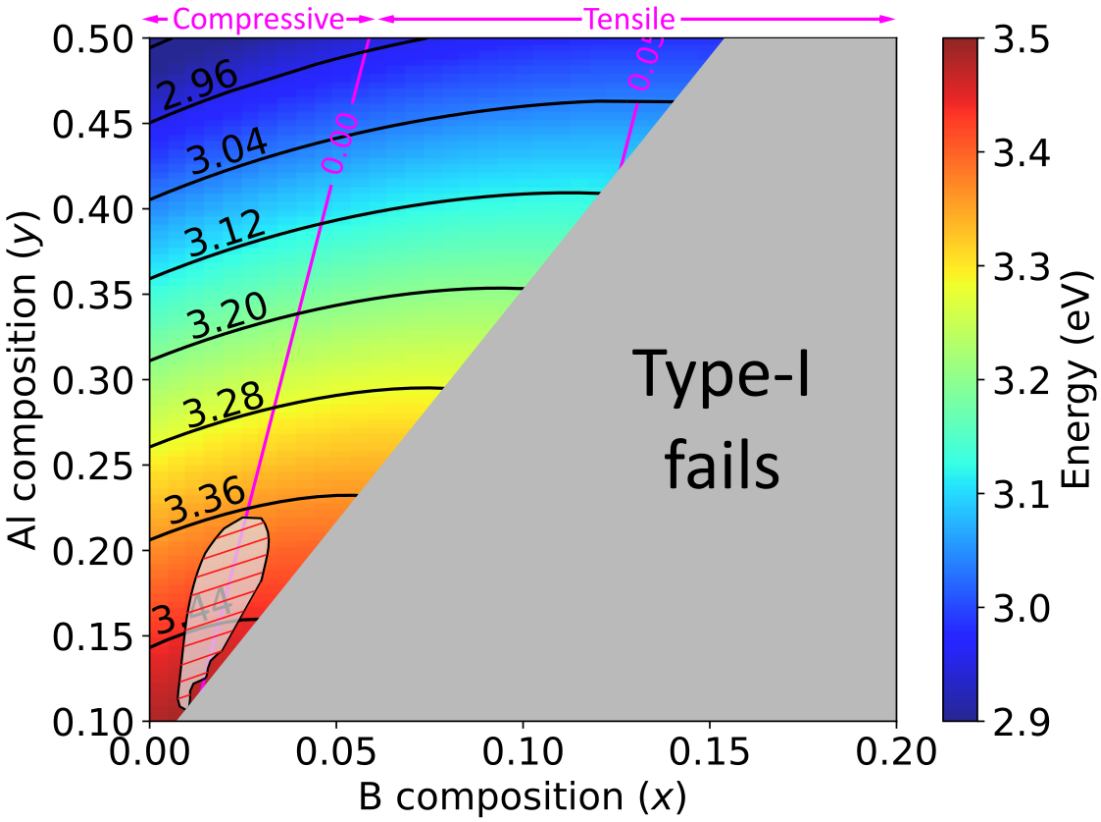

Figure 2-11. Emission energy for a 2.5 nm SQW of $B_xGa_{1-x}N$/ $Al_yGa_{1-y}N$.

An emission energy of 3.5 eV and 3.43 eV was obtained for $B_{0.01}Ga_{0.99}N/Al_{0.15}Ga_{0.85}N$ and GaN/ $Al_{0.15}Ga_{0.85}N$ respectively. Further to this, in the region of 0.15 Al content in the barrier, a slight blueshift is observed for B content <0.01, followed by a redshift as B content increases above 0.01. This is due to an initial strain improvement, as the QW becomes lattice matched to the QB, resulting in a reduction in the P_{pz} component and also only a small contribution from the ΔP_{sp} component to the overall polarisation. However, as the B content increases the large P_{sp} component dominates resulting in a redshift.

2.5 Conclusion

From the theoretical literature, it is clear that there are many advantages of alloying B with III-Nitride materials. Our theoretical results show that low contents of BN ~0.01 in a SQW along with low Al incorporations of ~0.15 into the QB appears to improve the wavefunction overlap along with a slight blueshift followed by a redshift in the emission energy. This initial improvement in the wavefunction overlap is due to a

reduction in polarisation and an improvement in strain engineering. However, increasing the B content in the QW results in both an increase in tensile strain and polarisation. The theoretical results in this chapter guided the Al and B concentrations focused on in **Chapter 5**.

3 EXPERIMENTAL TECHNIQUES

The main material growth system used in this thesis along with other material characterisation tools such as structural, morphological and optical techniques will be discussed in this chapter.

3.1 Epitaxy

Epitaxy is the process of growing layers of crystalline material on the same (homoepitaxy) or different (heteroepitaxy) substrate material. Complicated heterostructures such as LEDs, vertical-cavity surface-emitting lasers (VCSELs), etc. can thus be obtained. The term "epitaxy" is constructed from the Greek language with the meaning "ordered upon", where the term "epi" means on/ to/ above and "taxy" means order/ ordering.

Some of the most commonly used chemical vapour deposition (CVD) epitaxy techniques include; halogen vapour phase epitaxy (HVPE)[128,129], metalorganic chemical vapour deposition (MOCVD)[128–130] and molecular beam epitaxy (MBE)[128,131].

3.1.1 Halogen vapour phase epitaxy

In HVPE, group-III nitrides are formed by reacting hot gaseous metal chlorides with NH_3. A simple schematic of the process can be seen in **Figure 3-1**.

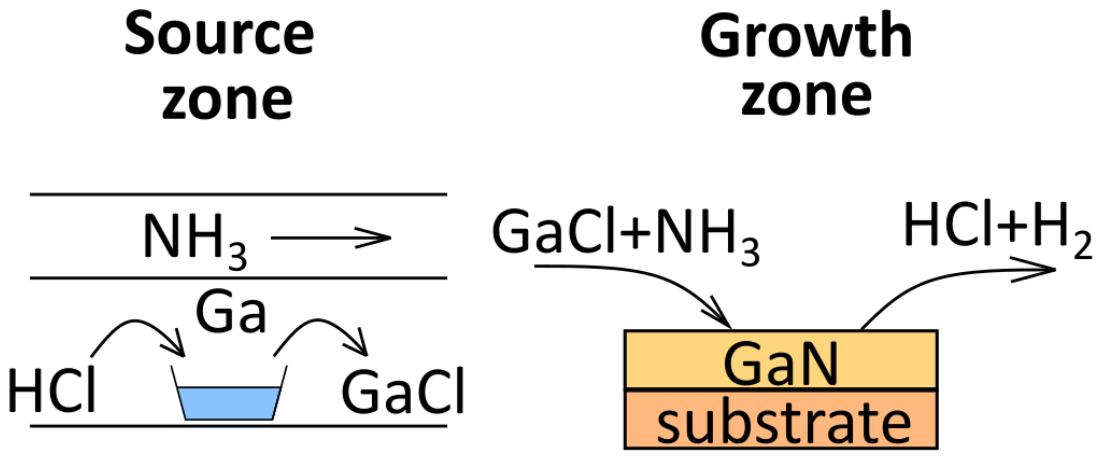

Figure 3-1. Schematic of a halogen vapour phase epitaxy (HVPE) process for GaN.

The first growth of GaN was achieved using the HVPE process[132,133]. In HVPE, group-III elements are transferred into the reactor as *halides* and group-V atoms are introduced as *hydrides*. For GaN growth, the halide and hydride precursors used are gallium chloride (GaCl) and NH_3 respectively. Pure metallic Ga is heated in a crucible and exposed to the hydrogen chloride, where the H_2 carrier gas is then passed through, where they react with NH_3 to form GaN with the by-products of H_2 and hydrochloric acid (HCl) as seen in **Equation 3-1**.

$$GaCl + NH_3 \rightarrow GaN + HCl + H_2 \qquad 3\text{-}1$$

3.1.2 Molecular beam epitaxy

A simple schematic of an MBE reactor can be seen in **Figure 3-2,** which usually consists of an ultra-high vacuum chamber ~10^{-8} Pa.

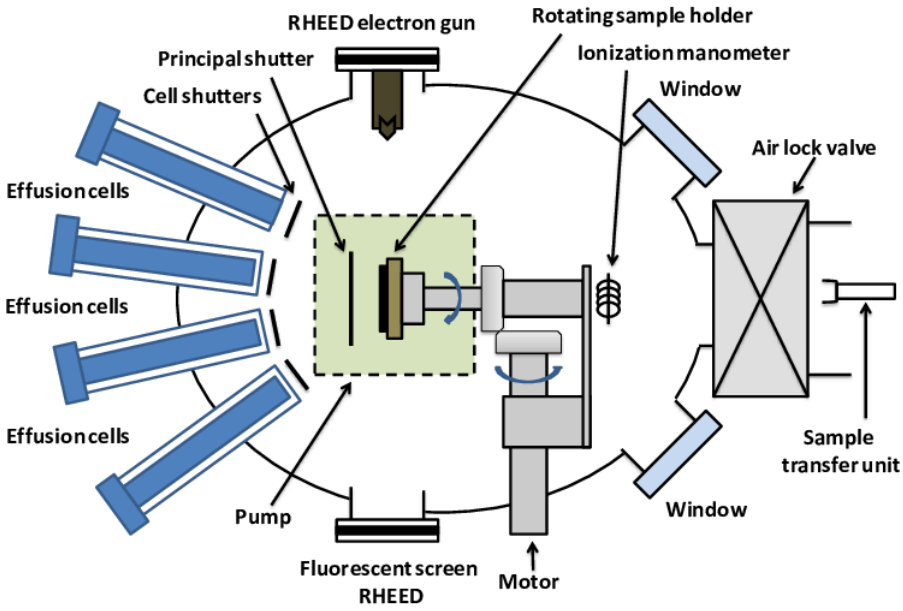

Figure 3-2. Schematic of a molecular beam epitaxy (MBE) reactor[134].

The group-III metals and dopant atoms are in a solid source stored in (Knudsen) effusion cells[135]. The cells are heated to a temperature where the elements evaporate, the shutters are opened, and an atomic beam strikes the hot substrate[131]. Due to the high vacuum, the atoms have a mean free path for collisions longer than the

source-to-substrate distance. The atoms react on the substrate surface and the material can be grown layer by layer in two dimensions. In-situ characterisation of the sample can be achieved during growth using a reflection high-energy electron diffraction (RHEED) gun. Information such as the sample's quality, thickness and surface morphology can be obtained.

Nitrogen cannot be stored in the effusion cell and, as a result, other techniques are implemented such as plasma-assisted MBE in which the nitrogen radicals are produced by radio-frequencies[128,131].

Another popular epitaxy technique especially in the industrial mass-production of semiconductor materials growth is MOCVD. This was the main epitaxy technique used in our work and will be described in detail in the next section.

A summary of the main strengths and weaknesses of the CVD epitaxy techniques can be seen in **Table 3-1**.

Table 3-1. Overview of epitaxy techniques[136].

Technique	Strengths	Weaknesses
HVPE	Well developed Large scale High growth rates	Complex process/ reactor Hazardous precursors
MBE	Simple process Uniform Abrupt interfaces In-situ monitoring	N materials difficult Expensive Low throughput
MOCVD/ MOVPE	Most flexible Abrupt interfaces High purity Robust process Large scale Selective growth In-situ monitoring	Expensive reactants Hazardous precursors

3.1.3 Metal-organic chemical vapour deposition

MOCVD involves the decomposition of metal-organic (MO) precursors to produce a thin film of the desired material. MOCVD is widely used in the production of semiconductor devices, such as LEDs, solar cells, and other electronic devices. In MOCVD, metalorganic compounds are used for the group-III source precursors along with NH_3 as the nitrogen source. The composition and growth rate of the film can vary depending on the growth temperature, reactor pressure, dilution of the precursors and flow rate of the precursors. MOCVD was the main epitaxy growth method used in this thesis.

An AIXTRON 3x2” vertical reactor which uses the closed-coupled showerhead technology originally developed by the British company Thomas Swan was used to grow all of the samples discussed in this thesis[137]. A picture of our reactor can be seen in **Figure 3-3**.

Figure 3-3. AIXTRON Close coupled showerhead reactor.

Reaction process in MOCVD reactor

Some common MOs used in MOCVD include; trimethylaluminium (TMAl) as the aluminium source, trimethylgallium (TMGa) as the gallium source, triethylboron (TEB) as the boron source and trimethylindium (TMIn) as the indium source. The precursor choice depends on the material being deposited and the desired properties of the resulting thin film. Doping of the material during growth can be achieved by supplying a controlled amount of dopants such as disilane or biscyclopentadienylmagnesium (Cp_2Mg) into the reactor for *n* and *p* doping respectively.

Some of the key chemical reactions involved in a MOCVD reactor can be seen in **Figure 3-4**.

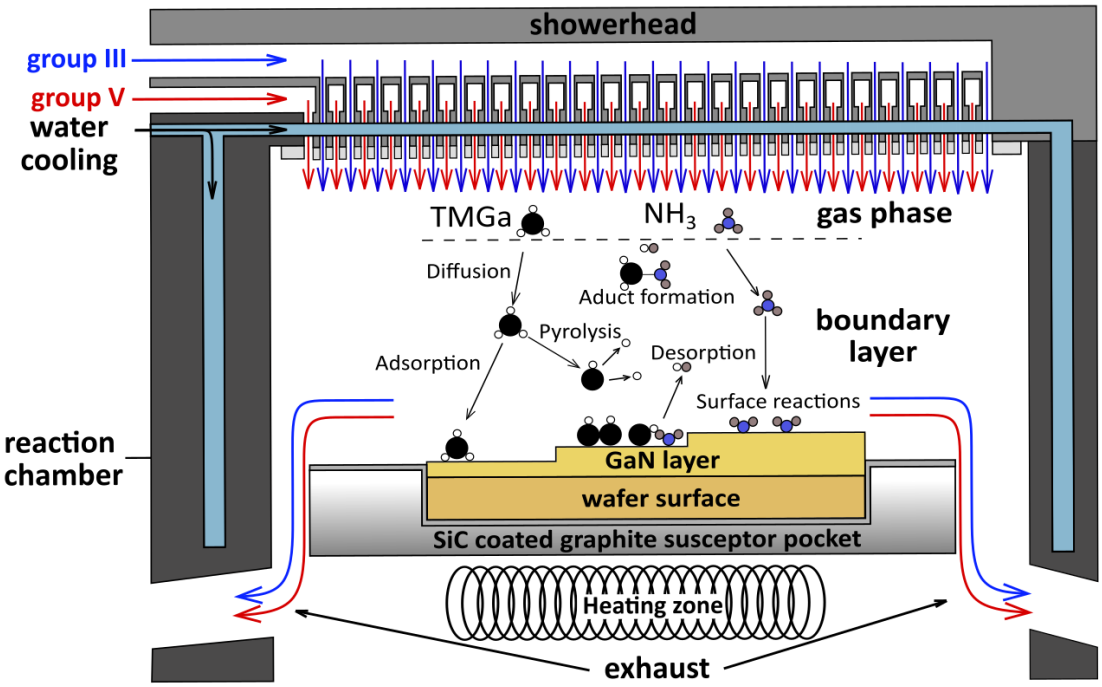

Figure 3-4. CVD process in an MOCVD reactor and on the substrate surface.

The substrates can be placed into a 'pocket' on the graphite susceptor. The MOs and NH_3 are supplied from the top of the reactor where the lid of the reaction chamber contains a similar shape to that of a "showerhead". This showerhead design contains an alternating array of holes that enable independent precursor injection, corresponding to two separate gas lines for the MOs and NH_3. (as seen by the red and

blue arrows). This injection separation also helps to minimize the pre-reactions of the MOs and NH_3 as they are supplied through different inlets in alternating positions and only come into contact close to the surface of the substrate. Rotation of the susceptor is also possible to improve the growth uniformity of the layers.

The boundary layer refers to the thin region adjacent to the surface of the substrate (as seen in **Figure 3-4**) where chemical reactions occur. The growth and quality of the epitaxial grown thin layers are influenced by the conditions within this boundary layer as the MOs and NH_3 must pass through this layer before reaching the substrate surface[138,139].

High temperature is used during the growth process which allows the decomposition of the MOs and form pyrolysis products. Adsorption occurs on the surface of the substrate with these decomposed products and they can diffuse to available growth sites. The reaction by-products are extracted from the reactor chamber through the exhaust.

Many thermodynamic reactions occur during the growth process, however, a general simplistic reaction in the MOCVD process can be written as seen in **Equation 3-2**.

$$A^{III}R_3 + B^V X_3 \rightarrow A^{III}B^V + by\ products \qquad 3\text{-}2$$

The group III alkyls are denoted by $A^{III}R_3$ where R_3 is an organic radical and A^{III} is a group-III metal. The binary hydrogen compound of group V is denoted $A^{III}B^V$ where B^V is a non-metal from group-V. This subsequent reaction results in the epitaxial growth on the heated substrate. The main idealised reactions for AlN, GaN and BN can be seen in **Equation 3-3** along with a summary of the main parameters for III-nitride MOCVD material growth in **Table 3-2**.

The values provided in **Table 3-2** are for general reference only, as the growth recipes created by various research groups with different reactors may differ.

$$Al(CH_3)_3 + NH_3 \rightarrow AlN + 3CH_4$$

$$Ga(CH_3)_3 + NH_3 \rightarrow GaN + 3CH_4$$

$$B(C_2H_5)_3 + NH_3 \rightarrow BN + 3C_2H_6 \qquad 3\text{-}3$$

Table 3-2. Typical MOCVD growth parameters used in our reactor.

	Carrier gas	Temperature (°C)	Pressure (mbar)	V/III ratio
GaN	H_2	~1050	~100	~1000
AlN	H_2	1100-1300	~50	~50

The MOs are usually in a solid or liquid phase and stored in bubblers where a carrier gas nitrogen/ hydrogen can be flowed through, picking up the precursors as vapours. The temperature of the bubbler is fixed, resulting in the desired partial pressure of the MOs. The flow rate of the MOs (f_{MO}) into the MOCVD reactor then depends on the flow rate of the carrier gas (f_{H_2/N_2}) along with the pressure of the bubbler $(P_{Bubbler})$ and MO partial pressure (P_{MO}) which can be calculated using **Equation 3-4**.

$$f_{MO}\left(\frac{\mu mol}{min}\right) = \frac{f_{H_2/N_2}}{22400\left(\frac{sccm}{\mu mol}\right)} \cdot \frac{P_{MO}}{P_{Bubbler} - P_{MO}} \qquad 3\text{-}4$$

This MO partial pressure can be rewritten in terms of the temperature (T) and the temperature coefficients A, B, C using Antoine's equation[140] (**Equation 3-5**).

$$\log[P_{MO}] = B - \frac{A}{T + C} \qquad 3\text{-}5$$

The main MOs used in this thesis along with their melting points and A, B, C temperature coefficients can be seen in **Table 3-3**.

Table 3-3. Physical properties of the main metalorganic sources used in this work[141–143].

Symbol	Chemical	A	B	C	Melting Point (°C)	Remark
TMGa	Trimethylgallium $(CH_3)_3Ga$	1703	8.07	0	-15.8	Primary gallium source
TMAl	Trimethylaluminium $(CH_3)_3Al$	2134.8	8.224	0	15.4	Primary aluminium source
TEB	Triethylboron $(C_2H_5)_3B$	753.261	2.91408	112.631	-93	Primary boron source
Cp_2Mg	Cyclopentadienylmagnesium $(C_5H_5)_2Mg$	3556	10.56	0	175	*p*-doping

Three different growth regimes are possible during epitaxial growth as seen in **Figure 3-5**[144], depending on the growth rate and temperature[145,146].

- At lower temperatures, the growth rate is restricted by reaction kinetics, which means that the slowest reaction in the gas phase or at the surface limits the growth rate.
- As the growth temperature increases, so does the growth rate until it is limited by mass transfer through the boundary layer. The growth rate in this region is relatively independent of the growth temperature, and the growth rate is instead controlled by the partial pressures of the precursors.
- Further temperature increase results in the growth rate decreasing. This region is referred to as the thermodynamically limited regime and the decrease in the growth rate is due to several factors: parasitic side reactions in the gas phase, an increase in deposition on the reactor walls and an increase in desorption of atoms from the growing film[147].

These regimes are not mutually exclusive, and the growth process can switch between them depending on the MOCVD system's unique parameters. In practice, the goal is

to maintain good film quality and uniformity while operating in a regime that maximises deposition rate.

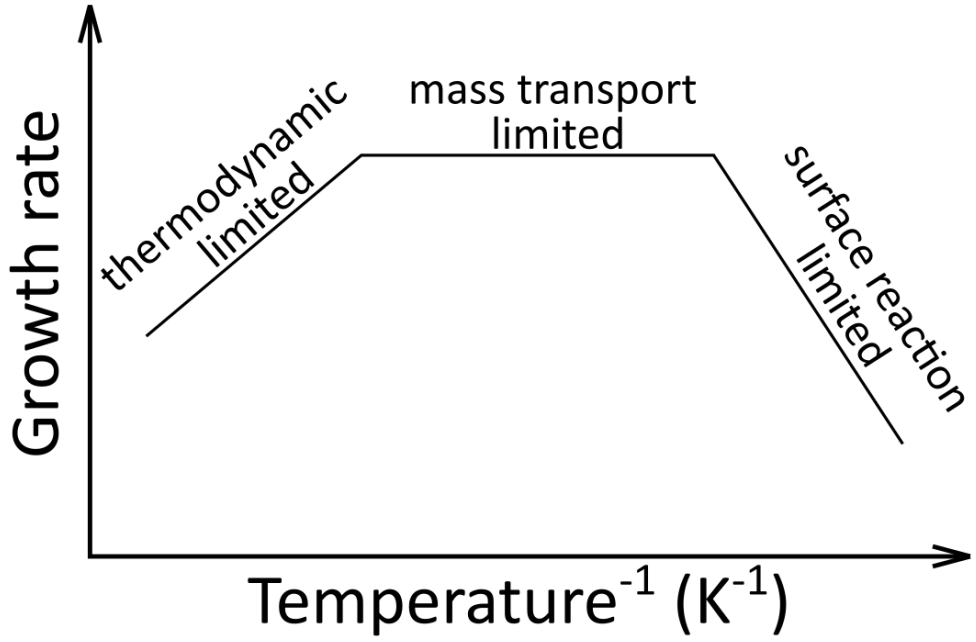

Figure 3-5. CVD growth mechanisms as a function of reciprocal temperature.

The Close Coupled Showerhead (CCS) reactor is one of the most commonly used showerhead for III-Nitride material growth[148,149]. It allows a uniform injection and thus potentially uniform growth, and a short distance between the (separate) injection of the ammonia and group III precursor limits the opportunity for gas phase (parasitic) reactors to occur (as seen in **Figure 3-4**). It has been reported in literature that the CSS MOCVD reactor has problems with Ga contamination during the growth of InAlN, when the Ga precursor line is turned off[150–156]. In the case of InAlN growth, residual Ga remains on the wafer susceptor, quartz liner and even on the showerhead surface[150,154]. Mrad *et al.*[157] was able to reduce the contamination of Ga in their InAlN films by mounting a SiC coated graphite deposition shield on the showerhead. Deng *et al.*[158] was able to achieve Ga free InAlN films by chemically treating the quartz liner and wafer susceptor. This parasitic effect in reactors mean that the possibility of reactor history affecting growth need to be considered when depositing materials systems that are relatively unexplored.

Literature reports show that the growth of hexagonal BN with TEB precursor in a CCS reactor, results in parasitic reactions in the chamber along with a memory effect[159,160]. This undesirable contamination could also be a possibility when working with boron-containing III-Nitride materials and, while not a focus in this work, is one that merits more detailed investigation in future. Indeed, the area of reactor history effects is one that has not been fully explored for MOVPE more generally. For example, even recently the impacts on the growth of AlN on AlGaN has been found to show unusual grading[161] and for doping Mg in GaN a detailed review can be found in Ohba *et al.*[162] and Xing *et al.*[163]. This issue is also not unique to GaN. Even recently, work to fully understand the issues of reactor history and growth condition for Zn doping of conventional III-V has led to new insights[164].

3.2 Structural and surface morphology techniques

After the material is grown, in-depth ex-situ characterisation can be performed to determine the structural, optical and surface properties of the grown structure.

3.2.1 X-ray diffraction

X-ray diffraction (XRD) involves probing a crystal with X-ray radiation of wavelength λ, which has a wavelength close to the crystal spacing. The XRD equipment used in this work was a Malvern Panalytical X-pert MRD XRD and a schematic of the setup can be seen in **Figure 3-6**.

The $K_{\alpha 1}$ radiation from the copper anode at a wavelength of 1.541 Å was selected with a hybrid monochromator which was composed of a graded parabolic mirror and a (220) channel-cut Germanium crystal. The $Cu_{K_{\alpha 2}}$ component from the beam is filtered by the Ge crystal. An Euler cradle is used to hold the sample which allows a variation in the incident angle (ω), the diffraction angle (2θ), the angle around the surface normal (ϕ) and the angle around an in-plane horizontal direction (χ) as seen in **Figure 3-7**.

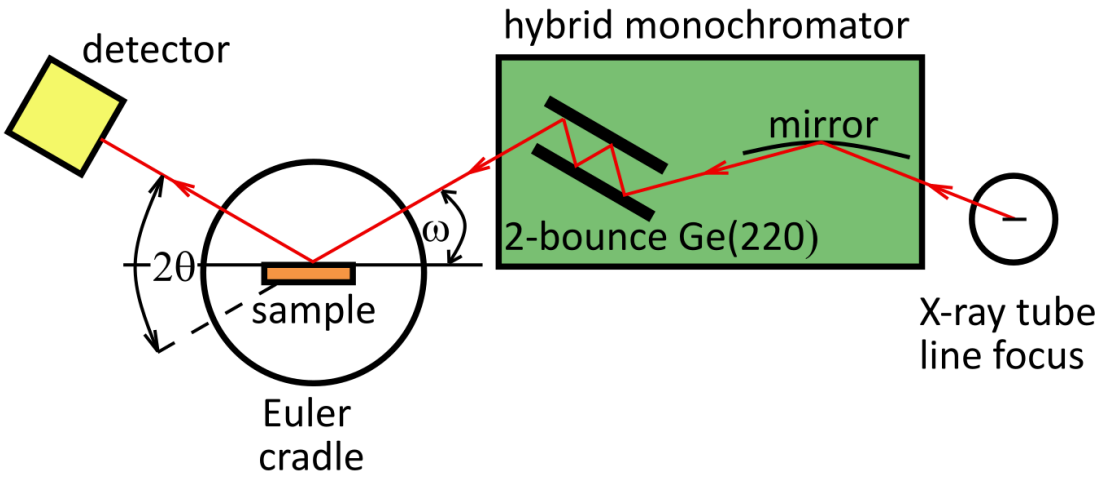

Figure 3-6. Schematic of X-ray diffraction setup.

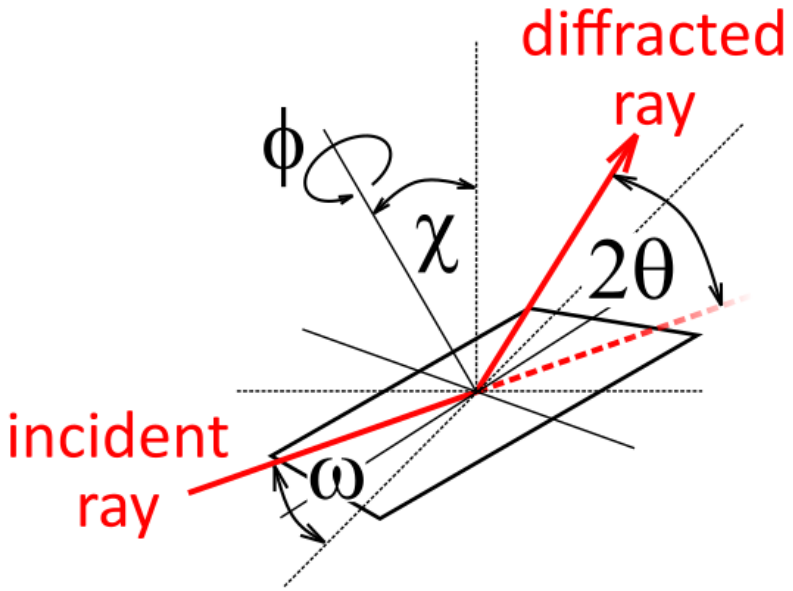

Figure 3-7. Axes and angles in a standard XRD measurement.

The scattering angle of the incident ray can be calculated using Bragg's law[165] as seen in **Equation 3-6** and the main principle can be seen in **Figure 3-8**.

$$n\lambda = 2d_{hkl}sin\theta \qquad 3\text{-}6$$

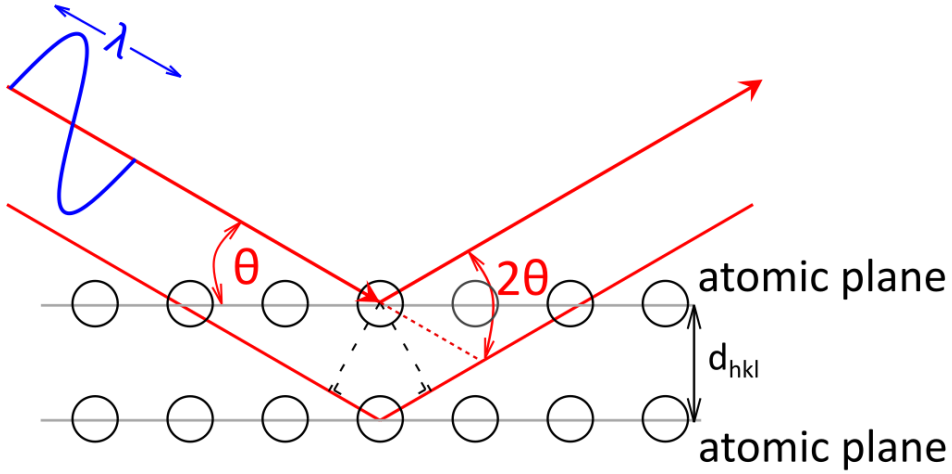

Figure 3-8. Schematic illustrating Bragg's law.

The distance between planes/ interplanar spacing is denoted by d_{hkl}, θ is the incident angle (for a symmetric scan which will be discussed in detail below) and hkl are the Miller indices. The difference in path length can lead to constructive and destructive interference depending on the in/out of phase of the waves.

The theoretical interplanar spacing (d_{hkl}) can be determined using **Equation 3-7**[166], for a hexagonal layered structure, which allows for information to be determined such as the composition of the molecular and atomic structure of a crystal, strain in the material, superlattice thickness etc.

$$\frac{1}{d_{hkl}^2} = \frac{4}{3}\frac{(h^2 + hk + k^2)}{a^2} + \frac{l^2}{c^2} \qquad 3\text{-}7$$

The separation in the atomic planes can also be used to determine the scattering vector $\overline{\boldsymbol{S}}$ as shown in **Figure 3-9**.

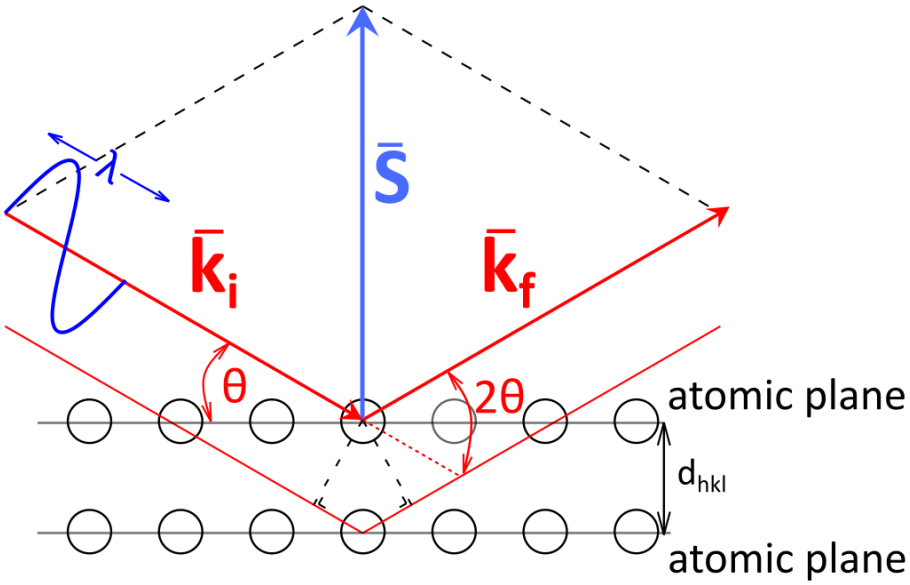

Figure 3-9. Illustration of the incident, diffracted and scattering vectors.

The terms $\overline{\boldsymbol{k}}_{\boldsymbol{i}}, \overline{\boldsymbol{k}}_{\boldsymbol{f}}$ and $\overline{\boldsymbol{S}}$ represent the incident, diffracted and scattering vectors which can be used to calculate the reciprocal lattice. The scattering vector $\overline{\boldsymbol{S}} = \overline{\boldsymbol{k}}_{\boldsymbol{i}} + \overline{\boldsymbol{k}}_{\boldsymbol{f}}$ and can be varied by changing ω and 2θ. $\overline{\boldsymbol{S}}$ will end at a reciprocal lattice point and as a result, various areas of reciprocal space can be probed by varying the crystal direction and the magnitude of $\overline{\boldsymbol{S}}$. The magnitude of $\overline{\boldsymbol{S}}$ can be altered by varying the incident angle (θ) and 2θ.

The film quality can be determined using ω-scans which are also known as rocking curve scans as the sample is 'rocked'. The detector is fixed at a 2θ angle for the corresponding reflection that is required to be measured. A mosaic spread of the crystal is obtained by measuring around the reciprocal plane. The full-width half maximum (FWHM) of the required peak is obtained which contains information such as dislocation densities and wafer bow[167,168].

For an ω-2θ scan, the integrated intensity of the reflection from the sample is measured. With this scan, we move radially away from the centre of the reciprocal plane, and information such as the interplanar spacing can be determined.

As mentioned in **Chapter 1**, heteroepitaxy results in compressive and tensile strain. If the material is strained to the underlayer, then the corresponding *c*-lattice constant can

be calculated using **Equation 3-8**[166] which contains the theoretical and the strained/ measured lattice constants (a_o, c_o) and (a_{meas}, c_{meas}) respectively, and the elastic constants C_{13}, C_{33}.

$$\frac{c_{meas} - c_o}{c_o} = -2\frac{C_{13}}{C_{33}}\frac{a_{meas} - a_o}{a_o} \qquad 3\text{-}8$$

However, if the material is in an unknown strain state the lattice parameters *a* and *c* must be measured by both a symmetric and asymmetric/ skew-symmetric ω-2θ scan as seen in **Figure 3-10**.

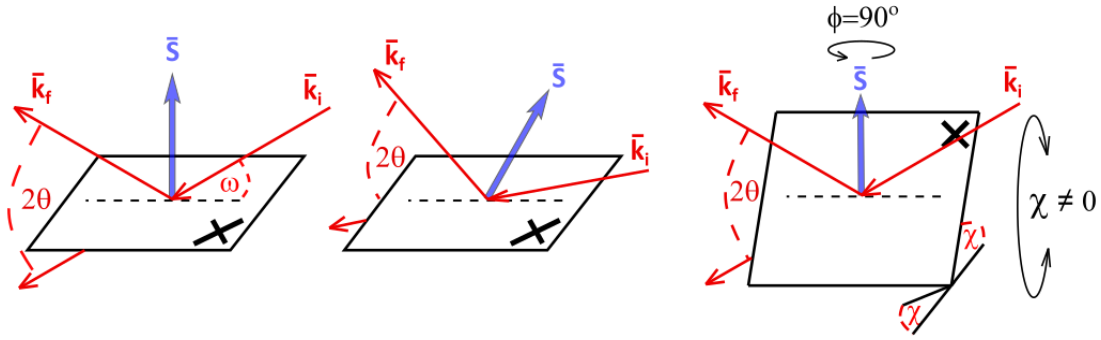

(a) (b) (c)

Figure 3-10. X-ray diffraction (a) symmetric, (b) asymmetric and (c) skew-symmetric scans.

With a symmetric scan the incident angle θ is equal to the sample tilt ω and the measurement of the planes is parallel to the surface of the material as seen in **Figure 3-10 (a)**. A variation of the *c*-lattice constant of the material in the 002 plane which is parallel to the 001 or *c*-plane is measured. This is in contrast to an asymmetric/ skew-symmetric scan where the sample tilt is not equal to the incident angle, as a result, a combination of the *a* and *c* lattice parameters are measured with ideally a small contribution from the *c*-plane. Relaxation of the material can also be calculated using a combination of these scans.

This is in contrast to an asymmetric scan where $2\theta \neq 2\omega$ and ω contains an offset value as seen in **Figure 3-10 (b)**. The sample is rotated by unequal angles on either

side of the incident beam i.e. the sample is rotated to a specific angle on one side of the beam before being rotated to a different angle on the other.

In a skew-symmetric scan, the sample is initially rotated at an angle of ϕ=90° as seen in **Figure 3-10 (c)**. The sample is then rotated perpendicular to the growth plane by equal amounts on either side of the incident beam $\overline{\boldsymbol{k}_i}$ at an angle χ. The resulting diffraction pattern will be symmetric in relation to the incident beam and will contain information on the crystal symmetry and relative orientation of the crystal planes.

As a result, skew-symmetric scans can be used to determine crystal symmetry and identify crystal planes, while the asymmetric scan is used to determine lattice parameters, strain, and defects in the crystal lattice.

A distribution in the diffraction intensity of one (hkl) point in reciprocal space can also be observed by using a reciprocal space map (RSM). RSM scans show the structural information which can be used to determine the strain and composition profile of the material. A simple RSM scan can be seen in **Figure 3-11**[166], where AlGaN is grown strained and relaxed on top of the GaN buffer layer.

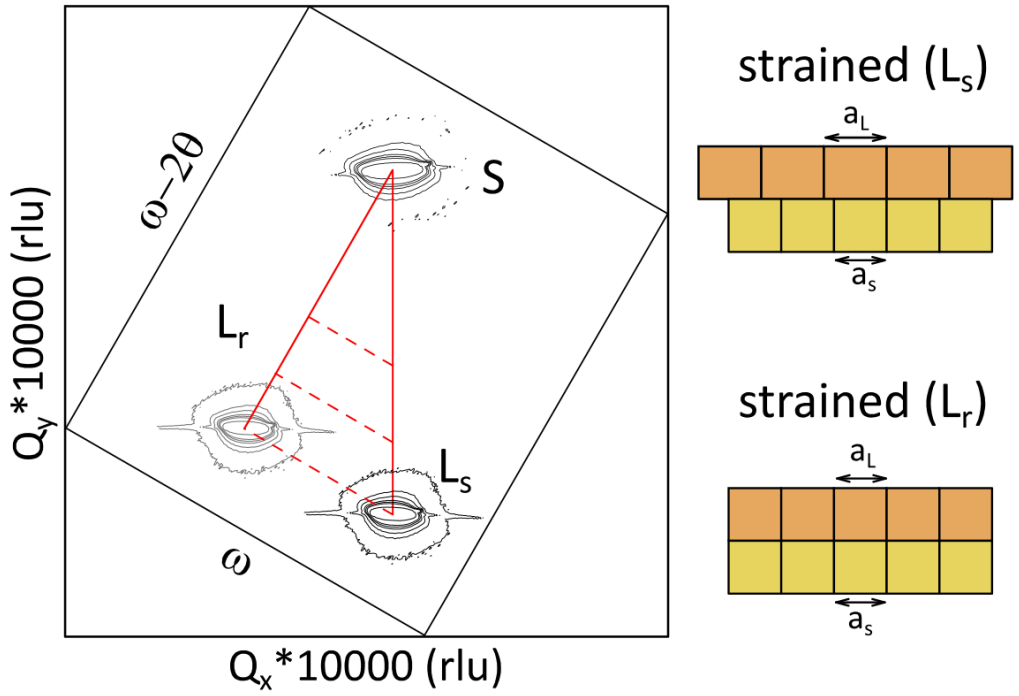

Figure 3-11. Reciprocal space map of strained and relaxed AlGaN film (L) on a thick GaN buffer layer (S).

The grey reciprocal lattice point (L_r) and black reciprocal lattice points (L_s) denote the AlGaN strained and relaxed to the GaN buffer respectively. The vertical and diagonal solid red line corresponds to the theoretical value of the GaN *a*-lattice parameter and the relaxed *a*-lattice parameter of the AlGaN layer respectively. The diagonal dashed lines correspond to different concentrations of the AlGaN layer.

In RSM scans the angular positions $(\omega, \omega\text{-}2\theta)$ are often expressed in terms of the diffraction space coordinates (Q_x, Q_y) as seen in **Equation 3-9**[169] where the angle θ and ω can be calculated using **Equation 3-6** and **Equation 3-10**, respectively.

$$(Q_x, Q_y) = \frac{1}{2}(cos\omega - cos(2\theta\text{-}\omega), sin\omega + sin(2\theta\text{-}\omega)) \quad 3\text{-}9$$

$$tan\omega = \frac{\frac{1}{5}c}{\frac{\sqrt{3}}{2}a} \quad 3\text{-}10$$

The main parameters used in the RSM calculations can be seen in **Table 3-4**.

Table 3-4. Main wurtzite III-Nitride parameters used in X-ray diffraction calculations.

	AlN	**GaN**	**BN**
a/ Å	3.112[30]	3.189[30]	2.534[29]
c/ Å	4.982[30]	5.185[30]	4.189[29]
C_{13}/ Pa	108[30]	106[30]	64[29]
C_{33}/ Pa	373[30]	398[30]	1113[29]

3.2.2 Scanning electron microscopy/ Transmission electron microscopy

With an electron microscope, illumination of the sample is achieved by electrons, instead of photons for an optical microscope. Scanning electron microscopy (SEM) and transmission electron microscopy (TEM) create images of the samples using electrons. With SEM an image is obtained from electrons being reflected or knocked off of the sample, this is in contrast to TEM where an image is created by detecting electrons that are passed through the material. For TEM much higher voltages are required to transmit the electrons through the material, this allows for a near-atomic resolution to be obtained.

The surface morphology of the samples was examined using an FEI Quanta FEG 650 field emission SEM and a Zeiss Supra 40. The use of electrons contains many advantages; a larger magnification can be obtained due to the smaller achievable wavelength of electrons (as seen by the De Broglie wavelength λ_e in **Equation 3-11**) along with a much higher depth of field.

$$\lambda_e = \frac{h}{m\nu} = \frac{h}{\sqrt{2m_o eV\left(1+\frac{eV}{2m_o}c^2\right)}} \approx \sqrt{\frac{1.5}{V}}\ (nm) \qquad 3\text{-}11$$

The terms *h*, *m* and ν denote Planck's constant, the relative electron mass and velocity. The terms m_0, *e*, c^2 and *V* denote the electron rest mass, electron charge, speed of light and applied voltage. Since the values of $e = 1.6 \times 10^{-19}$ C, $m_0 = 9.1 \times 10^{-31}$ kg and $h = 6.626 \times 10^{-34}$ J·s, further simplification of the equation can be achieved as seen in **Equation 3-11**. The applied voltage used for the SEM was 5-10 kV, thus obtaining a value of 17.3-12.2 nm for λ_e^{SEM}.

A simple schematic of an SEM can be seen in **Figure 3-12**. The electron gun creates a beam of electrons, which are then directed and focused by magnets (lenses) towards the surface of the sample. A detector is used to analyse any emitted electrons from the surface of the sample.

For TEM, thin cross-sectional samples were prepared by a standard in-situ lift-out technique using a focused ion beam system[171]. They were observed in a high-angle annular dark field (HAADF) scanning TEM (STEM) mode. HAADF images are created by collecting high-angle scattered electrons with an annular dark field detector. HAADF image contrast is linked to the atomic mass. A brighter contrast is obtained for the heavier elements[172]. TEM uses a broad, parallel beam, which is good at surveying a sample. In this work, the samples were analysed by a scanning TEM (STEM) which uses a focused beam which scans the sample line by line. The TEM was a Thermo Fisher Talos F200X G2 equipped with a field emission gun and operating at 200 kV thus resulting in 2.7 pm for λ_e^{TEM}. The system has four in-column Super-X energy dispersive X-ray spectrometer detectors having a total collection angle of ~0.9 sr. The TEM measurements and sample preparation were carried out at Queens University Belfast, United Kingdom.

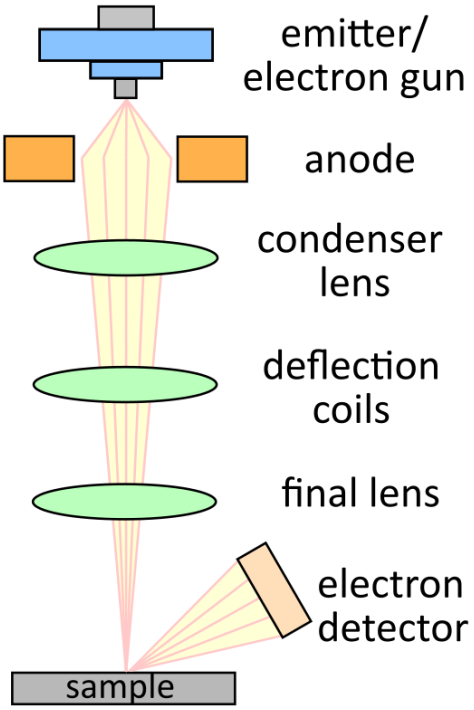

Figure 3-12. Scanning electron microscope layout and function.

3.3 Optical spectroscopy techniques

Spectroscopy is the study of the emission and absorption of light from a material as a function of optical wavelength. A simple schematic of our spectroscopic setup can be seen in **Figure 3-13**, where the sample is placed on the sample holder within a cryostat.

The temperature control system consisted of a closed cycled helium cryostat which allowed for room temperature (RT) and low temperature (LT), 12 K photoluminescence measurements.

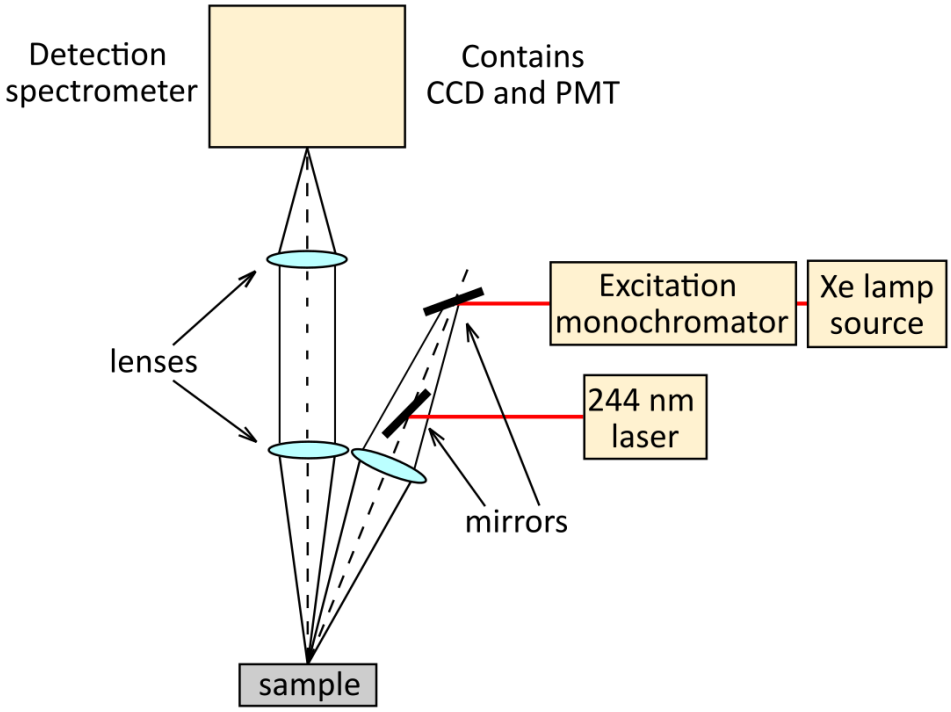

Figure 3-13. Schematic of spectroscopy setup used in this thesis.

A charge-coupled device (CCD) is an integrated circuit that contains small light-sensitive areas which are composed of an array of pixels that collect the incident photons and generate electrons. The generated electrons captured by the pixels are then amplified and converted to a voltage.

The excitation source (which usually contains a higher photon energy than that of the bandgap energy of the sample), can be either the 244 nm laser or the monochromatic emission from the xenon lamp. The light is then directed using a mirror and focused on the sample using a lens. The resulting emission is then passed through two lenses which direct and focus the light onto the spectrometer which has both a photomultiplier tube (PMT) and CCD available for detection.

3.3.1 Photoluminescence spectroscopy

Photoluminescence (PL) is the excitation of the sample at a fixed wavelength (photon energy higher than the material's band gap energy) where the emission wavelengths from the sample are measured. The emission spectra for our samples were obtained using a continuous-wave Ar^+ ion 244 nm laser as the excitation source.

A photoluminescence spectrum for 120 nm thick GaN at 12 K can be seen in **Figure 3-14** where the peak at 357 nm corresponds to the near band edge (NBE) emission and the peak at ~550 nm corresponds to defect emission in the material.

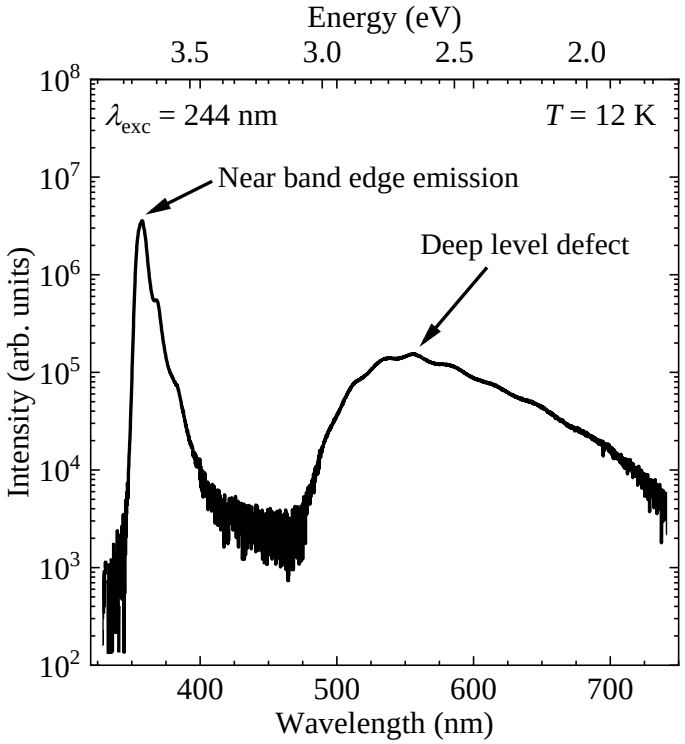

Figure 3-14. Photoluminescence spectrum for GaN thin layers at 12 K.

3.3.2 Photoluminescence Excitation spectroscopy

Photoluminescence Excitation (PLE) is a spectroscopic technique used to study the electronic structure of materials by measuring the absorption of light at different excitation wavelengths and detecting the subsequent emission of light[173].

With PLE, a wavelength tuneable source (Xenon lamp) is used to excite the sample where the energies can be varied from $> E_2$ to E_1 (as seen in **Figure 3-15**) and the resulting luminescence is collected via a spectrometer at a fixed detection wavelength (λ_0)[173].

One luminescence band or energy level can therefore be isolated and studied within the forbidden band gap region i.e. E_x. This is in contrast to PL which provides information about the ground state in the bandgap due to crystal impurities, PLE can access their excited states which provides information about the absorption and emission of electronic defects.

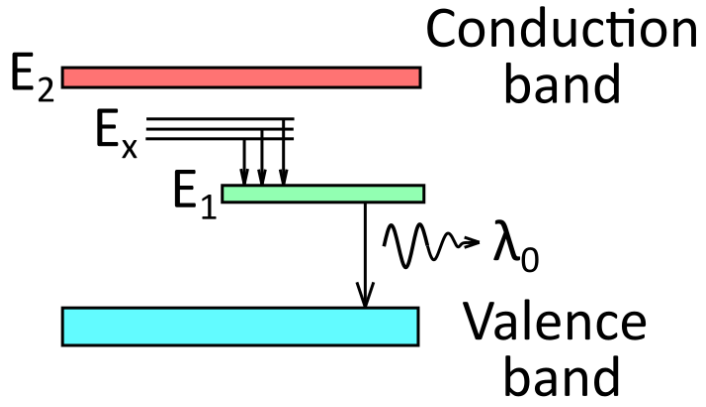

Figure 3-15. Energy gaps showing defects in the forbidden region.

By way of example, a PL and PLE spectrum for 120 nm thick GaN at 300 K can be seen in **Figure 3-16**.

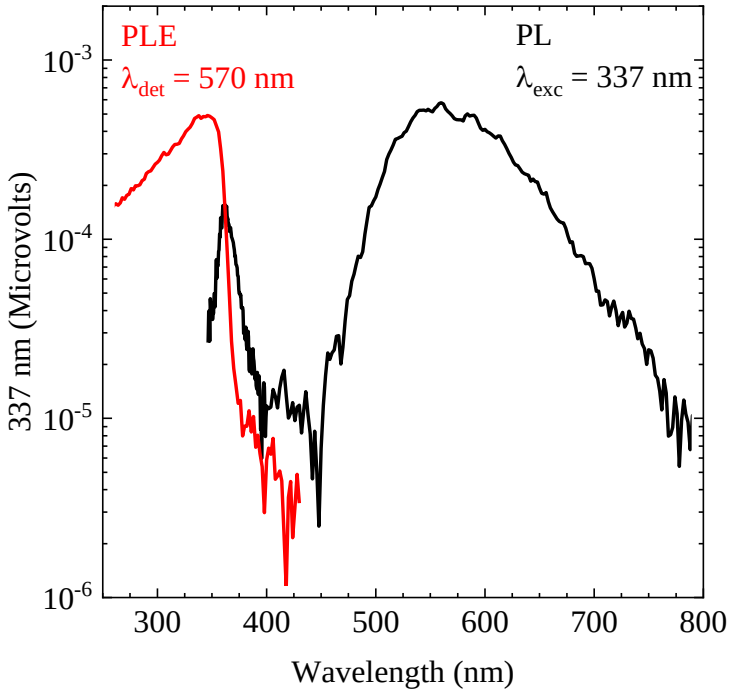

Figure 3-16. Room temperature photoluminescence and photoluminescence excitation spectra (using Xe lamp as the excitation source).

In this example, the excitation wavelength (λ_{exc}) of the sample was at 337 nm where the peaks at 360 and 570 nm are associated with the band edge and defect peak, respectively. For PLE a detection energy is chosen larger than the E_{gap}. Since a large intensity is observed for the defect peak at 570 nm, this is then chosen as the detection wavelength λ_{det} for PLE. The sample is then excited using the broad band xenon source and a λ_{det} of 570 nm was used. The peak at 344 nm corresponds to the bandedge[174].

4 GROWTH OF BGAN THIN LAYERS

In this chapter, an introduction is given into the experimental work that other groups have achieved with the growth of B containing III-Nitride materials. The growth and characterisation of 120 nm BGaN thin films were then conducted in our MOCVD reactor under various conditions.

4.1 Introduction

There have been various literature reports on the growth of BGaN layers with varying boron incorporation under a range of growth conditions. The maximum boron incorporation achieved by these groups along with the growth temperature and carrier gas can be seen in **Figure 4-1**.

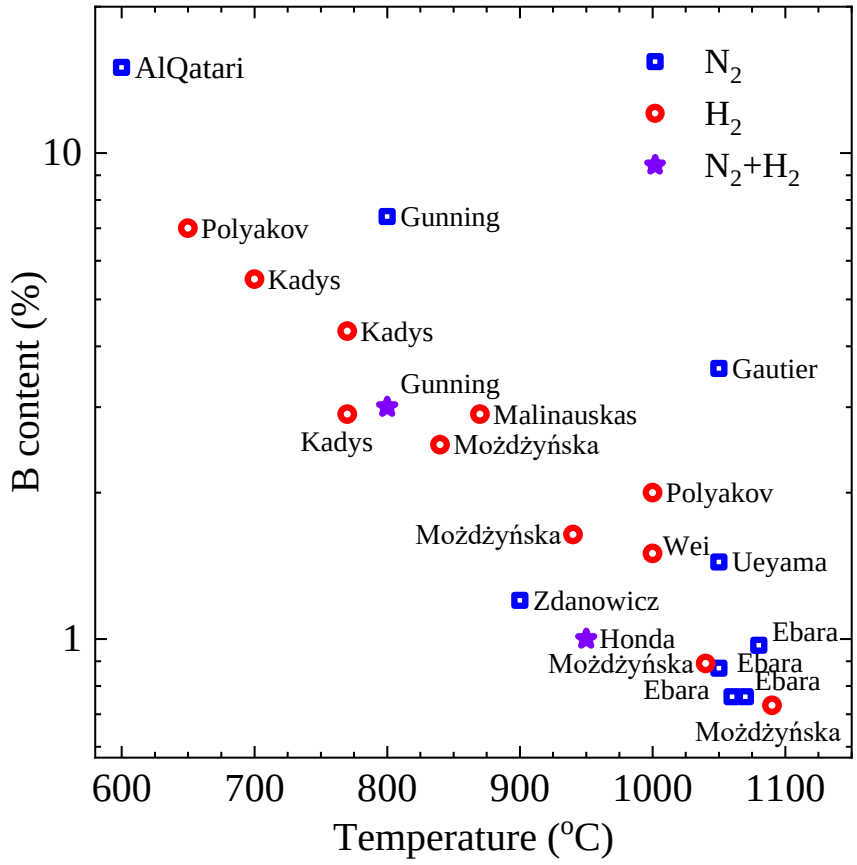

Figure 4-1. Boron content achieved in BGaN thin films versus growth temperature by MOCVD where templates used were carrier gases □N_2, ○H_2, ☆H_2+N_2[42,175–185].

AlQatari *et al.*[183] reported a maximum boron incorporation above 10% in thin layers of 200 nm (B)GaN using low growth temperature along with N_2 carrier gas. However, this thin layer contains a mixed-phase of BGaN which has been reported elsewhere in the literature[186,187], where both zincblende (ZB) and wurtzite (WZ) structures are observed.

The growth of the unwanted ZB phase along with the WZ phase appears to be quite a fundamental effect with the incorporation of BN. Altering the temperature was reported to have no effect in preventing the formation of the ZB phase[179,186]. Gautier *et al.*[186] showed that this ZB phase further impacts the material quality resulting in the presence of columnar growth and stacking faults in the BGaN layers. A large miscibility gap also exists with the incorporation of BN the threshold for which is reported to be around 2.8% and 3.7% at 1000°C for GaN and AlN respectively[188,189].

Different techniques have been implemented to try and increase the boron content while maintaining the structural and material quality. Ougazzaden *et al.*[190] showed that the use of BGaN/GaN superlattices allowed for a high boron incorporation while preventing plastic relaxation in the material and thus preventing cracking in the material. The use of flow-modulated epitaxy/ pulsed atomic flow epitaxy by various groups has allowed for the growth of BAlN thin layers above 7% while holding the single wurtzite phase[191,192]. Polyakova *et al.*[42] showed that an increase from 1-7% was achievable by ion implantation of B into BGaN thin layers however, an increase in the defect density of the layer was also observed. Ueyama *et al.*[182] showed that by increasing the offcut angle of sapphire from 0 to 2° towards the *a*-axis an improvement in root mean square surface (RMS) roughness was observed from 428 nm to 47 nm due to B incorporating at the step edges rather than the formation of nuclei on the terrace and then desorbing.

The potential advantages of BGaN have been shown by Akasaka *et al.*[193] The growth of BGaN micro islands as novel buffer regions uses this phase separation to reduce the number of threading dislocations propagating up through the material. Nong *et al.*[194] showed that the introduction of boron during the initial stages of MOCVD growth promoted a 3D growth pattern for an AlN buffer layer. This pattern resulted in a reduction in the tensile stress along with a crack-free 500 nm AlN thin film.

The two critical factors for high boron content, as shown in **Figure 4-1**, are N_2 carrier gas and low growth temperatures. This influenced the temperature range and carrier gas used in this study.

4.2 Experimental growth of BGaN thin layers

In this chapter, the growth of nominally 120 nm-thick layers of BGaN was initially studied under both compressive and tensile strain conditions to understand the growth mechanism and incorporation of boron in our MOCVD reactor. The main group-III precursors included TMAl, TMGa and TEB; and ammonia as a source of nitrogen. Nitrogen was used as the main carrier gas. The temperature was varied from 950°C to 850°C in increments of 50°C with a constant pressure of 100 mbar and gas phase B/III ratio of 1%. A 900°C GaN reference sample was also grown for comparison. The thin layers were grown on top of 2 µm GaN, or 800 nm AlN templates in each case. Both templates were prepared on a *c*-plane sapphire substrate, with a 25 nm AlN sputtered layer (Kyma Technologies). A simple schematic of the grown structure can be seen in **Figure 4-2**.

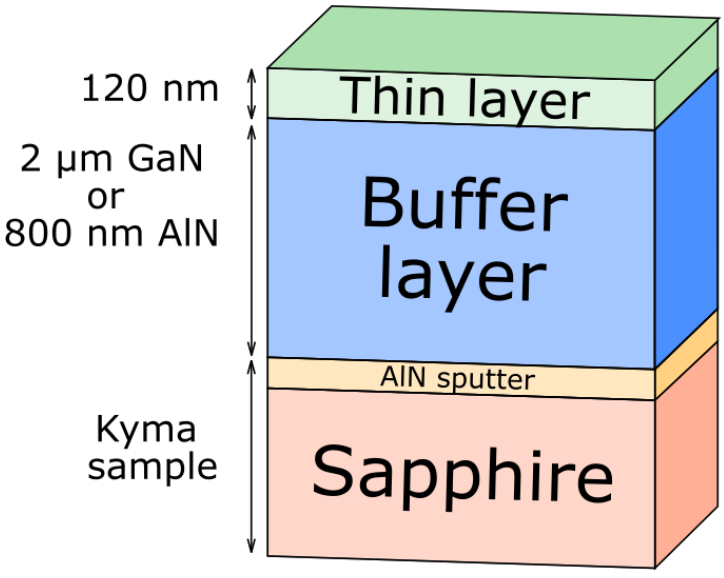

Figure 4-2. Simple schematic of 120 nm BGaN thin layer grown on AlN/ GaN templates.

XRD 002 and 101 scans can be used to determine the number of edge and screw dislocations in a sample, as previously discussed in **Section 1.3.7**. From the 002 and 101 FWHM XRD ω-scans for the 2 µm GaN buffer layer a value of 200 and 450

arcseconds was obtained, respectively. Literature values for the 002 and 101 are around 250-300 arcseconds and 300-350 arcseconds[195] which are similar to our results. This result suggests that the dominant dislocations present in the GaN template are screw dislocations which originate due to the low-temperature nucleation layer at the interface resulting in a highly faulted layer[196].

A value of 600 and 800 arcseconds was obtained for the 002 and 101 FWHM ω-scans for the 800 nm AlN buffer layer grown on AlN/Sapphire. The FWHM values obtained for the AlN template are different when compared to the literature values where a higher value is expected for the 101 than the 002 FWHM[197–200]. There are numerous methods to nucleate AlN on Sapphire[201–203], including ones that are designed to reduce the very large edge dislocation density, with a sacrifice in screw dislocation density as a result. Indeed our AlN template grown in our reactor was not optimised fully as the aim was primarily calibration, also it is a relatively thin material i.e. < 1um leading to the relatively large FWHM observed.

4.3 Analysis of BGaN thin layers grown on GaN template

4.3.1 Surface morphology of BGaN thin layers

Using SEM, a heavily v-pitted surface was observed for the 900°C GaN reference sample grown on the GaN template as seen in **Figure 4-3 (a)** and a cross-sectional image of the sample (as seen in **Figure 4-3 (b)**), indicates that the formation of these pits is at the buffer and thin layer interface, often referred to as pinned v-pits[204].

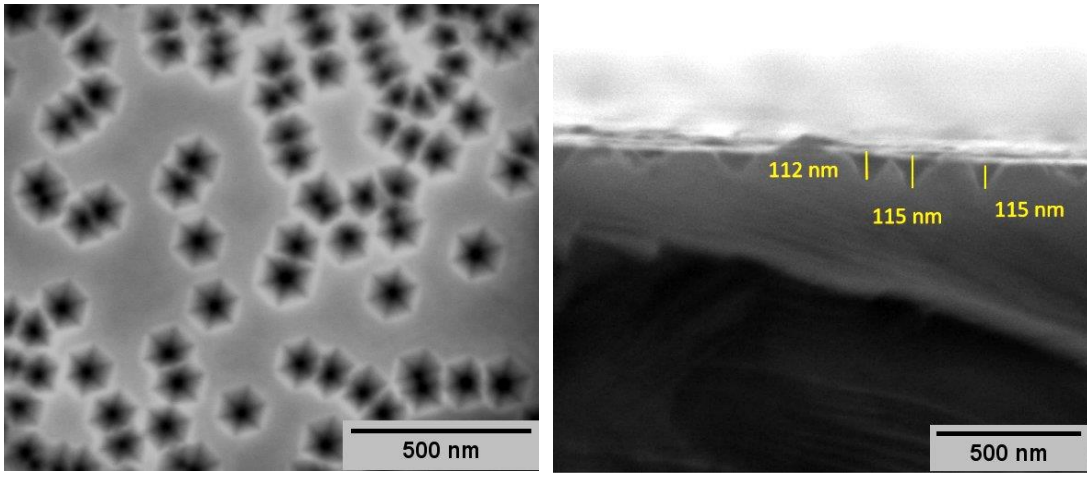

(a) (b)

Figure 4-3. GaN thin layer reference sample grown at 900°C (a) surface and (b) cross-sectional image using SEM.

This was further confirmed using the software package ImageJ[205], where the angle α between the *c*-plane and the slanted plane associated with the v-pits was calculated as ~62°. This indicates that these are pinned v-pits with $10\bar{1}1$ slanted planes[206]. This angle θ between the (001) and (101) plane can also be calculated using **Equation 4-1**[207].

$$Cos\theta = d_{h_1k_1l_1} d_{h_2k_2l_2} \left[\left(\frac{4}{3a^2} \right) \left\{ h_1h_2 + k_1k_2 + \frac{1}{2}(h_1k_2 + h_2k_1) \right\} + \frac{l_1l_2}{c^2} \right] \quad 4\text{-}1$$

The terms $d_{h_1k_1l_1}$ and $d_{h_2k_2l_2}$ denote the interplanar spacing for the planes (h_1, k_1l_1) and (h_2, k_2, l_2) respectively. The in-plane and out-of-plane lattice constants are denoted by a and c respectively. The formation of these v-pits is associated with threading dislocations propagating perpendicular to the *c*-plane through the buffer layer and forming v-pits at the interface. From the literature, a reduction in v-pit diameter is observed when increasing the growth temperature of GaN layer[204,208], higher growth temperature also allows for the improved cracking of NH_3 and as a result, improves the quality of the GaN layers.

The dislocation density of the GaN thin layer was also estimated using ImageJ[205] as seen in **Figure 4-4**, by dividing the number of pits by the image area.

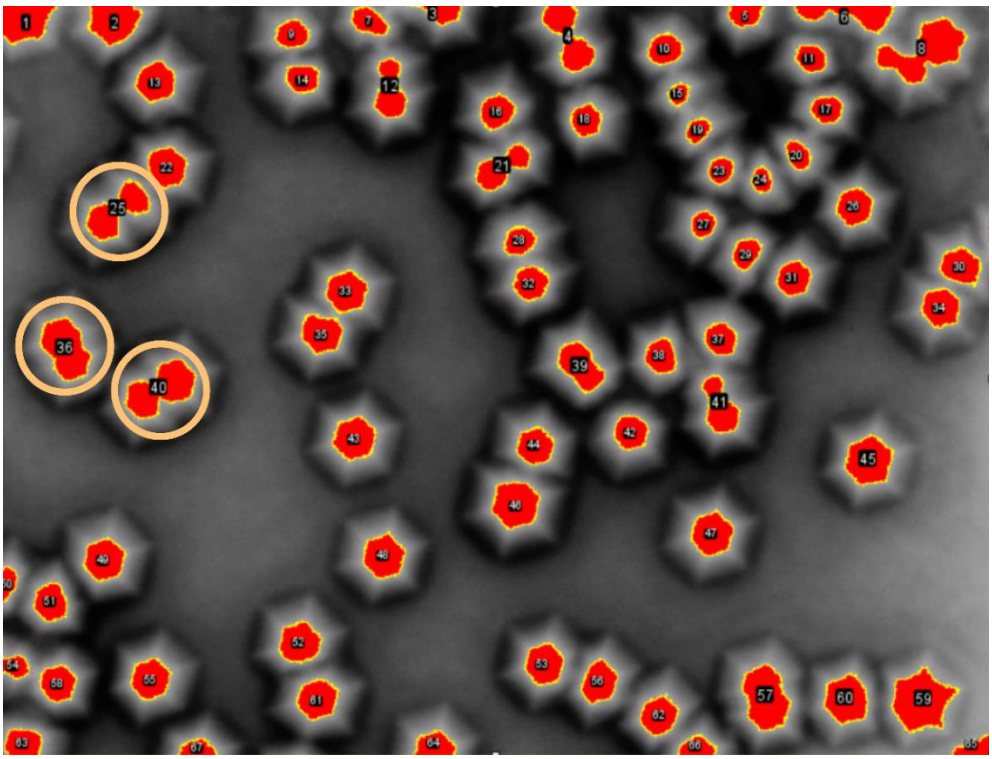

Figure 4-4. ImageJ software pit analysis of 120 nm GaN grown on GaN template.

However, with the software ImageJ the density of the pits is undercounted as seen by the "pits" numbered 25, 36, 40 etc. This results in an underestimation of the dislocation density which is further highlighted when compared to the estimate of the dislocation density of the buffer layer region using XRD 002 and 101 ω-scans (**Table 4-1**).

Table 4-1. Estimated threading dislocation density for 900°C GaN thin layer.

	Dislocation density (cm^{-2})
ImageJ	$4.32x10^{9}$
XRD	$5.8x10^{9}$

The incorporation of 1% TEB at 900°C results in the removal of these v-pits along with a disruption in the surface morphology as seen in **Figure 4-5 (c)**.

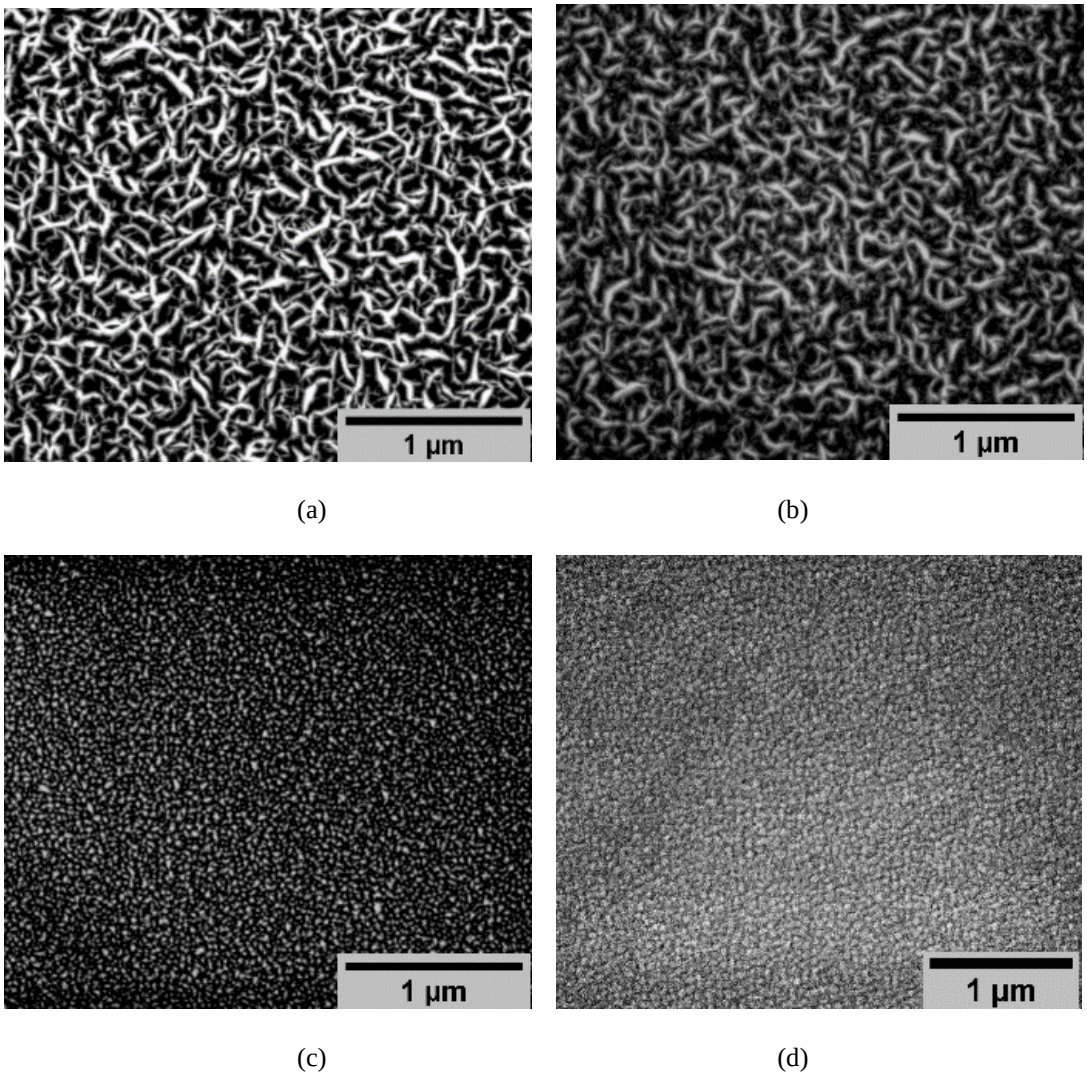

Figure 4-5. Surface morphology of BGaN samples grown at (a) 800°C, (b) 850°C, (c) 900°C and (d) 950°C on a GaN template.

This was similar to the BGaN samples grown at 950°C (as seen in **Figure 4-5 (d)**) where a speckled morphology along with higher surface roughness was observed.

The 800°C and 850°C BGaN samples as seen in **Figure 4-5 (a)** and **(b)** respectively appear to have lighter and darker regions. A 45° tilted view of the 850°C sample can be seen in **Figure 4-6**, which indicates that these darker regions are associated with areas of slower-growth rate.

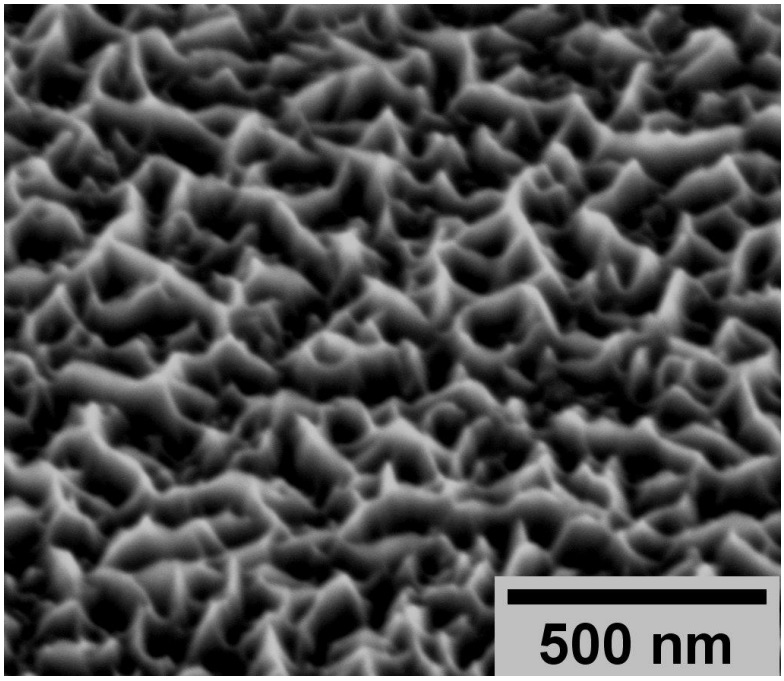

Figure 4-6. Cross-sectional image of 850°C BGaN thin layer sample.

These slower-growth regions are also similarly seen by Kadys *et al.*[177] which appears to be a result of using N_2 carrier gas. This is in contrast to an island-like growth observed with the use of H_2 carrier gas as seen by Możdżyńska *et al.*[180]

4.3.2 Strain analysis of BGaN thin layers

XRD results for the 002 ω-2θ scans can be seen in **Figure 4-7** where two main peaks are observed when BGaN was grown on top of the GaN template.

The 34.5° and 34.7° peaks correspond to the GaN and BGaN peaks, respectively. All temperature-varied samples with TEB introduced into the system, resulted in a shoulder appearing at higher angles indicating BN is occupying the sites in the GaN lattice and therefore forming BGaN. The lack of a distinct BGaN peak at 800°C indicates a smaller BN incorporation when compared to the other samples, which is possibly due to the non-optimal growth conditions for GaN. Lowering the growth temperature reduces the thermal cracking efficiency of ammonia[209] and also reduces the formation of the Ga--N bond which requires high energy[210].

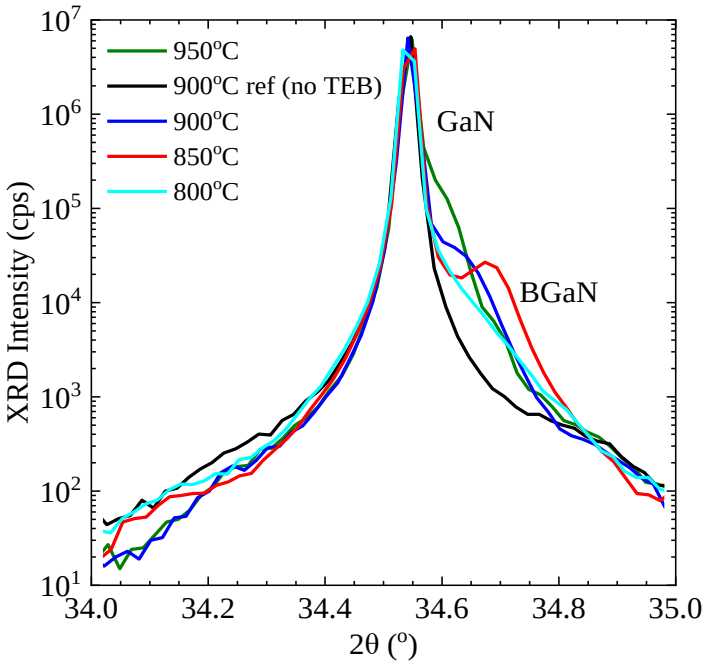

Figure 4-7. ω-2θ 002 scans for 120 nm thin layers of BGaN grown on a GaN template.

A distinct peak is present for BGaN grown at 850°C in 002 ω-2θ reflections and 105 RSM scans were measured to confirm the strain state of the thin layer as seen in **Figure 4-8(a)** when compared to the GaN reference sample as seen in **Figure 4-8(b)**.

The vertical and diagonal full red line represents the strained and relaxed line for BGaN on the GaN template. The diagonal red dashed line represents different B incorporations into the thin layers. The distinct shoulder at around (2775, 7452) indicates that the material grows fully strained with the incorporation of boron. A boron incorporation of 1.3±0.7% was estimated for this fully strained 850°C BGaN sample. The error was calculated using the formula for one standard deviation i.e. $\sigma = \frac{FWHM}{2\sqrt{2\ln 2}}$ which was confirmed using the algorithm described by Schuster *et al.*[211]. A linear interpolation of the values in **Table 3-4** and ω-2θ scans in the 101 and 002 planes were used for this calculation.

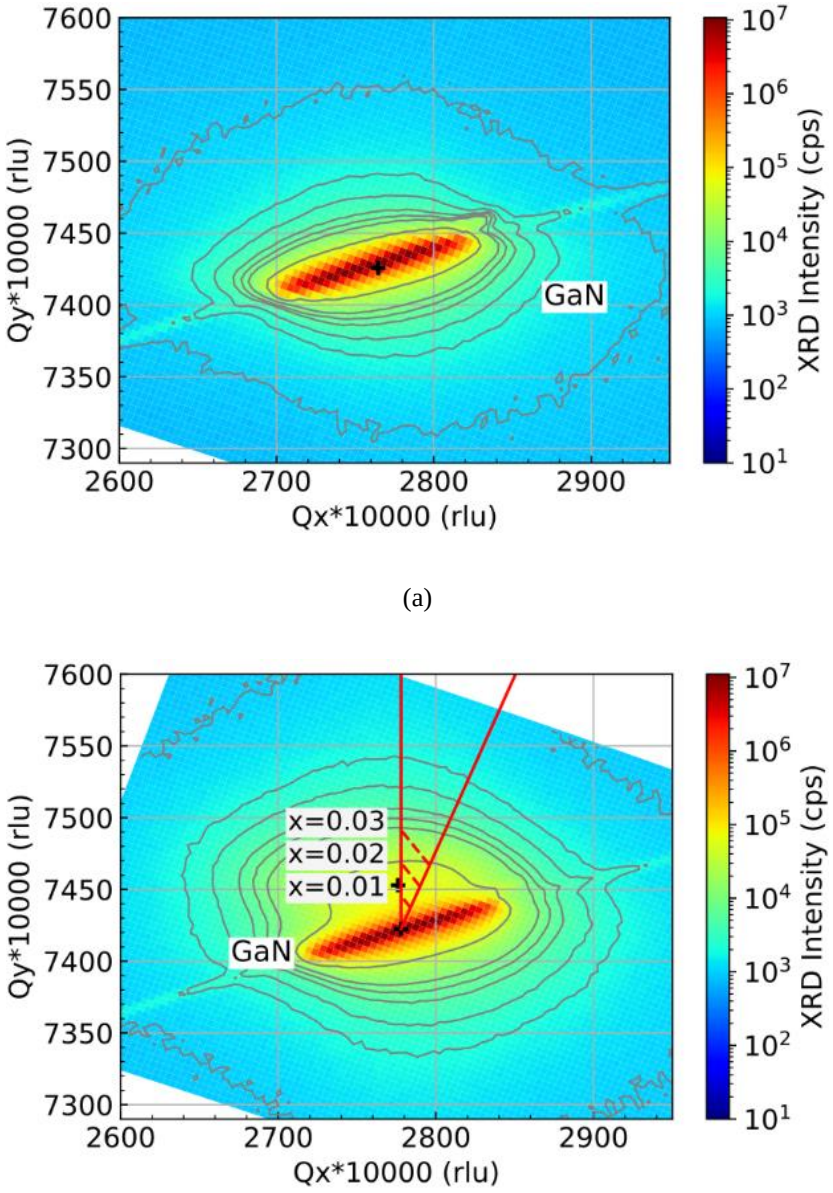

Figure 4-8. 105 Reciprocal space map scans for (a) 900°C GaN and (b) 850°C BGaN sample on a GaN template.

4.3.3 Strain analysis of BGaN samples

XRD 002 symmetric ω-2θ scans for the BGaN thin layer grown under compressive strain on the AlN template can be seen in **Figure 4-9**. This initial growth under strain can be seen as an asymmetric peak/ tail in the region 34.0° to 34.4° for the reference sample before it is allowed to relax. When the BGaN thin layers are grown on the AlN template a shift of the main peak to higher angles, towards the AlN peak is observed.

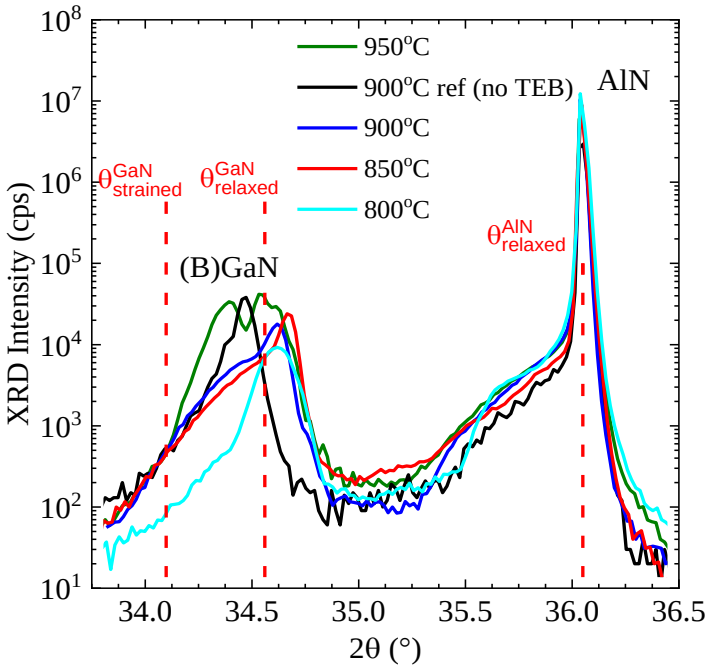

Figure 4-9. ω-2θ 002 scans for thin layers of BGaN on an AlN template.

Two peaks are observed for the 900°C GaN reference sample at 34.5° and 36.04°, corresponding to the GaN and AlN peaks, respectively. With the addition of BN, the main peak shifts to higher angles leaving a broad shoulder in the original position (34.0° to 34.4° region) except for the sample grown at 950°C for which two resolved peaks are observed. One peak coincides with the theoretically relaxed GaN line ($\theta_{relaxed}^{GaN}$), however the other peak shifts to a lower angle towards the theoretically strained GaN line $\left(\theta_{strained}^{GaN}\right)$. Similarly, to BGaN grown on a GaN template as seen in **Figure 4-7**, the 850°C sample contains the largest shift to higher angles.

To understand the sample structure more clearly skew-symmetric 101 reflections were measured as seen in **Figure 4-10**.

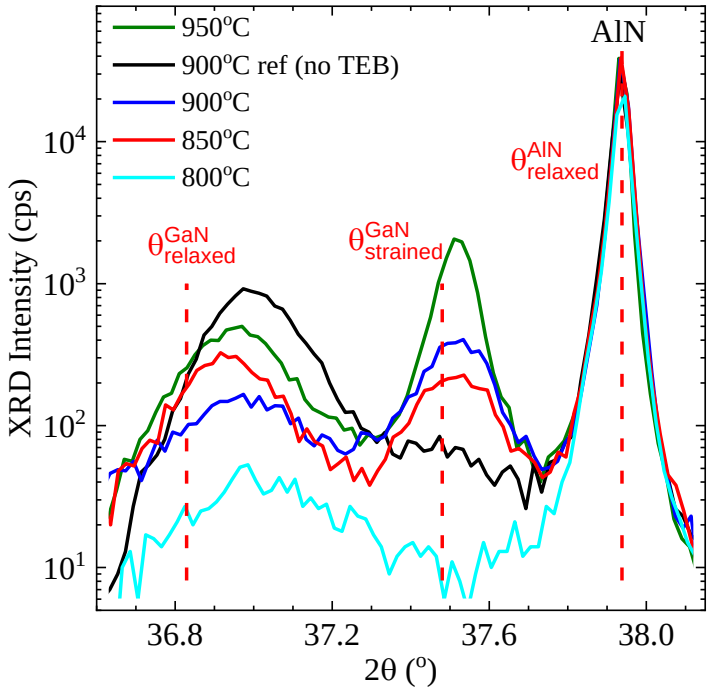

Figure 4-10. ω-2θ 101 reflections for BGaN thin layers on an AlN template.

Three distinct peaks at around 37°, 37.5° and 37.9° are seen for all BN-containing samples. While the lower angle peaks (~37°) for these samples almost coincide with the GaN peak for our reference (no boron) sample and the highest angle peak (37.9°) corresponds to the AlN template, the peaks in between them (~37.5°) must be associated with BGaN. For the 850°C BGaN sample, the formula from Schuster *et al.*[211] was used with the peak values obtained from the 101 and 002 reflections. A boron incorporation of ~0.01 and 0.05 was obtained for the peaks 36.93° and 37.51° respectively.

105 RSM scans were measured to try and help understand this double peak behaviour. This can be seen in **Figure 4-11 (a)** and **Figure 4-11 (b)** which corresponds to the GaN reference sample and 850°C BGaN sample respectively.

Similarly, the vertical and diagonal full red line represents the strained and relaxed line for (B)GaN on the AlN template. The diagonal red dashed line represents different B incorporations into the thin layers. For the GaN reference sample (as seen above in **Figure 4-11 (a)**), a single peak of ~74% relaxation was obtained which is similarly seen for the 101 reflections. This is in contrast to the 850°C BGaN reference sample

(**Figure 4-11 (b)**), where a single peak is obtained with a 95% relaxation along with 1.4% boron incorporation. However, a shoulder is also present with the sample at around (2864, 7380), which indicates that the incorporation of B forces the material to initially grow strained to the AlN buffer before allowing it to almost completely relax.

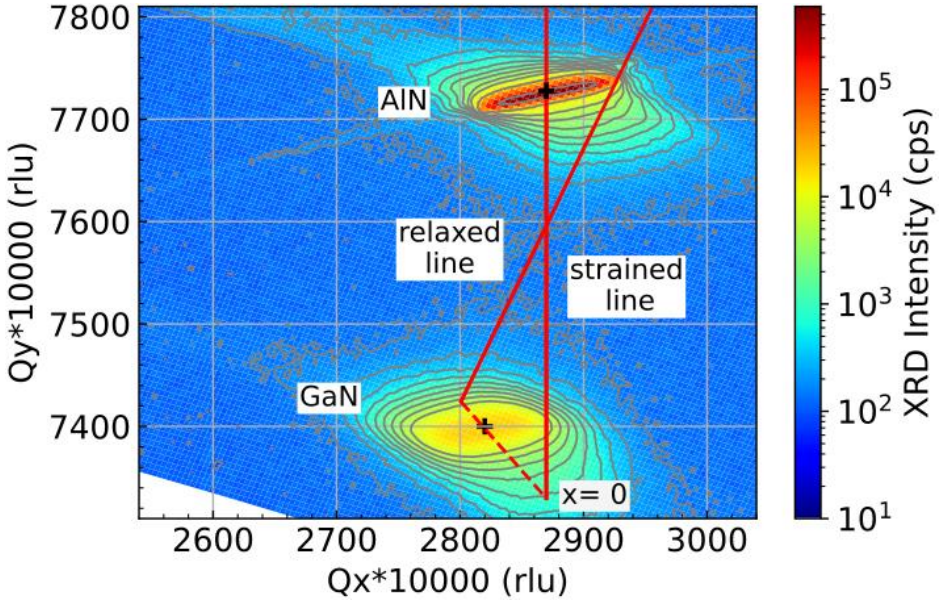

(a)

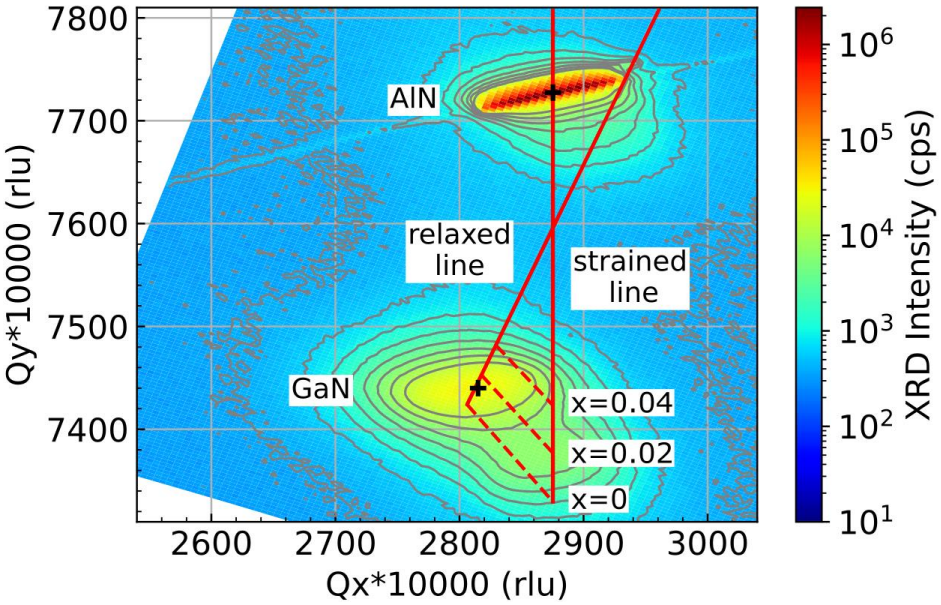

(b)

Figure 4-11. 105 Reciprocal space map scans for (a) 900°C GaN and (b) 850°C BGaN sample on an AlN template.

Moreover, double peak behaviour evident from the 101 scans and a difference in concentration to the 105 reflections for the samples, suggests a phase separation in the BGaN/ AlN samples which could also explain the shoulder appearing at lower angles in the 002 ω-2θ scans as previously mentioned. To get a better understanding of the phase separation a plane was chosen for the ω-2θ XRD measurement so that the GaN fully strained and relaxed almost overlapped as seen in the work of Wallis *et al.*[212,213]. The 102 plane was chosen (as seen in **Figure 4-12**), with an angular separation of 0.26° between $\theta_{relaxed}^{GaN}$ and $\theta_{strained}^{GaN}$.

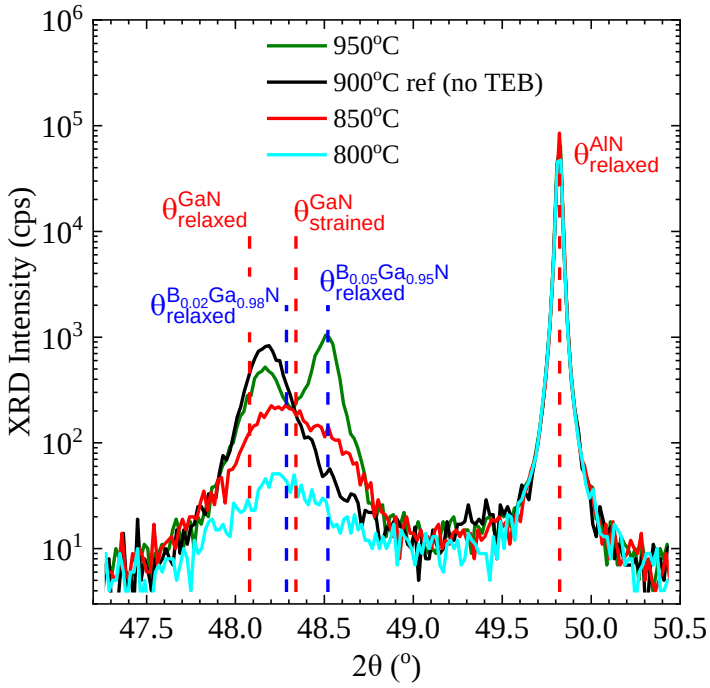

Figure 4-12. ω-2θ 102 reflections for thin layers of BGaN on an AlN template.

For the GaN reference sample, the peaks at 48.17° and 49.82° correspond to the GaN and AlN peaks respectively. With the incorporation of boron, a slight shift is observed in the main 48.17° peak to higher angles, along with an observed shoulder at 48.5° which becomes a distinct peak at 950°C. Again, it is believed that this peak is associated with phase separation that is present in all the boron-containing samples and increases with temperature.

Using the reflections from the (002), (101) and (102) planes the relaxation and BN incorporation for the BGaN thin layers were calculated as seen in **Figure 4-13 (a), (b)** respectively.

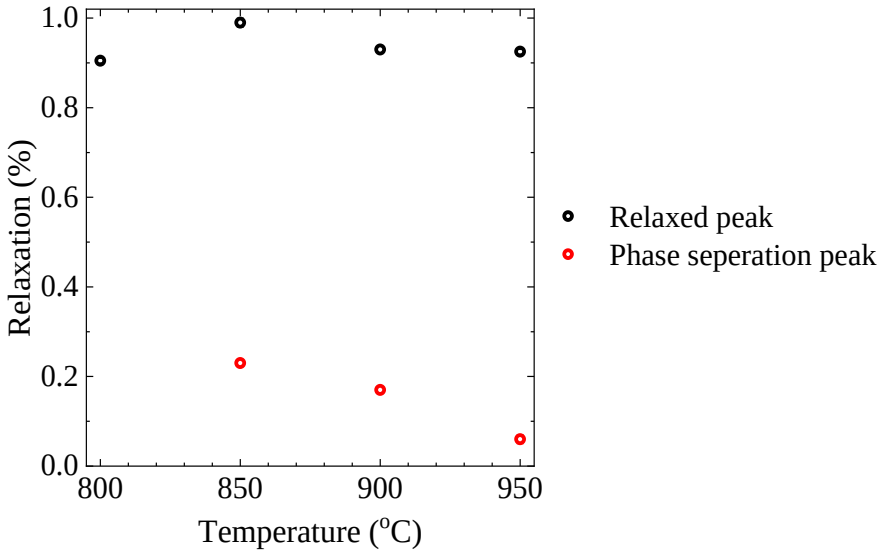

(a)

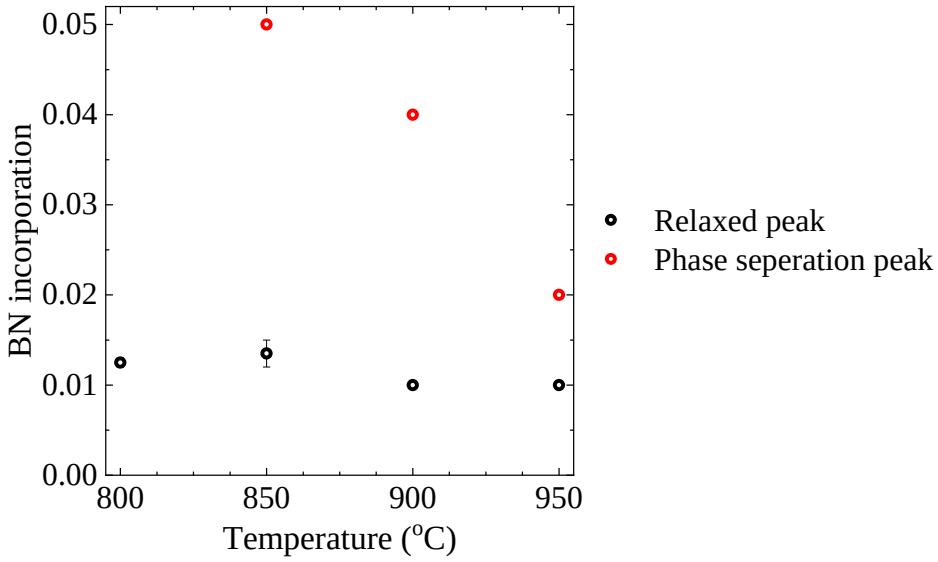

(b)

Figure 4-13. (a) Relaxation and (b) BN incorporation for $B_xGa_{1-x}N$ thin layers on an AlN template using 002, 101 and 102 XRD reflections.

From the results above, a maximum BN incorporation of 5% was obtained in the BGaN thin layers grown at 850°C. However, this is at the cost of what we believe to

be a phase separation occurring. As the temperature increases the BN incorporation into the "Phase separation peak" (denoted by red circles) appears to reduce along with a reduction in the strain in the material. The non-existence of a phase separation peak for the 800°C sample, as previously mentioned could be due to the non-ideal growth temperature of GaN. A similar behaviour is observed for the "Relaxed peak", the incorporation of small amounts of boron appears to reduce the relaxation in the material. To prevent this phase separation higher temperatures, appear to be more favourable, however at the cost of a lower BN incorporation in the "relaxed peak".

4.3.4 Conclusion

To conclude, an increase in strain was observed with the incorporation of BN as seen by the 101 and 102 ω-2θ and 105 RSM scans. At higher temperatures, phase separation occurs when BGaN is grown under compressive strain resulting in highly strained and relaxed regions within the BGaN thin layers. A method is proposed for distinguishing the clustering of boron atoms in the BGaN thin layers by choosing a plane where the relaxed and strained lines of GaN contain a small separation.

The maximum amount of boron clustering occurs when BGaN is grown at a temperature of 850°C on an AlN template. The incorporation of BN into thinner layers, such as quantum wells or barriers could be a more promising approach to reduce the amount of spinodal decomposition.

5 B(AL)GAN TERNARY AND QUATERNARY MQW STACK

Research into B-III-Nitride materials has increased in recent years, with the main focus so far being on thick layers as mentioned previously in **Chapter 4**. In contrast, there has been limited report on B containing quantum well heterostructures[214,215]. In this work, we try to advance this area from an experimental perspective by alloying boron with GaN to create the first ternary MQW BGaN/AlGaN stacks grown on *c*-plane AlN/sapphire templates for UV emission.

5.1 Experimental growth of BGaN MQW structure

The MQW structures were grown on a slightly Si-doped (< $5x10^{17}$ cm^{-3}) $Al_{0.2}Ga_{0.8}N$ buffer layer of 1.5 μm thickness, prepared on a *c*-plane AlN/sapphire (Kyma Technologies) substrate with a 200 nm AlN connecting layer. Disilane was used as the n-dopant precursor. For this initial study with low BN incorporation expected, the standard GaN growth conditions were used for the growth temperature of the MQW stack.

The complete structure was grown under both hydrogen and nitrogen carrier gas with a reactor pressure of 100 mbar, at a growth temperature of 1060°C, measured using optical pyrometry of the wafer pocket. The MQW structure consisted of five nominal 2.5 nm QWs of (B)GaN with a 10 nm $Al_{0.15}Ga_{0.85}N$ QB. The gas phase B/III ratios used were 0.3%, 1% and 3%, in addition to a B-free reference sample, grown for comparison. It should be noted that the solid composition is not expected to be the same as the gas phase ratio. A simple schematic of the grown structure can be seen in **Figure 5-1**.

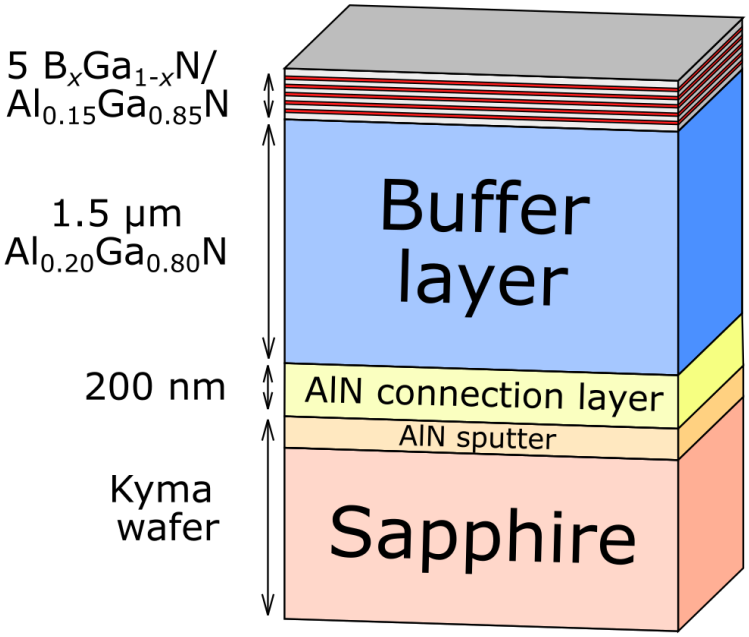

Figure 5-1. Schematic of $B_xGa_{1-x}N$/ $Al_{0.15}Ga_{0.85}N$ ternary MQW stack grown by MOCVD

5.1.1 Discussion of GaN/ AlGaN reference samples

XRD results are presented in **Figure 5-2** for the GaN QW reference samples grown under H_2 and N_2 carrier gas.

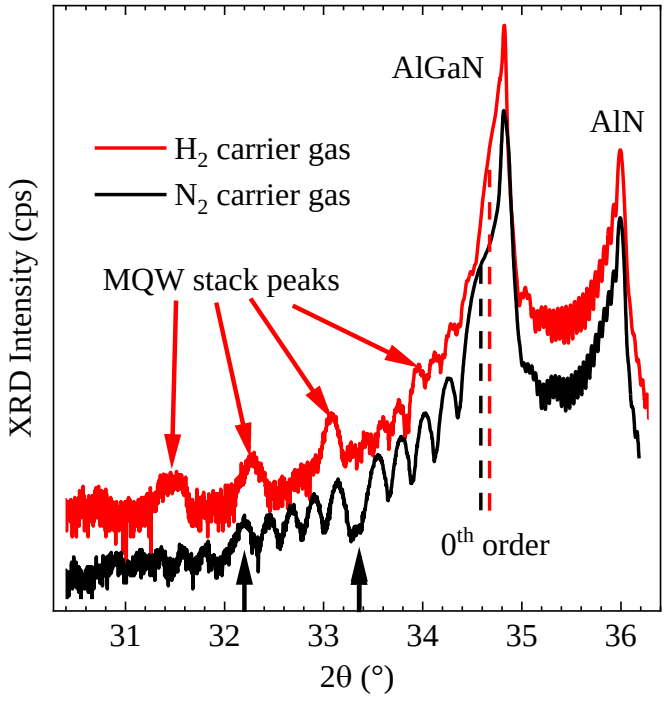

Figure 5-2. ω-2θ (0002) scan for GaN/ AlGaN MQW grown with N_2 and H_2 carrier gas

Both reference samples contain rather sharp and smooth QW/QB interfaces within the MQW stack. An improvement in the 0002 ω-2θ scans indicates that an enhancement in the Al adatom mobility occurs when replacing the carrier gas from H_2 to N_2[216], resulting in a smoother interface between the QW and QB interface as seen in **Figure 5-2**. This may be due to the higher density of the N_2 atom (14 times heavier[216]) than that of the H_2, improving the surface mobility of the Al adatoms. Further to this, a shift in the zeroth order peak to lower angles for growth with N_2 carrier gas when compared to H_2 indicates a lower Al incorporation into the MQW barriers.

Growth of the structure under H_2 resulted in a smaller separation of the MQW interference fringes than that of N_2 indicating a thicker QW+QB thickness[166]. This is due to the lower thermal conductivity of N_2 and a smaller diffusion coefficient which results in a delay in the decomposition of the metal organics and a lower growth rate[216]. By using the software package X'Pert Epitaxy provided by PANalytical, a sum of the QW and QB thicknesses (QW stack period) of 11.4 nm and 7 nm were obtained for the GaN/AlGaN samples grown under H_2 and N_2 respectively. The growth under H_2 was similar to the expected values of 12.5 nm, however, the N_2 was much thinner. This is due to standard AlGaN being grown under H_2 carrier gas.

Table 5-1. Results obtained from X'Pert Epitaxy

	N_2 carrier gas	**H_2 carrier gas**
QW+QB thickness	7 nm	11.4 nm
QW+QB Al content	12%	14.8%
Buffer layer Al content	18%	19%

A missing order peak also exists for the reference sample grown under nitrogen at the 1st order fringe which might indicate a similar thickness for the QWs and QBs[217,218]. Further to this, similar intensity was observed for both the satellite peaks and MQW

stack peaks indicating a reduced compositional contrast between QW and QB i.e. low Al incorporation in the QB[166].

A reduction in QW and QB thickness can also be seen from in-situ reflectance data in **Figure 5-3**. Vertical axes of the samples are mutually tuned so that the amplitudes of reflectance oscillations in the buffer coincide for both samples. From this representation, it is clear that the QW thicknesses are similar, but barriers for the H_2 sample are proportionally thicker compared to the N_2 sample as XRD analysis also suggests.

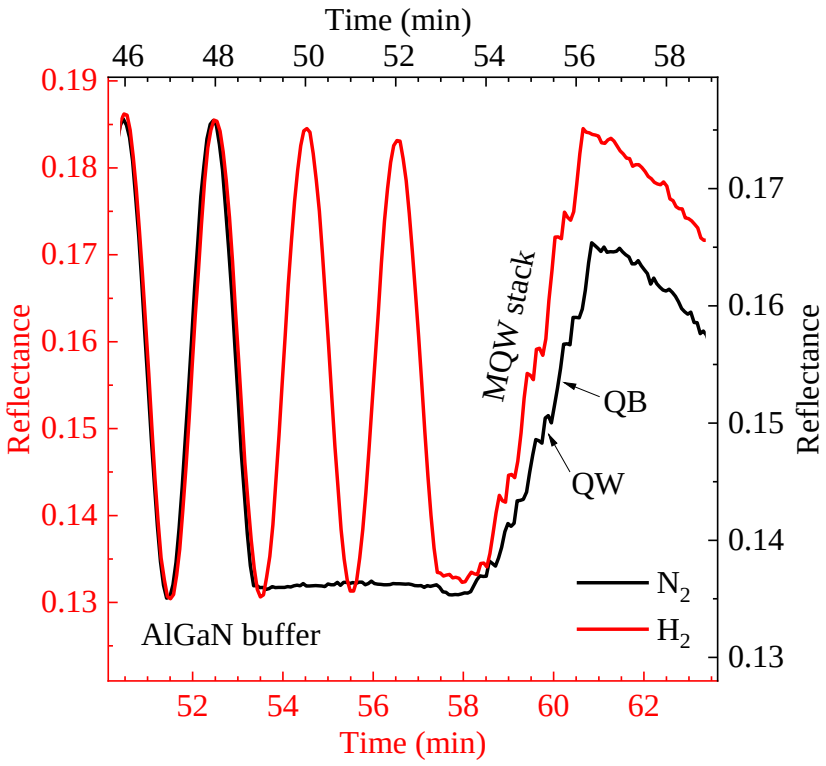

Figure 5-3. In-situ 650 nm LayTec reflectance for GaN/ AlGaN MQW grown with N_2 and H_2 carrier gas

An improvement in the surface morphology was also observed in SEM for the reference samples grown under N_2 compared to growth under H_2 carrier gas as seen in **Figure 5-4 (a)** and **(b)**.

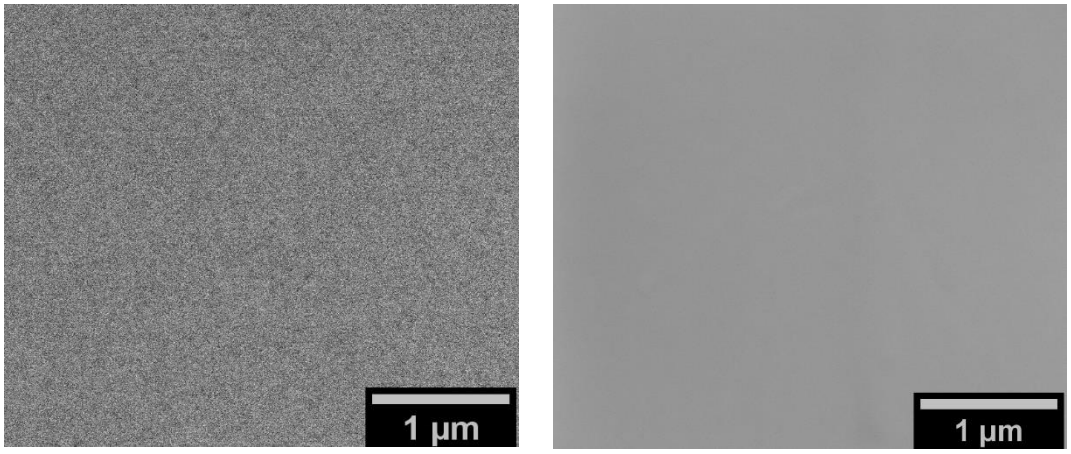

(a) (b)

Figure 5-4. SEM surface morphology for TEB/III = 0% samples grown with carrier gas (a) H_2 and (b) N_2

5.1.2 Discussion of BGaN/ AlGaN MQW samples

XRD results are presented in **Figure 5-5 (a),(b)** for the (B)GaN samples grown under H_2 and N_2 carrier gas, respectively.

For the <1% and 1% TEB/III samples, little impact was observed on the symmetric 002 ω-2θ scans in both cases. This was not the case for the highest TEB/III ratio of 3%, where the XRD features diminish significantly, and from this, we can conclude that some disruption to the periodic structure of the MQW stack has occurred with the introduction of B. This disruption of the QW+QB interface does not seem to be as severe when the samples are grown under N_2 carrier gas. Further to this, a shift to higher angles in the ω-2θ scans can be seen for the N_2 carrier gas samples with a TEB/III>1%. This shift to higher angles is consistent with the incorporation of BN which contains a smaller *c*-lattice parameter of 4.189 Å [29] when compared to that of GaN 5.185 Å[30].

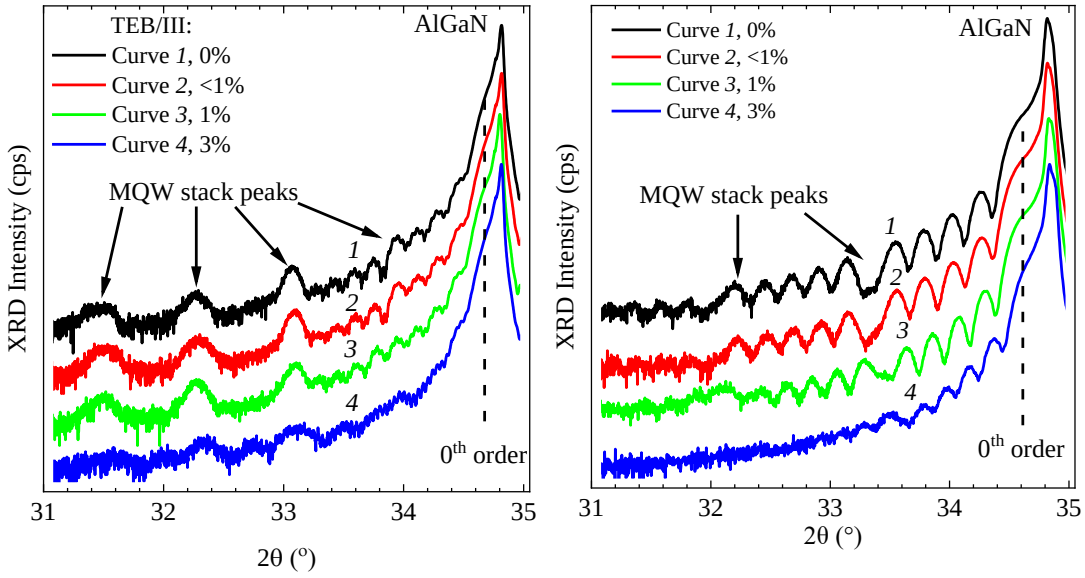

Figure 5-5. XRD ω-2θ (0002) scan for (B)GaN/AlGaN MQW grown at 1060°C with (a) H_2 and (b) N_2 carrier gas

Using SEM a smooth surface was obtained for both reference samples as previously seen in **Figure 5-4**. The incorporation of BN resulted in multiple pits forming on the surface of our samples as seen in **Figure 5-6 (a),(b)**.

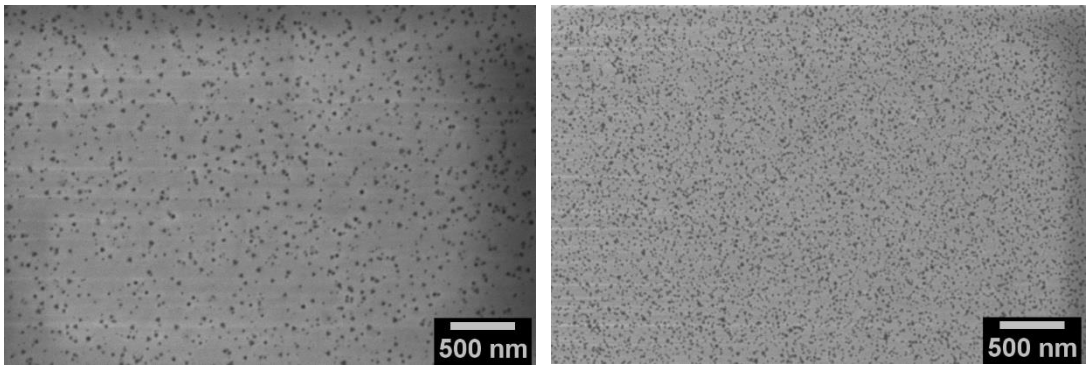

Figure 5-6. SEM surface morphology for TEB/III = 1% samples with carrier gas (a) H_2 and (b) N_2

Growth under H_2 resulted in an increase in diameter but a lower density of pits when compared to growth under N_2 carrier gas, suggesting a modification in the mechanism

with carrier gas. One possibility is that the N_2 carrier gas lowers the mean free path of the B atoms and thus limits the clustering size, as the B atoms are not able to find one another. A similar SEM surface morphology to the "1%" sample was observed for the "<1%" sample showing that even small flows of TEB have a significant impact on the growth. In the case of the TEB/III 3% sample, no pits were visible on the surface for both carrier gases however, a general increase in surface roughness was observed, as seen in **Figure 5-7**.

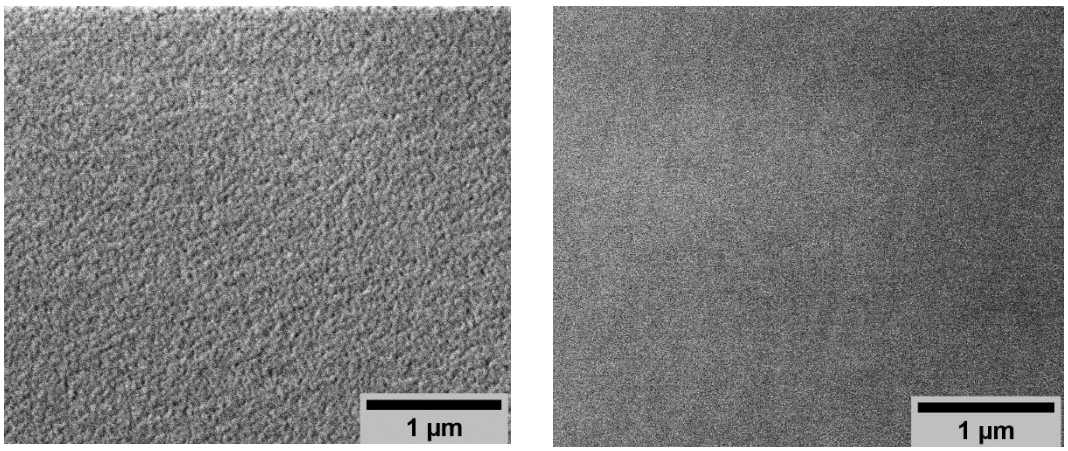

(a) (b)

Figure 5-7. SEM surface morphology for TEB/III = 3% samples with carrier gas (a) H_2 and (b) N_2

The room temperature (RT) PL emission spectra show a blueshift in the reference samples for the growth with H_2 compared to N_2 carrier gas as seen in **Figure 5-8 (a),(b)** respectively. This could be due to stronger quantum confinement due to a higher Al content (14.8% for H_2 compared to 12% for N_2 carrier gases, as estimated from the modelling of XRD scans as seen in **Table 5-1**). Another possible mechanism involves smearing the QW and QB interface, resulting in some of the Al atoms incorporating into the nominally GaN QWs[219]. This mechanism seems to be less severe in the case of growth under N_2 ambient conditions as seen from the sharper MQW interface features in the corresponding XRD scan (black curve in **Figure 5-5**).

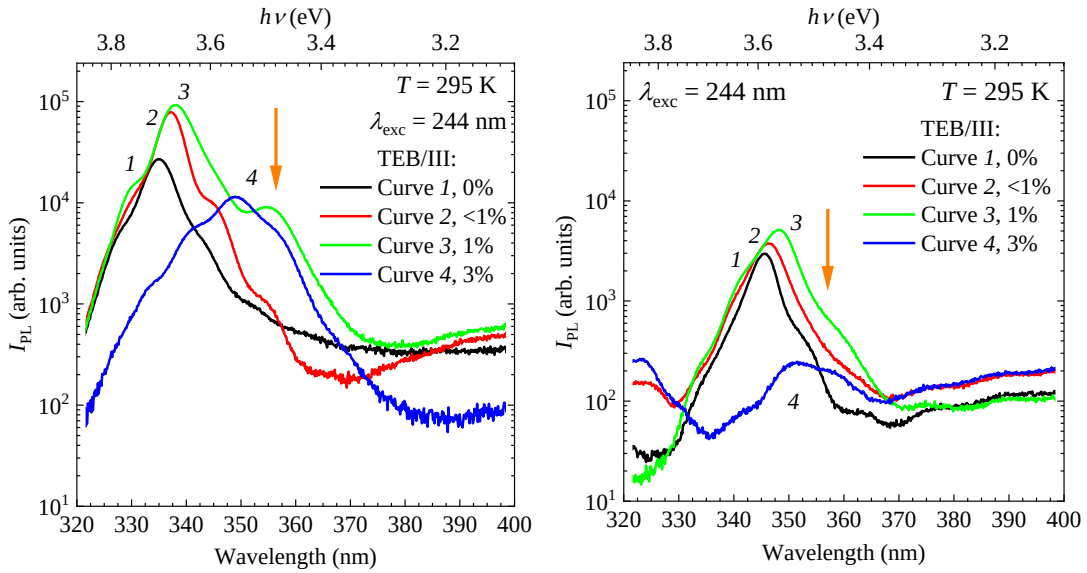

Figure 5-8. Room temperature photoluminescence spectrum for the BGaN MQW with (a) H_2 (b) N_2 carrier gas

In all the samples (as seen in **Figure 5-8 (a),(b)**), a redshift is observed with the incorporation of BN along with an increase in the intensity. For the samples grown with H_2 carrier gas (**Figure 5-8 (a)**), a slight shoulder is observed for the "<1%" sample at higher energies and for the "1%" sample, this becomes a distinct peak at ~3.5 eV (denoted by an orange arrow in **Figure 5-8 (a)**). This is similarly seen in the N_2 case as a slight shoulder (denoted by the orange arrow in **Figure 5-8 (b)**). The reduction in the intensity for the TEB/III 3% is possibly due to the disruption in the QW+QB interfaces as previously seen by XRD in **Figure 5-5**.

We believe that the broad peaks at 3.5 eV (~354 nm) in **Figure 5-8 (a)**, are associated with B localised centres, which result in the formation of localised states. We believe that the localised centres may be a result of isoelectronic impurities which introduce a trapping potential in our binary material. Isoelectronic traps[220] were reported to occur in II-VI materials resulting in a hole or electron being bounded depending on whether the impurity has a lower or higher electronegativity than the host atom respectively[221,222]. In our case, B contains a lower electronegativity than the host atom, resulting in a hole being the directly bounded carrier and an electron being bounded to

form a localized exciton. For small incorporations of BN, the bound exciton localizes at a single B site. When the concentration of B increases clusters of BN form which results in deeper energy levels forming. This is further highlighted by the multiple peaks observed with the "3%" samples in **Figure 5-8 (a)**.

The low temperature (LT) PL for the BGaN/ AlGaN MQW stack grown under (a) H_2 and (b) N_2 carrier gas can be seen in **Figure 5-9 (a),(b)** respectively. In the LT PL, a series of phonon replicas can be seen for both reference samples on the low energy side of the main peak which agrees well with the LO phonon energy associated with GaN (91 meV)[223].

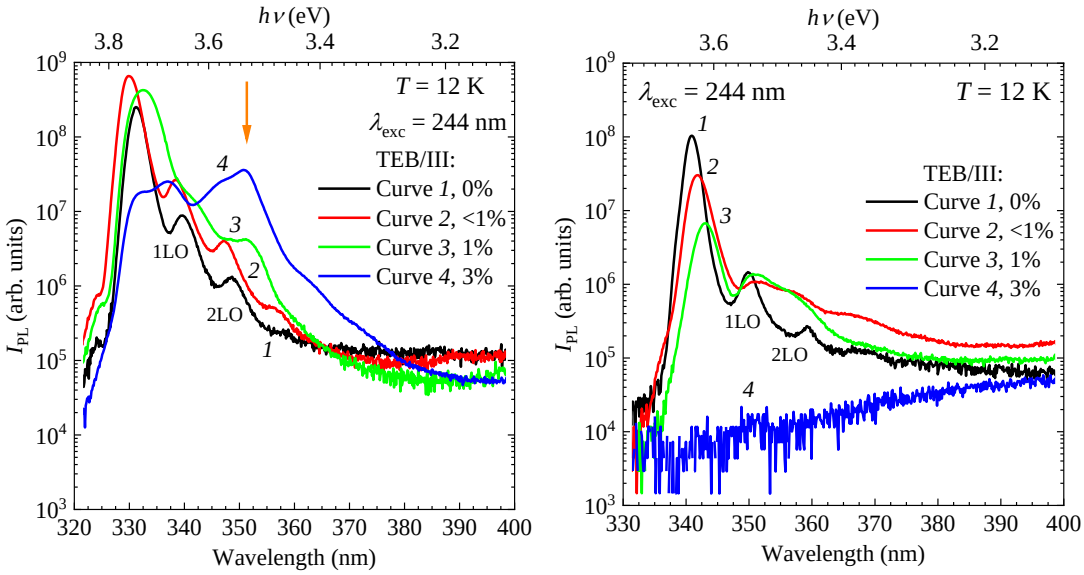

Figure 5-9. Low temperature photoluminescence spectrum for the BGaN MQW with (a) H_2 (b) N_2 carrier gas

Similarly to the RT PL, the incorporation of B appears to result in a redshift in the LT PL emission spectrum. However, an initial blueshift at LT was observed for the "<1%" sample grown under H_2 carrier gas in **Figure 5-9 (a)**) followed by the redshift (in the 1% sample). One possibility is that the incorporation of small amounts of BN could be slightly reducing the overall QCSE (previously mentioned and calculated in **Chapter 2**) and this could also explain the slight increase in intensity due to an

improvement in wavefunction overlap. At LT for the samples grown under H_2 carrier gas, a distinct peak is present for the 1% and 3% TEB/III samples. We believe that the peak at 3.54 eV is associated with the localised B centres. However, this peak is not as apparent for the BGaN samples grown under N_2.

5.1.3 Growth and characterisation of 960°C BGaN MQW

A reduction in the growth temperature to 960°C and a carrier gas of N_2 (due to a smaller pit dimension on the sample surface as seen in **Figure 5-6 (b)**) was used to try and prevent the nanomasking effect from occurring. As seen in **Figure 5-10**, a significant increase in surface roughness was observed by lowering the growth temperature of the MQW stack along with an increase in the pit density.

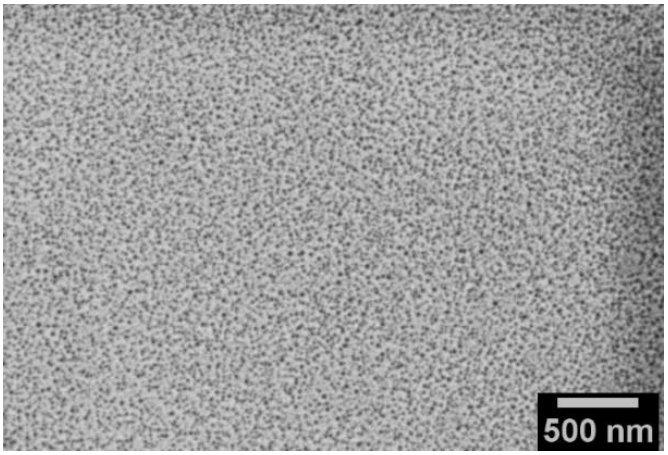

Figure 5-10. SEM surface morphology for 960°C N_2 samples with TEB/III = 1%

This increase in pit density was possibly caused by the higher BN incorporation at lower growth temperatures[179,180]. An increase in surface roughness was possibly due to the non-optimal growth parameters for the AlGaN QBs which was similarly seen on the surface for the 960°C reference sample.

The corresponding XRD and LT PL results are presented in **Figure 5-11 (a)**,**(b)** respectively. A shift in the reference sample's zeroth order peak to a lower angle indicates a lower AlN incorporation into the MQW stack when compared to the samples grown under 1060°C (as expected at lower growth temperatures[224]).

A reduction in the separation between the interference fringes indicates an overall reduction in the MQW stack thickness. A more severe disruption in the MQW interference peaks for 1% TEB/III was observed as seen in **Figure 5-11 (a)** when compared to when the sample was grown at 1060°C (as seen in **Figure 5-5**). This indicates that lower growth temperatures appear to be detrimental to the QW and QB interface with the incorporation of BN.

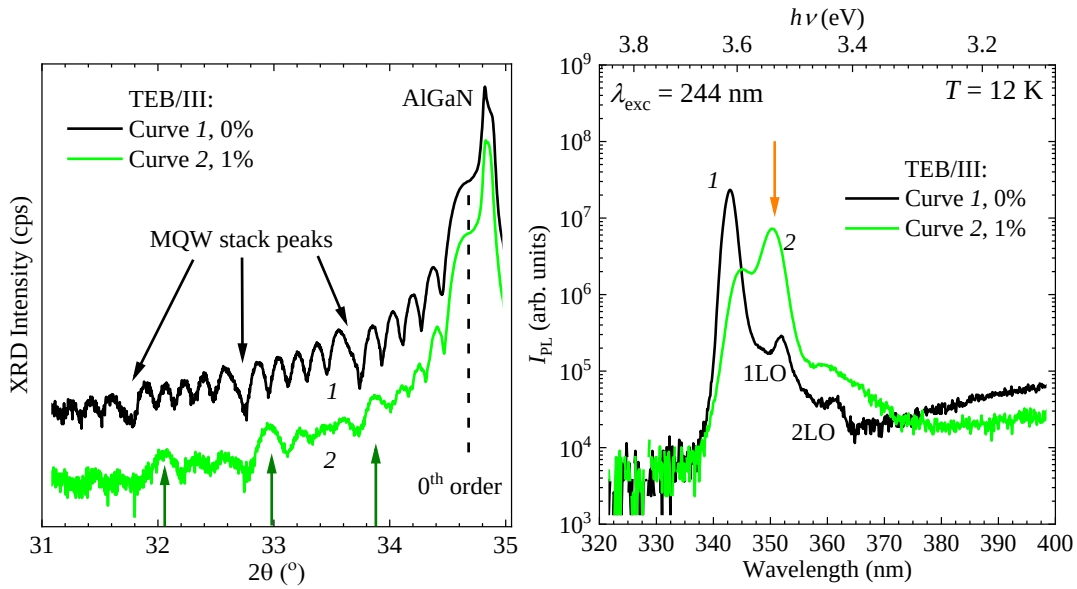

(a) (b)

Figure 5-11. (a) XRD ω-2θ (0002) scan and (b) RT PL for BGaN/AlGaN grown at 960°C and N_2 carrier gas

As seen in **Figure 5-11 (b)**, the PL peak position of our reference sample is located at a shorter wavelength compared to the "1%" sample, similar to our previous results. We believe that the second peak appearing for the TEB/III 1% sample at 3.54 eV (denoted by the orange arrow), may again be associated with isolated B atoms. Within small variations, this peak is present in all of our ternary samples regardless of the choice of temperature or carrier gas used further highlighting the incorporation of B at such low concentrations resulting in isolated atoms forming some sort of radiative defect centres.

5.1.4 Comparison with simulation work

From the simulation results in **Section 2.5**, an emission wavelength of 363 nm was obtained for a SQW of $B_{0.01}Ga_{0.99}N$/ $Al_{0.15}Ga_{0.85}N$. However, the emission wavelength from our LT PL results contained a shorter emission wavelength.

The difference in the experimental and theoretical results can arise due to a number of reasons. In our theoretical work, a SQW of BGaN/ AlGaN was analysed, which was compared to a 5 MQW structure in our experimental work. MQW and SQW structures differ in terms of carrier confinement[225], carrier localisation[226], strain distribution[227] etc. Further to this, the exact B incorporation in the 5 MQW structure is unknown, so we are assuming that the TEB/III flow is directly proportional to the boron incorporation.

A lack of bowing parameters in literature for the various polarisation components (P_{sp}, e_{31}, e_{33}), elastic constants (C_{13}, C_{33}) etc. will have an impact on the overall result. Our simulation results do not consider Stokes shift in the material. It is known that the band-gap energy determined from either PL or cathodoluminescence is subject to the effects of Stokes shift as compared to other spectroscopy techniques such as optical absorption, reflectance or transmission. This shifting gives rise to an underestimation of the band gap energy for a known composition.[228–231]

Further to this, it has been seen in literature that incorporation of BN with III-Nitride materials results in the clustering of boron atoms resulting in localization effects[232,233] which was not accounted for in our one-dimensional simulations. As a result, this local strain effect can incorporate local polarisation fields[34]. This is similarly seen with clustering of In-rich regions in InGaN alloys which makes the determination of the energy gap quite difficult.[48,234,235] The impact of B clustering is currently under intensive investigation by the group Schulz et al.[232,233] at Tyndall National Institute and the nature of this clustering can lead to significant effects.

5.1.5 Discussion on bandgap bowing parameter

In the case of the B containing samples grown under both N_2 and H_2 conditions, an initial improvement in PL intensity is observed for the “0.3%” and “1%” samples along

with a redshift, similar to what is seen in the literature[236]. Changes in the PL of the "3%" sample, are more radical: spectra further redshift however intensity drops significantly while FWHMs increase drastically. As previously seen by XRD analysis, this is caused by significant damage to the overall MQW stack structure.

For this reason, these samples along with the samples grown at 960°C were excluded from the estimation of *apparent* (since actual B incorporation in the solid is unknown) bandgap bowing parameters *b* which we found using **Equation 5-1** to be 13.5 eV and 12.4 eV for the H_2 and N_2 samples respectively, based on the reference (0%), "0.3%" and "1%".

$$E_g^{B_xGa_{1-x}N} = E_g^{BN}x + E_g^{GaN}(1-x) - bx(1-x) \qquad 5\text{-}1$$

An E_g^{BN} value of 13.2 eV[25] was used along with a value of 3.7 eV or 3.58 eV used for E_g^{GaN} for growth under H_2 and N_2 respectively. This value is much larger than the predicted theoretically for BGaN[25] where an initial redshift (in the bandgap energy) is not predicted. These values should be used with caution, as the exact B incorporation in our MQW stack is unknown and boron is a difficult material to detect by standard experimental procedure due to its small atomic size e.g. secondary ion mass spectroscopy.

5.1.6 Discussion on the internal quantum efficiency

Based on the PL data above, the apparent IQE values were summarised for all of the samples, determined as ratios between their RT and LT PL peak intensities as seen in **Figure 5-12**, due to the difficulty in acquiring the FWHM for some of the samples and thus unable to acquire accurate integrated intensity values.

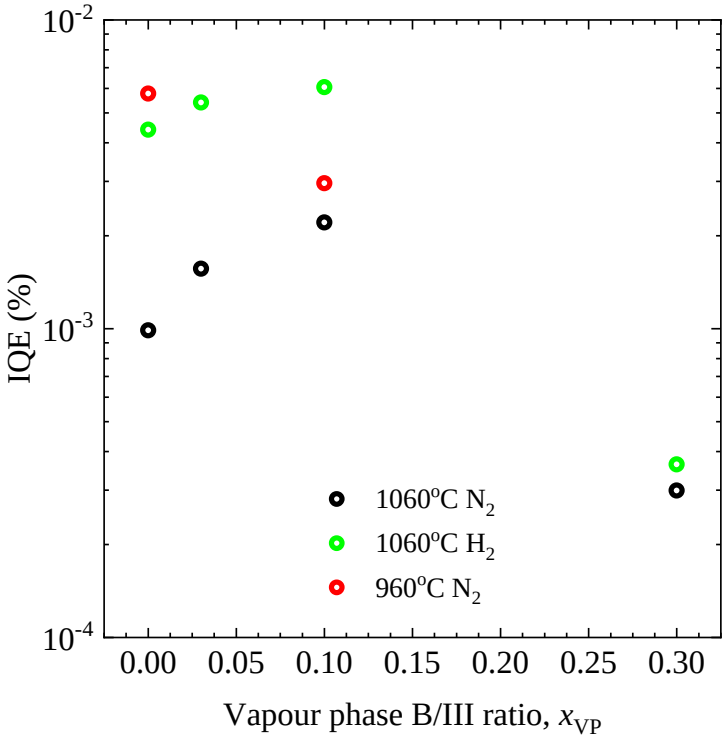

Figure 5-12. Internal quantum efficiency for BGaN/AlGaN

Assuming that light extraction efficiencies do not depend much on B incorporation and growth parameters used, to minimise error in IQE estimation our brightest sample at LT (TEB/III<1%, 1060°C growth temperature and H_2 carrier gas) was considered to have 100% efficiency while others were recalculated accordingly.

As it is seen from **Figure 5-12**, for all samples grown with a low TEB/III ratio (i.e. containing "1% and <1%) and at a growth temperature of 1060°C, the introduction of boron results in an IQE improvement while it somewhat decreases for the samples grown at lower temperatures (960°C). This is similarly seen in InGaN QW systems[237–240].

From the results, it is clear that for TEB/III $\leq$ 1% an improvement was observed in the IQE for all the samples however in the case of the 3% sample an intensity drop was observed. This intensity drop was expected due to the disruption between QW and QB interface as seen by XRD in **Figure 5-5** and **Figure 5-11** indicating a reduction in carrier confinement.

5.2 Growth and characterisation of quaternary BAlGaN MQW stack

In this section, to try and remove the pitting effect seen on the surface of our ternary BGaN MQW samples a small amount of Al was incorporated into the QW region to create a quaternary alloy to try and prevent the nanomasking/ nanoetching effect, as Al atoms are "sticky" at this temperature. Based on our literature review, this appears to be the first report on the growth and characterisation of a quaternary BAlGaN/AlGaN MQWs on a *c*-plane sapphire substrate where the boron-containing structures are directly compared to a non-boron containing reference sample grown in otherwise identical conditions.

5.2.1 Experimental growth of BAlGaN MQW structure

A schematic of the structure can be seen in **Figure 5-13** which is similar to that of the MQW ternary samples as seen in **Figure 5-1**, however, a low Al content is incorporated into the QWs. The five MQW quaternary samples were again grown with a $\frac{\text{TEB}}{\text{III}}$ ratio of <1%, 1% and 3% along with a growth temperature of 1060°C and H_2 carrier gas. An $Al_{0.05}Ga_{0.95}N/Al_{0.15}Ga_{0.85}N$ reference sample was also grown for comparison.

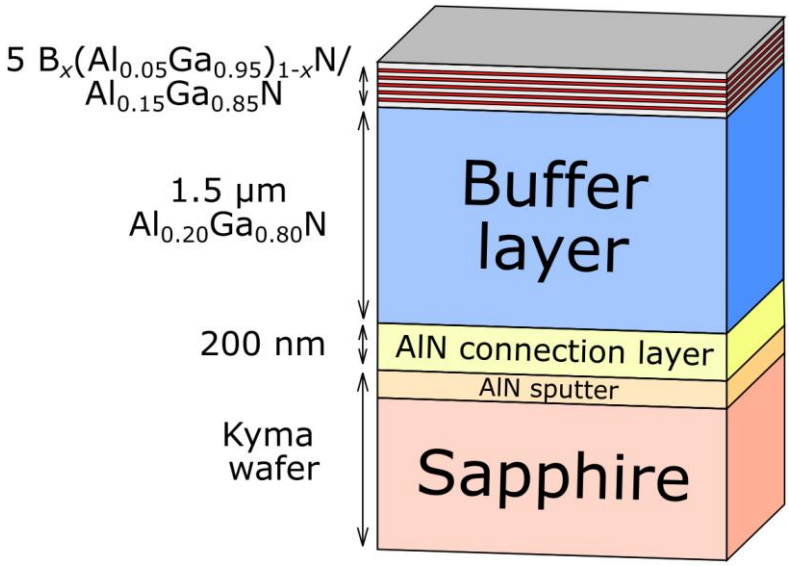

Figure 5-13. Schematic of $B_x(Al_{0.05}Ga_{0.95})_{1-x}N$/ $Al_{0.15}Ga_{0.85}N$ quaternary MQW stack grown by MOCVD

5.2.2 Surface and structural quality

A relatively smooth surface was observed for the reference sample as seen in **Figure 5-14 (a)**, however, for the samples grown with the smallest TEB/III ratio of ≤1%, the surface becomes heavily pitted, as seen in **Figure 5-14 (b)**.

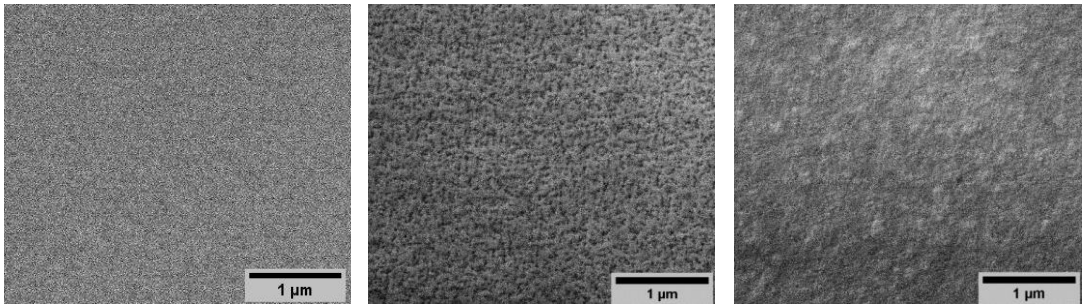

(a) (b) (c)

Figure 5-14. SEM surface morphology for samples with (a) TEB/III = 0%, (b) TEB/III < 1% and (c) TEB/III = 3%

A similar surface morphology was observed for the quaternary samples with the incorporation of boron to that of the ternary samples. The 1% sample had a similar surface morphology, while a further increase in the TEB/III ratio to 3% resulted in the disappearance of these pits, but the surface remained significantly roughened, as shown in **Figure 5-14 (c)**.

XRD results for the BAlGaN/ AlGaN samples are presented in **Figure 5-15**.

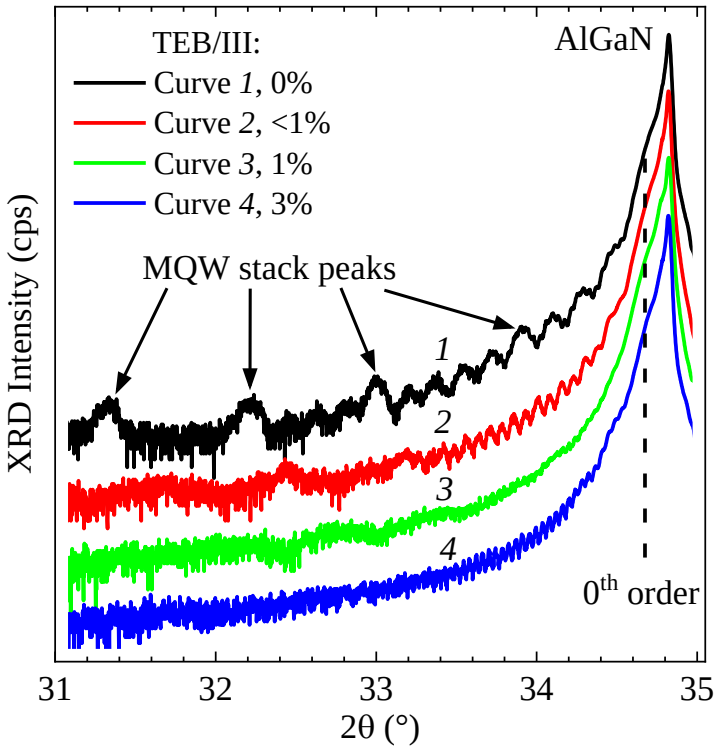

Figure 5-15. ω-2θ (0002) scan for (B)AlGaN/ AlGaN MQW

For the reference sample (Curve *1*), clear XRD features related to both the full MQW stack and individual QW+QB periods were observed, indicating the presence of relatively sharp and smooth QW/QB interfaces within the MQW stack. With increasing boron content, the satellite peaks associated with the MQW stack degrade and ultimately disappear, indicating that some disruption to the periodic structure of the MQW stack may be occurring, which may be related to the pits and roughening structure observed in SEM.

To further investigate the impact of B on the MQW structure, the "<1%" and "3%" samples were selected for TEM analysis. As seen in **Figure 5-16 (a)**, for the <1% sample, the quantum wells are locally smooth, but are separated by voids in which the deposition appears "blocked".

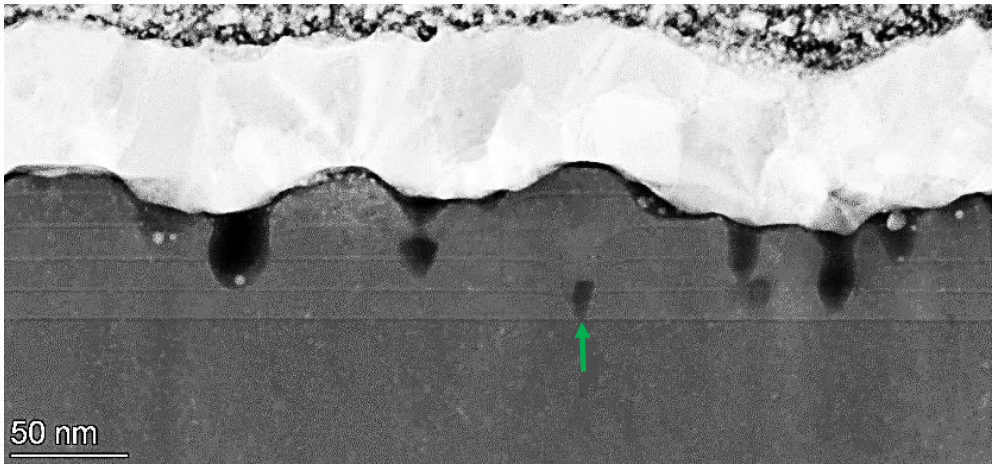

(a)

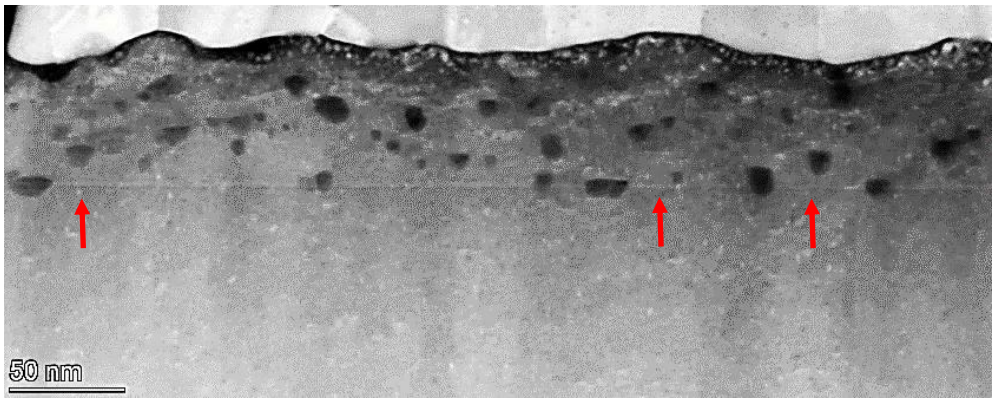

(b)

Figure 5-16. HAADF-STEM cross-section of MQW stack for samples with (a) TEB/III <1% and (b) TEB/III = 3%

This suggests that the incorporation of BN results in some form of nanomasking effect under the growth conditions used and in some regions overgrowth can also be seen (as indicated by the green arrow), which results in the formation of nanovoids in the material. One possible mechanism for this is that wherever a cluster of boron or BN forms, then they would prevent GaN growth around this region and act as a repellent for other group III atoms. This was not expected as Al adatoms are much "stickier" than Ga (only 5% of them during QW growth), however, it was still not enough to prevent the nanomasking effect from occurring. Partial coalescence did occur during the barrier growth (resulting in some of the voids being completely encapsulated),

however, some of the "nanomasking" features propagated up to the surface of the material and resulted in the pits also observed by SEM (**Figure 5-14 (b)**).

With increasing B content, the probability of nanomasking increases so that the resulting nanovoids have much higher density, with smaller dimensions, as seen by TEM for the 3% sample (**Figure 5-16 (b)**). This nanomasking was observed throughout the sample, completely disrupting the MQW stack so that only the first QW can be seen in this case. Due to the smaller void size, it appears easier to coalesce them during QB growth which explains the lack of pits seen on the surface of this sample (**Figure 5-14 (c)**). The strong disruption of the MQW stack observed explains the complete disappearance of the MQW-related features in the XRD ω-2θ scan for the highest B content sample (Curve *4* in **Figure 5-15**).

A further interesting observation for the "3%" sample is that voids propagate beneath even the first QW i.e. even before B was introduced into the reactor (indicated by arrows in **Figure 5-16 (b)**). From this, we conclude that not only nanomasking but also nanoetching can occur at higher TEB flows. This is interesting in itself as it is known that, unlike GaN, AlGaN is a challenging material to deliberately induce in-situ etching[241]. One possibility is that the BN and hydrogen are creating a type of etchant for AlGaN which could also be used in several applications. Further work will be required to investigate the feasibility of this approach to operate in a controlled manner.

Kimura *et al*.[242] have observed a similar growth mechanism as seen in **Figure 5-17**. They suggest that the incorporation of BN with GaN can lead to the introduction of v-pits followed by nanopipe formation, and as the material grows thicker overgrowth results in elongated nanovoids along the *c*-direction forming in their material. They suggest that boron acts as a surfactant, reducing the surface energy of the semi-polar $(10\bar{1}1)$ and nonpolar $(101\bar{0})$ planes to below that of the polar *c*-plane (0001).

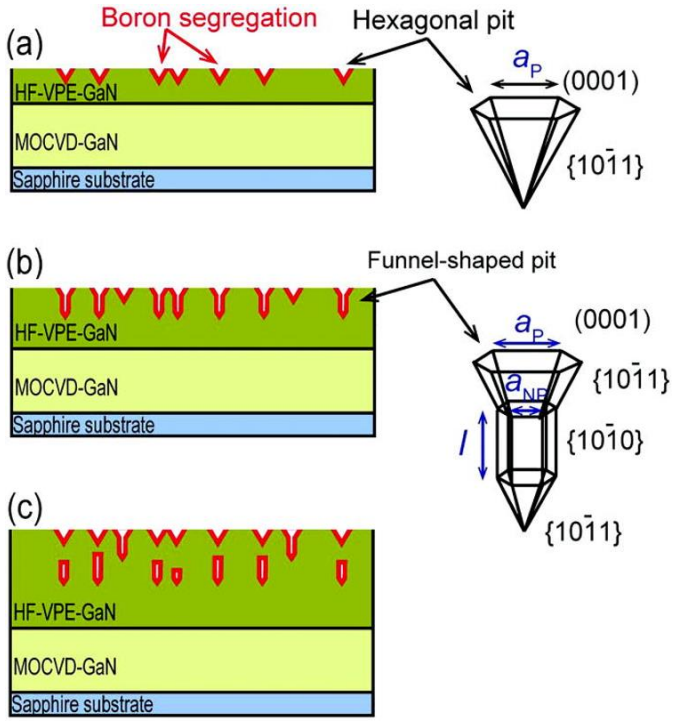

Figure 5-17. Diagram showing the proposed nanopipe formation mechanism. The surface in red represents the one-monolayer boron segregated surfaces (a) Hexagonal pit formation due to boron impurity segregation, (b) funnel-shaped pit formation from the hexagonal pits and (c) nanopipes embedded by overgrowth above the bottom portion of the funnel-shaped pits[242]

In our growth, such development of these defects into crystallographically shaped v-pits does not occur and were not expected since B is supplied only during the relatively short QW growth (~2 nm). Nevertheless, some of the voids show signatures of this process, as their bottoms have slanted facets and almost vertical sidewalls (**Figure 5-16 (a)**). We did not observe V-pits on the surface (**Figure 5-14 (a)**) as our samples are capped with a non-B-containing AlGaN QB, during the growth of which the effect of B is expected to gradually diminish. Therefore, what we observe in **Figure 5-14** is an incomplete coalescence of nanopipes/ nanovoids initiated during the QW growth.

It has also been reported in literature that low boron contents result in the presence of cubic BGaN forming in the material.[186,243] A difference in the cubic zincblende and hexagonal wurtzite crystal structure exists in their stacking sequence as previously discussed in **Section 1.3.1**. Difference in stacking sequence can be identified from fast Fourier transform (FFT) patterns[244–246]. FFT patterns were measured for the

TEB/III<1% sample in the QB region (which was assumed to contain the wurtzite structure) and the nanopipe region in our material as seen in **Figure 5-18**.

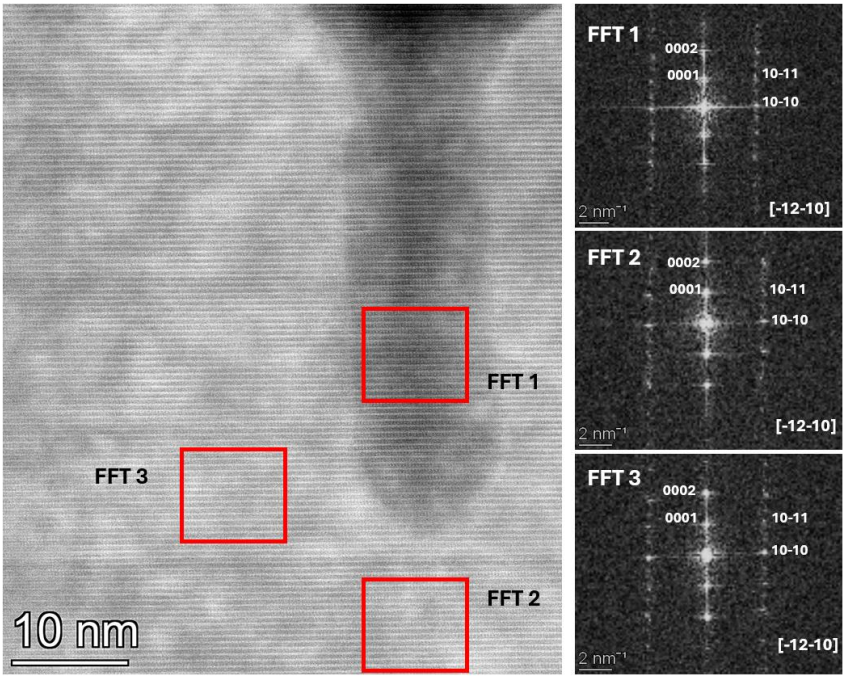

Figure 5-18. FFT pattern analysis of nanopipes for TEB/III < 1%

The different sampling area FFT scans are denoted as *FFT 1*, *FFT 2* and *FFT 3*. The results indicate that the material is wurtzite throughout as the pattern is the same in all scans.

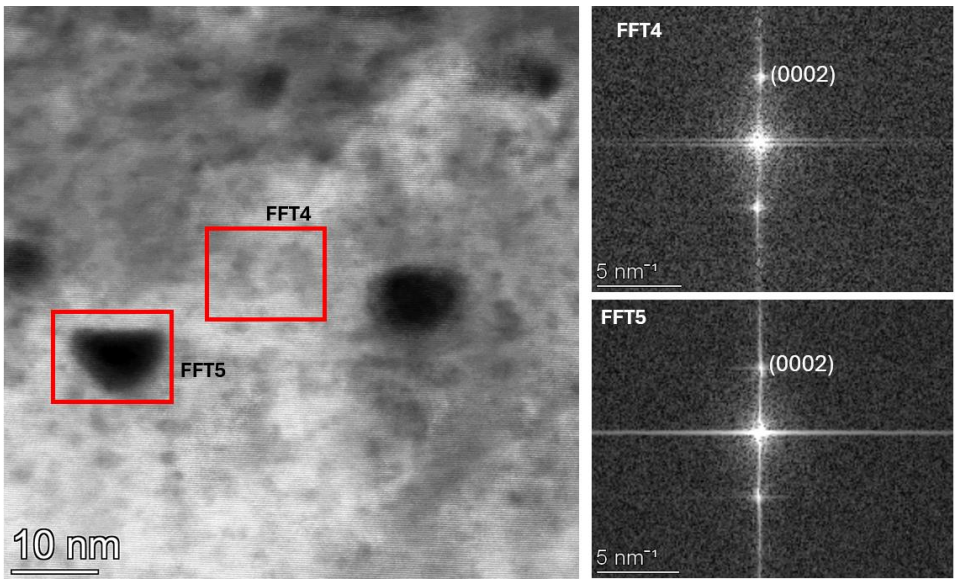

Figure 5-19. FFT pattern analysis of nanovoids for TEB/III = 3% samples

Similarly, FFT patterns were obtained for the TEB/III =3% sample inside and outside the nanovoid regions as seen in **Figure 5-19**. As seen from the FFT4 and FFT5 pattern no difference was observed indicating that a wurtzite material is present.

It is difficult to determine whether boron is all incorporating into the lattice of the material. However, it is clear that boron is incorporating into the material. A similar LED structure was grown by Milner *et al*.[247] in our group where the incorporation of B into the material is evident from the secondary ion mass spectrometry (SIMS) results. A cumulative effect is observed with the incorporation of B into the QW with an initial concentration of 1% and rising to a value of 2.3% in the final well. In the QB region the boron content is evident, decaying slowly without the flow of TEB. Orsal *et al*.[248] reported a similar surface accumulation behaviour with the growth of BGaN layers. It is still unclear whether the boron is incorporated into the alloy and future work will be required. Although the x-ray evidence from the thicker single layers clearly indicate that a significant fraction of the boron will do so. To fully understand this, future work using techniques such as Atom Probe Tomography[249,250] will be required.

5.2.3 Spectroscopy results for BAlGaN MQW samples

As seen by the RT PL spectra in **Figure 5-20 (a),** the reference sample exhibits a single near band edge peak at 329 nm, which we attribute to the QWs, with an additional broad peak in the visible observed around 520 nm (not shown), associated with deep level defect emission from the structure.

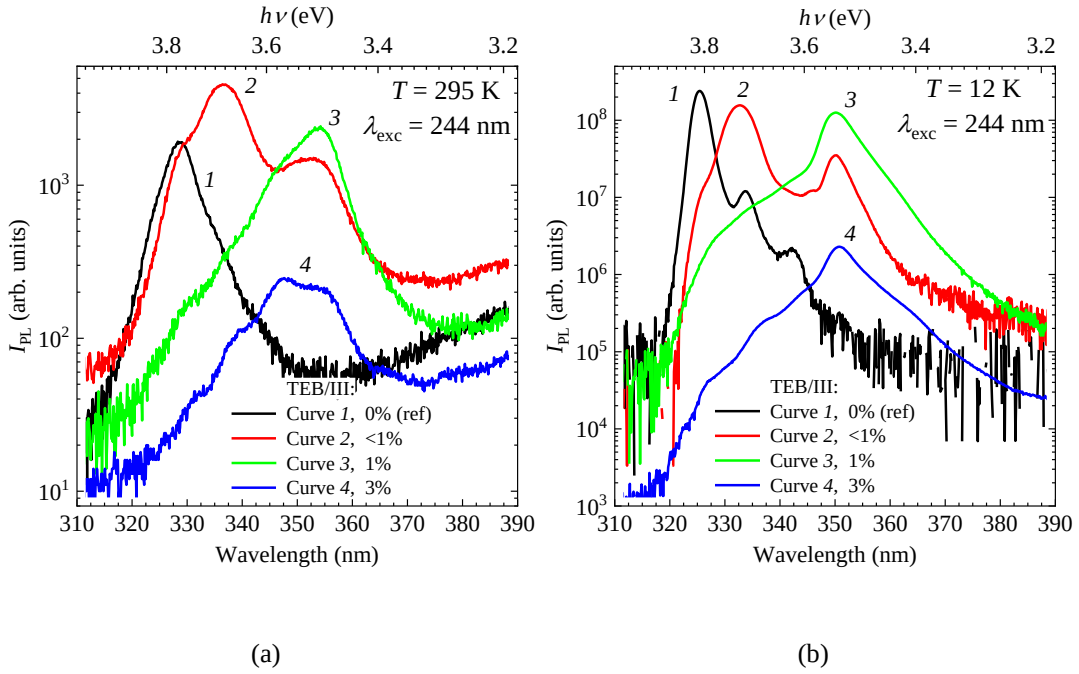

(a) (b)

Figure 5-20. Photoluminescence spectrum from MQW stack at (a) RT and (b) LT

In our PL analysis, we initially focus on the main MQW-related peak in the near UV. The introduction of the smallest amounts of BN (<1% sample) resulted in a significant change in the emission spectrum. The main peak is redshifted by 8 nm (90 meV) with a shoulder aligned with the MQW peak of the reference sample. In addition to this, a new peak appears at 354 nm. The 1% sample peaks at 354 nm at RT, while with the 3% sample, this peak somewhat blueshifts to 350 nm. The coinciding (in wavelength) of the 350-354 nm peak in all three samples is very visible, particularly in the LT spectra presented in **Figure 5-20 (b)**. This may indicate that this peak is not composition-dependent but perhaps can be attributed to some sort of luminescence centres associated with boron in the AlGaN matrix. It is worth noting that a large bandgap bowing parameter is predicted for both BGaN and BAlN as previously seen in **Figure 1-8**, and therefore it is reasonable to expect similar behaviour in our B-containing quaternary alloy. The main (dominant) peak in the <1% sample seems to be near band edge emission in the BAlGaN QWs and so the observed redshift for our reference sample may stem from a larger bandgap bowing parameter than theoretically predicted[24,25].

A proposed possible arrangement to explain the PL is as follows. For low B incorporation (TEB/III<1%), the QW material in between the nanovoid regions acts like a quaternary alloy. A large number of carriers can recombine before meeting and being captured by the near bandedge "centre" associated with boron producing the PL band at 337 nm. Those that interact with the deeper possible iso-electronic trap[251] like boron centre, lead to the emission peak at 354 nm.

For the 1% sample, the bandgap energy may shrink further, however, the localised isoelectronic state remains in a fixed position. In principle, as the B content increases the probability of meeting these B localised centres increases drastically for carriers resulting in a single peak in RT PL and a band-to-band transition only appearing as a high-energy shoulder. For the highest B incorporation sample, the spectra are rather similar in form to the 1% case, but with lower intensity. This may be due to the disruption to the sample of the quantum wells (only one left) for example.

Further to the PL, the samples were also characterised by PLE measured at low temperatures (12 K). For detection, deep-level defect (DLD) emission in the visible (~520 nm) was chosen to have more complete and unbiased (by stray light) information about the absorption edge in the UV. PL spectra, normalised by the intensity of the defect peak measured with excitation wavelengths in the range of 305-325 nm (varied for different samples), are presented in **Figure 5-21 (a)**. The corresponding PLE spectra (also normalised) depicted in **Figure 5-21 (b)** are characterised by the following features:

(i) a slight decrease in the DLD emission intensity below 4.05 eV (above 307 nm) which corresponds to the onset of transparency in the *n*-AlGaN buffer;
(ii) this is then followed by an intensity increase below 4 eV (above 310 nm) due to the vanishing of absorption in the AlGaN barriers in the MQW stack;
(iii) finally, after reaching the maximum in the 3.88-3.76 eV (320-330 nm) region, the PLE intensity diminishes as less light is absorbed by QWs themselves.

It is, therefore, reasonable to conclude that even though a very similar band is present in our bare *n*-AlGaN template (not shown), the DLD peak in these MQW samples at least partly originates from the QWs themselves.

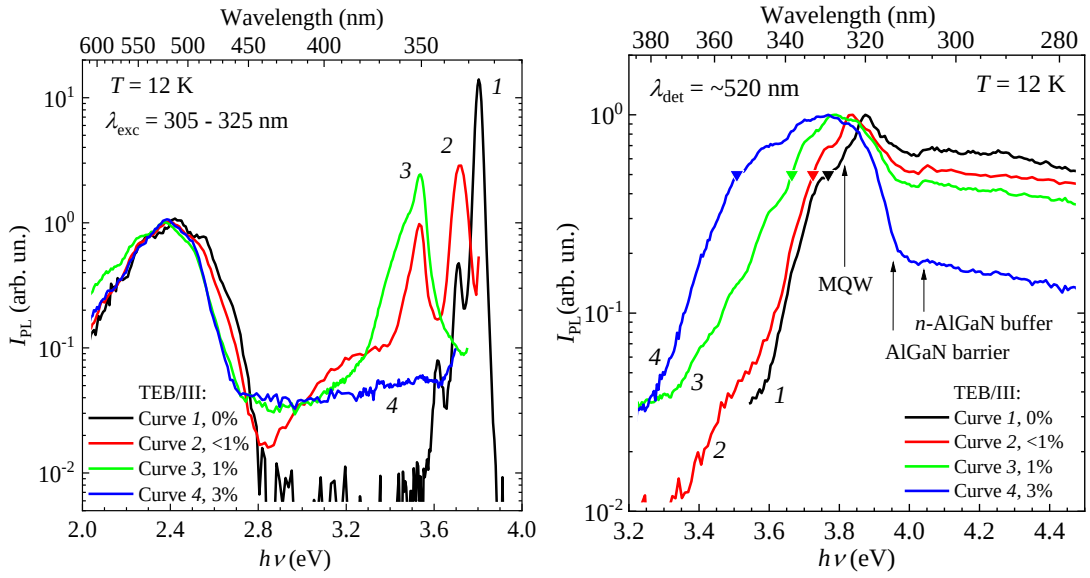

Figure 5-21. Normalised LT PL (a) and PLE (b) spectra (using Xe lamp excitation)

Two significant features from the PLE spectra are worth discussing. First, the MQW-related absorption edge is found to redshift with higher B incorporation. This would indicate a high bandgap bowing parameter associated with quaternary alloys containing BN leading to a redshift rather than blueshift of the absorption edge[236]. Second, the increase of the DLD peak in the transparency range of QBs (> 315 nm, < 3.95 eV) indicates that carriers are not efficiently transferred from the barriers to the QWs and as a result, the barriers are effectively acting as optical filters. The increasing effect of this optical filter correlates with B incorporation and can be understood in relation to the TEM data presented above. For samples with higher B content, only a fraction of the QWs survive due to the nanovoid formation and this fraction is higher for QWs closer to the substrate. In the extreme case of the 3% sample, only the first QW remains and all other barriers and wells act as an optical filter seemingly without contributing to the DLD peak. This explains the highest decrease of intensity in the PLE spectrum for the 3% sample, coming from the spectral range where the QB is transparent (~ 3.7 eV) to the range where it has full absorption (~ 3.95 eV).

The coloured triangles in **Figure 5-21 (b)**, mark the wavelengths at which the PLE spectrum drops to half of its initial intensity from the QW maximum. This can be used

as a rough estimation of the effective bandgap energy $(E_{g,eff})$[252] for the QWs. These are plotted against the B/III vapour phase ratio in **Figure 5-22**.

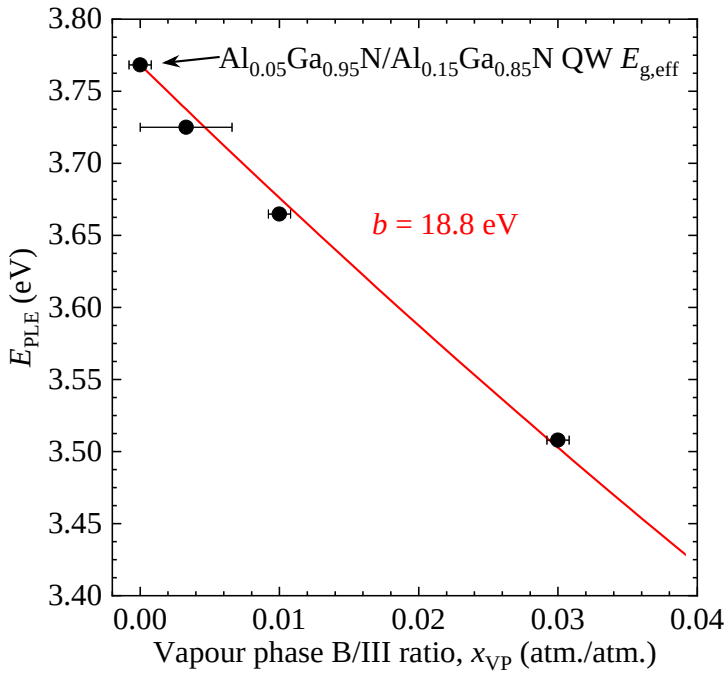

Figure 5-22. Effective bandgap of $B_x(Al_{0.05}Ga_{0.95})_{1-x}N/Al_{0.15}Ga_{0.85}N$ MQWs versus vapour phase B/III ratio used during QW growth.

The solid red line represents the best fit using the standard formula with the bandgap bowing parameter (**Equation 5-2**).

$$E_g^{B_x(Al_{0.05}Ga_{0.95}N)_{1-x}} = E_g^{BN}x + E_g^{Al_{0.05}Ga_{0.95}N}(1-x) - bx(1-x) \qquad 5\text{-}2$$

A theoretical value of 13.2 eV[25] and our experimental value of 3.76 eV were used for the AlGaN and BN endpoints leaving b as the only free parameter for the fitting. Based on the experimental data, a value of b = 18.8 eV can be estimated when plotted against the B/III gas phase ratio. This value is at least two times higher than the predicted theoretically for BGaN[25] where an initial redshift (in the bandgap energy) is not predicted. However, this value needs to be used with caution as the actual B content in our material is not known. Considering the fragmental nature of our MQWs, it is difficult to estimate using standard methods like secondary ion mass spectroscopy. Large bowing parameters in systems with potential miscibility

issues are well known and data in different composition ranges can also show different values due to composition-dependent effects such as in InAlN for example[36]. Such effects are known in the BGaN system, though conducting such an analysis here would require more information on the precise B content in the QWs.

5.2.4 Conclusion

We believe that the incorporation of BN results in some of the atoms forming into a conventional quaternary and ternary alloy, whereas the other atoms form clusters which passivate the material preventing the growth of (Al)GaN and thus resulting in nanovoids forming in the material. At higher B content, along with passivation, a nanoetching effect also occurs leading to back etching below the QW region i.e. impacting regions grown before the introduction of TEB in the reactor.

The growth of the ternary MQW stack with low B incorporation shows an improvement in PL without severe degradation of the QW and QB interfaces. Signatures of what we believe to be radiative recombination defect centres associated with isolated B atoms in (Al)GaN matrix are observed in the PL of all our samples as a redshifted relative to band edge emission peak (~350 nm).

From our PL and PLE characterisation of the quaternary structure, a multiband behaviour was observed and a possible mechanism to explain it was proposed. From the redshift of the absorption edge (as determined from PLE) with the incorporation of B, a high bandgap bowing parameter *b* of the order of 19 eV was estimated, however, this value should be used with caution as we assumed the B/III as ratio as an indicator of BN incorporation in the QWs.

Despite the experimentally observed improvement in PL properties for low B-containing samples, the overall B effect was proven detrimental to the periodic structure of the MQW stack. Taking this into account, the problem of nanomasking and severe disruption of the quantum wells still needs to be addressed by perhaps an investigation of a wider space of growth parameters before the potential of wz-BN-containing alloys can reach their full potential in UV-LEDs.

CONCLUSION AND FUTURE WORK

In the previous five chapters of this thesis, the incorporation of WZ-BN with III-Nitride materials has been discussed from both a theoretical and experimental aspect.

- The theoretical work showed that caution should be used when working with polarisation constants associated with B-III-N materials. Low Al incorporation in the QB along with low B incorporation in the QW appears to improve the wavefunction overlap.
- From the experimental work, a method to identify the clustering of boron atoms in BGaN thin layers is proposed. Further to this MQW of B(Al)GaN/ AlGaN showed an initial improvement in the emission intensity along with a redshift with the incorporation of boron at the cost of nanovoids/ nanopits forming in the material.

Due to the novelty of WZ-BN, there are many areas in both the experimental and theoretical literature still untouched.

The implementation of different growth temperatures for the QW and QB (more commonly known as flow-modulated epitaxy) of the MQW stack region could play a key role in obtaining nano-void-free BGaN. Growth of the AlGaN barriers at a more favourable high temperature of around 1100-1200°C and lowering QW growth to ~800°C could prevent the clustering of B atoms. If the nanomasking is inherent to the incorporation of WZ-BN then a thin capping layer of high Al content above the QW region could potentially prevent the nanomasking effect from propagating into the QB region and thus improve carrier confinement in the active region.

An alternative method to try and prevent the nanomasking effect with the incorporation of WZ-BN and still obtain emission in the UV region (with the possibility of deeper UV emission), could be the research into InAlN due to the lower growth temperature of <800°C[253]. Lower growth temperatures are more optimum for InN and could play a key role in the improved incorporation of B with III-N materials.

Another possible route for B containing III-N materials would be focusing on the visible region and the growth of BInN or BInGaN to improve red LEDs' efficiency.

Further work on the theoretical side can be completed using a 3D simulation software package to implement the clustering of boron atoms for a BAlGaN/ BInAlN/ BInGaN MQW structure to see the impact the isolated boron atoms have on the charge density of the material. Further to this, reports in the literature suggest the possibility of type-II band alignment with the incorporation of B-III-N materials[75].

While the positive effect of low boron incorporation on the PL intensity of our samples is promising, the problem of nanomasking still needs to be addressed by perhaps an investigation of wider space of growth parameters before potential of B in optoelectronic applications can be fully unravelled.

APPENDIX

Finite difference method

The finite difference method (FDM) is a numerical analysis technique used for solving differential equations through the process of discretization[254,255]. FDM can be used to solve a single particle in a box problem as seen in **Equation 0-1** by discretising the problem as seen in **Figure 0-1**.

$$-\frac{h^2}{2m}\frac{d^2\Psi}{dx^2} + V(x)\Psi(x) = E\Psi(x) \qquad 0\text{-}1$$

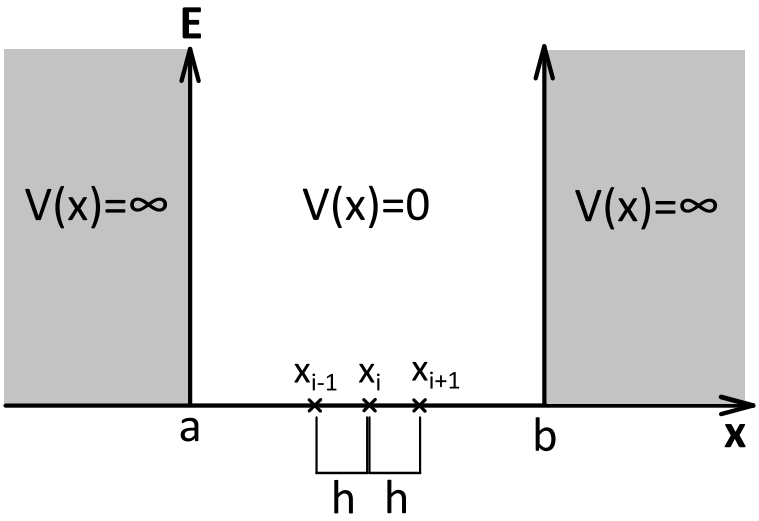

Figure 0-1. Discretization of a particle in a box

Solving the equation in the region $x \in [a, b]$, with N+1 grid points and $x_o = a$ and $x_N = b$, then the boundary conditions are $\Psi_o = 0$ and $\Psi_N = 0$. The spacing between intervals is denoted by $h = \frac{b-a}{N+1}$ with the mesh points $x_i = a + ih$ where $i = 0,1, \ldots, N+1$. This method works by replacing derivative terms in the equation with finite difference approximations as seen in **Equation 0-2**.

$$\frac{d\Psi}{dx} = \frac{\Psi(x+h) - \Psi(x-h)}{2h} = \frac{\Psi(x_{i+1}) - \Psi(x_{i-1})}{2h}$$

$$\frac{d^2\Psi}{dx^2} = \frac{\Psi(x+h) - 2\Psi(x) + \Psi(x-h)}{h^2} = \frac{\Psi(x_{i+1}) - 2\Psi(x) + \Psi(x_{i-1})}{h^2} \qquad 0\text{-}2$$

By solving the equation above and rewriting it in matrix notation, the results can be seen in **Equation 0-3**. By diagonalizing the matrix, both the eigenvectors and eigenvalues can then be obtained.

$$\frac{1}{h^2}\begin{pmatrix} -2 & 1 & 0 & 0 & \dots & 0 \\ 0 & 1 & -2 & 1 & \dots & 0 \\ 0 & 0 & 1 & -2 & \dots & 0 \\ \vdots & \vdots & \vdots & \vdots & \ddots & 1 \\ 0 & 0 & 0 & 1 & -2 & 1 \\ 0 & 0 & 0 & 0 & 1 & -2 \end{pmatrix} \begin{pmatrix} \Psi_1 \\ \Psi_2 \\ \vdots \\ \vdots \\ \Psi_{N-1} \\ \Psi_N \end{pmatrix} = E \begin{pmatrix} \Psi_1 \\ \Psi_2 \\ \vdots \\ \vdots \\ \Psi_{N-1} \\ \Psi_N \end{pmatrix} \qquad 0\text{-}3$$

Main Parameters

Table 0-1. Summary of the main parameters used

	AlN	GaN	BN
a/ Å	3.112[30]	3.189[30]	2.534[29]
c/ Å	4.982[30]	5.185[30]	4.189[29]
E_g/ eV	6.23[30]	3.51[30]	13.2[25]
E_{vb}/ eV	0.8[30]	0[30]	1.02[69,70]
m_h	-	1.876[97]	-
m_e	-	0.209[97]	-
C_{13}/ Pa	108[30]	106[30]	64[29]
C_{33}/ Pa	373[30]	398[30]	1113[29]
P_{sp}^{ZB}/ C·m^{-2}	-0.090[80]	-0.035[80]	-0.012[69,70]
e_{31}^{prop}/ C·m^{-2}	-0.676[80]	-0.551[80]	0.282[69,70]
P_{sp}^{Href}/ C·m^{-2}	1.351[80]	1.312[80]	2.174[69,70]
e_{31}^{imp}/ C·m^{-2}	-2.027[80]	-1.863[80]	-1.892
e_{33}/ C·m^{-2}	1.569[80]	1.020[80]	-1.068[69,70]
$a_c^{\parallel}$/ eV	-	-9.5[53]	-
$a_c^{\perp}$/ eV	-	-8.2[53]	-

d_1/ eV	-	-3.7[48]	-
d_2/ eV	-	4.5[48]	-
d_3/ eV	-	8.2[48]	-
d_4/ eV	-	-4.1[48]	-
d_5/ eV	-	-4.0[48]	-
ϵ	8.5[115]	9.6[115]	6.65[116]

REFERENCES

1. *UV LEDS and UV Lamps – Market & Technology Trends 2021 Report*. (2021).
2. *III-Nitride Ultraviolet Emitters: Technology and Applications*. vol. 227 (Springer International Publishing, Cham, 2016).
3. Marcu, L., French, P. M. & Elson, D. S. *Fluorescence Lifetime Spectroscopy and Imaging: Principles and Applications in Biomedical Diagnostics*. (CRC press).
4. Davitt, K. *et al.* 290 and 340 nm UV LED arrays for fluorescence detection from single airborne particles. *Opt. Express* **13**, 9548–9555 (2005).
5. Parbrook, P. J. & Wang, T. Light emitting and laser diodes in the ultraviolet. *IEEE J. Sel. Top. Quantum Electron.* **17**, 1402–1411 (2011).
6. Parrish, J. A. Phototherapy and photochemotherapy of skin diseases. *J. Invest. Dermatol.* **77**, 167–171 (1981).
7. Hockberger, P. E. A history of ultraviolet photobiology for humans, animals and microorganisms. *Photochem. Photobiol.* **76**, 561–579 (2002).
8. Schreiner, M. *et al.* UV-B-induced secondary plant metabolites-potential benefits for plant and human health. *Crit. Rev. Plant Sci.* **31**, 229–240 (2012).
9. Song, K., Mohseni, M. & Taghipour, F. Application of ultraviolet light-emitting diodes (UV-LEDs) for water disinfection: A review. *Water Res.* **94**, 341–349 (2016).
10. Hijnen, W. A. M., Beerendonk, E. F. & Medema, G. J. Inactivation credit of UV radiation for viruses, bacteria and protozoan (oo)cysts in water: A review. *Water Res.* **40**, 3–22 (2006).

11. Founders, B. D. White paper Blu-ray Disc Format, 1. A Physical Format Specifications for BD-RE. at (2004).

12. Wei, P., Li, B., de Leon, A. & Pentzer, E. Beyond binary: optical data storage with 0, 1, 2, and 3 in polymer films. *J Mater Chem C* **5**, 5780–5786 (2017).

13. Li, Y. *et al.* High-efficiency near-UV light-emitting diodes on Si substrates with InGaN/GaN/AlGaN/GaN multiple quantum wells. *J. Mater. Chem. C* **8**, 883–888 (2020).

14. Steigerwald, D. A. *et al.* Illumination with solid state lighting technology. *IEEE J. Sel. Top. Quantum Electron.* **8**, 310–320 (2002).

15. Rass, J. & Lobo-Ploch, N. Optical polarization and light extraction from UV LEDs. *III-Nitride Ultrav. Emit. Technol. Appl.* 137–170 (2016).

16. Lide, D. R. *CRC Handbook of Chemistry and Physics*. vol. 85 (CRC press, 2004).

17. Yu, J. *et al.* Influence of dislocation density on internal quantum efficiency of GaN-based semiconductors. *AIP Adv.* **7**, (2017).

18. Yu, J. *et al.* Erratum:“Influence of dislocation density on internal quantum efficiency of GaN-based semiconductors”[AIP Advances 7, 035321 (2017)]. *AIP Adv.* **7**, (2017).

19. Huang, S.-C., Tu, P.-M., Yang, S.-K., Lin, Y.-W. & Hsu, C.-P. High performance 375 nm ultraviolet InGaN/AlGaN light-emitting diodes by using a heavily Si-doped GaN growth mode transition layer. in *Gallium Nitride Materials and Devices VII* vol. 8262 314–320 (SPIE, 2012).

20. Wang, T. *et al.* Fabrication of high performance of AlGaN/GaN-based UV light-emitting diodes. *J. Cryst. Growth* **235**, 177–182 (2002).

21. Watson-Parris, D. *et al.* Carrier localization mechanisms in InxGa1-xN/GaN quantum wells. *Phys. Rev. B—Condensed Matter Mater. Phys.* **83**, 115321 (2011).

22. Chichibu, S. F. *et al.* Origin of defect-insensitive emission probability in In-containing (Al, In, Ga) N alloy semiconductors. *Nat. Mater.* **5**, 810–816 (2006).

23. Ioannou, D. E. & Davidson, S. M. Diffusion length evaluation of boron-implanted silicon using the SEM-EBIC/Schottky diode technique. *J. Phys. Appl. Phys.* **12**, 1339 (1979).

24. Shen, J.-X., Wickramaratne, D. & Van de Walle, C. G. Band bowing and the direct-to-indirect crossover in random BAlN alloys. *Phys. Rev. Mater.* **1**, 065001 (2017).

25. Turiansky, M. E., Shen, J.-X., Wickramaratne, D. & Van de Walle, C. G. First-principles study of bandgap bowing in BGaN alloys. *J. Appl. Phys.* **126**, 095706 (2019).

26. Shatalov, M. *et al.* Performance and applications of deep UV LED. *Int. J. High Speed Electron. Syst.* **21**, 1250011 (2012).

27. Available online: https://commons.wikimedia.org/wiki/File:Wurtzite_polyhedra.png.

28. Ren, C. Polarisation fields in III-nitrides: effects and control. *Mater. Sci. Technol.* **32**, 418–433 (2016).

29. Sheerin, T. P. & Schulz, S. Strain Effects in Wurtzite Boron Nitride: Elastic Constants, Internal Strain, and Deformation Potentials from Hybrid Functional Density Functional Theory. *Phys. Status Solidi RRL – Rapid Res. Lett.* **16**, 2200021 (2022).

30. Caro, M. A., Schulz, S., Healy, S. B. & O'Reilly, E. P. Built-in field control in alloyed c-plane III-N quantum dots and wells. *J. Appl. Phys.* **109**, 084110 (2011).

31. Monavarian, M., Rashidi, A. & Feezell, D. A Decade of Nonpolar and Semipolar III-Nitrides: A Review of Successes and Challenges. *Phys. Status Solidi A* **216**, 1800628 (2019).

32. Feneberg, M., Leute, R. A., Neuschl, B., Thonke, K. & Bickermann, M. High-excitation and high-resolution photoluminescence spectra of bulk AlN. *Phys. Rev. B* **82**, 075208 (2010).

33. Yan, Q. *et al.* Band parameters and strain effects in ZnO and group-III nitrides. *Semicond. Sci. Technol.* **26**, 014037 (2011).

34. Caro, M. A., Schulz, S. & O'Reilly, E. P. Theory of local electric polarization and its relation to internal strain: Impact on polarization potential and electronic properties of group-III nitrides. *Phys. Rev. B* **88**, 214103 (2013).

35. Coughlan, C., Schulz, S., Caro, M. A. & O'Reilly, E. P. Band gap bowing and optical polarization switching in Al1−xGaxN alloys. *Phys. Status Solidi B* **252**, 879–884 (2015).

36. Alam, S. N., Zubialevich, V. Z., Ghafary, B. & Parbrook, P. J. Bandgap and refractive index estimates of InAlN and related nitrides across their full composition ranges. *Sci. Rep.* **10**, 16205 (2020).

37. Vurgaftman, I., Meyer, J. R. & Ram-Mohan, L. R. Band parameters for III–V compound semiconductors and their alloys. *J. Appl. Phys.* **89**, 5815–5875 (2001).

38. Levinshtein, M. *Handbook Series on Semiconductor Parameters*. vol. 1 (World Scientific, 1997).

39. Vegard, L. The constitution of the mixed crystals and the space filling of the atoms. *J. Phys.* **5**, 17–26 (1921).

40. Morkoç, H. *Handbook of Nitride Semiconductors and Devices, Electronic and Optical Processes in Nitrides*. (John Wiley & Sons, 2009).

41. Rathinasabapathy, S., Santhosh, M. & Asokan, M. Significance of boron nitride in composites and its applications. *Recent Adv. Boron-Contain. Mater.* 63 (2020).

42. Polyakov, A. Y. *et al.* Growth of GaBN ternary solutions by organometallic vapor phase epitaxy. *J. Electron. Mater.* **26**, 237–242 (1997).

43. Amano, H. *et al.* The 2020 UV emitter roadmap. *J. Phys. Appl. Phys.* **53**, 503001 (2020).

44. Lambrecht, W. R., Limpijumnong, S., Rashkeev, S. & Segall, B. Electronic band structure of SiC polytypes: a discussion of theory and experiment. *Phys. Status Solidi B* **202**, 5–33 (1997).

45. Setyawan, W. & Curtarolo, S. High-throughput electronic band structure calculations: Challenges and tools. *Comput. Mater. Sci.* **49**, 299–312 (2010).

46. Volm, D. *et al.* Exciton fine structure in undoped GaN epitaxial films. *Phys. Rev. B* **53**, 16543 (1996).

47. Piprek, J. *Nitride Semiconductor Devices: Principles and Simulation*. (John Wiley & Sons, 2007).

48. Vurgaftman, I. & Meyer, J. R. Band parameters for nitrogen-containing semiconductors. *J. Appl. Phys.* **94**, 3675–3696 (2003).

49. Electronic Band Structure and Polarization Effects. in *Handbook of Nitride Semiconductors and Devices* 131–321 (John Wiley & Sons, Ltd, 2008). doi:https://doi.org/10.1002/9783527628438.ch2.

50. Hopfdeld, J. Fine structure in the optical absorption edge of anisotropic crystals. *J. Phys. Chem. Solids* **15**, 97–107 (1960).

51. Kirilyuk, V. *Optical Characterization of Gallium Nitride*. ([Sl: sn], 2002).

52. Strite, a S. & Morkoç, H. GaN, AlN, and InN: a review. *J. Vac. Sci. Technol. B Microelectron. Nanometer Struct. Process. Meas. Phenom.* **10**, 1237–1266 (1992).

53. Fonoberov, V. A. & Balandin, A. A. Excitonic properties of strained wurtzite and zinc-blende GaN/AlxGa1−xN quantum dots. *J. Appl. Phys.* **94**, 7178–7186 (2003).

54. Taniyasu, Y., Kasu, M. & Makimoto, T. Radiation and polarization properties of free-exciton emission from AlN (0001) surface. *Appl. Phys. Lett.* **90**, (2007).

55. Banal, R. G., Funato, M. & Kawakami, Y. Optical anisotropy in [0001]-oriented Alx Ga1−xN / AlN quantum wells (x > 0.69). *Phys. Rev. B* **79**, 121308 (2009).

56. Kolbe, T. *et al.* Optical polarization characteristics of ultraviolet (In)(Al)GaN multiple quantum well light emitting diodes. *Appl. Phys. Lett.* **97**, 171105 (2010).

57. Kawanishi, H., Senuma, M. & Nukui, T. Anisotropic polarization characteristics of lasing and spontaneous surface and edge emissions from deep-ultraviolet

(λ≈240nm) AlGaN multiple-quantum-well lasers. *Appl. Phys. Lett.* **89**, 041126 (2006).

58. Netzel, C., Knauer, A. & Weyers, M. Impact of light polarization on photoluminescence intensity and quantum efficiency in AlGaN and AlInGaN layers. *Appl. Phys. Lett.* **101**, 242102 (2012).

59. Varshni, Y. P. Temperature dependence of the energy gap in semiconductors. *physica* **34**, 149–154 (1967).

60. Teisseyre, H. *et al.* Temperature dependence of the energy gap in GaN bulk single crystals and epitaxial layer. *J. Appl. Phys.* **76**, 2429–2434 (1994).

61. Petalas, J., Logothetidis, S., Boultadakis, S., Alouani, M. & Wills, J. Optical and electronic-structure study of cubic and hexagonal GaN thin films. *Phys. Rev. B* **52**, 8082 (1995).

62. Shan, W. *et al.* Temperature dependence of interband transitions in GaN grown by metalorganic chemical vapor deposition. *Appl. Phys. Lett.* **66**, 985–987 (1995).

63. Salvador, A. *et al.* Properties of a Si doped GaN/AlGaN single quantum well. *Appl. Phys. Lett.* **67**, 3322–3324 (1995).

64. Nepal, N., Li, J., Nakarmi, M., Lin, J. & Jiang, H. Temperature and compositional dependence of the energy band gap of AlGaN alloys. *Appl. Phys. Lett.* **87**, (2005).

65. Guo, Q. G. Q. & Yoshida, A. Y. A. Temperature dependence of band gap change in InN and AlN. *Jpn. J. Appl. Phys.* **33**, 2453 (1994).

66. Jiang, L., Shen, W., Ogawa, H. & Guo, Q. Temperature dependence of the optical properties in hexagonal AlN. *J. Appl. Phys.* **94**, 5704–5709 (2003).

67. Nam, K., Li, J., Lin, J. & Jiang, H. Optical properties of AlN and GaN in elevated temperatures. *Appl. Phys. Lett.* **85**, 3489–3491 (2004).

68. Berland, K. *et al.* Temperature stability of intersubband transitions in AlN/GaN quantum wells. *Appl. Phys. Lett.* **97**, (2010).

69. Dreyer, C. E., Lyons, J. L., Janotti, A. & Van de Walle, C. G. Corrigendum: "Band alignments and polarization properties of BN polymorphs" [Appl. Phys. Express 7 031001 (2014)]. *Appl. Phys. Express* **13**, 019301 (2020).

70. Dreyer, C. E., Lyons, J. L., Janotti, A. & Van de Walle, C. G. Band alignments and polarization properties of BN polymorphs. *Appl. Phys. Express* **7**, 031001 (2014).

71. AlQatari, F. *et al.* Detailed band alignment of high-B-composition BGaN with GaN and AlN. *J. Phys. Appl. Phys.* **56**, (2023).

72. Mickevičius, J. *et al.* Type-II band alignment of low-boron-content BGaN/GaN heterostructures. *J. Phys. Appl. Phys.* **52**, 325105 (2019).

73. Sholl, D. S. & Steckel, J. A. *Density Functional Theory: A Practical Introduction*. (John Wiley & Sons, 2022).

74. Kohn, W. & Sham, L. Density functional theory. in *Conference Proceedings-Italian Physical Society* vol. 49 561–572 (Editrice Compositori, 1996).

75. Sulami, A. A., Alqatari, F. & Li, X. Band alignments of emerging wurtzite BAlN and BGaN semiconductors. *ArXiv Prepr. ArXiv200508407* (2020).

76. Ota, Y., Imura, M., Banal, R. G. & Koide, Y. Natural band alignment of BAlN and BGaN alloys. *J. Phys. Appl. Phys.* **55**, 455102 (2022).

77. Miller, D. A. B. *et al.* Band-Edge Electroabsorption in Quantum Well Structures: The Quantum-Confined Stark Effect. *Phys. Rev. Lett.* **53**, 2173–2176 (1984).

78. Costales, A., Blanco, M. A., Martín Pendás, Á., Kandalam, A. K. & Pandey, R. Chemical bonding in group III nitrides. *J. Am. Chem. Soc.* **124**, 4116–4123 (2002).

79. Ambacher, O. *et al.* Pyroelectric properties of Al (In) GaN/GaN hetero-and quantum well structures. *J. Phys. Condens. Matter* **14**, 3399 (2002).

80. Dreyer, C. E., Janotti, A., Van de Walle, C. G. & Vanderbilt, D. Correct Implementation of Polarization Constants in Wurtzite Materials and Impact on III-Nitrides. *Phys. Rev. X* **6**, 021038 (2016).

81. Wood, C. & Jena, D. *Polarization Effects in Semiconductors: From Ab Initio Theory to Device Applications*. (Springer Science & Business Media, 2007).

82. Morkoç, H., Morkoc, H. & Morkoc, H. *Nitride Semiconductor Devices : Fundamentals and Applications*. (John Wiley & Sons, Incorporated, Weinheim, GERMANY, 2013).

83. Trampert, A., Brandt, O. & Ploog, K. Crystal structure of group III-nitrides, Vol. 50 of Semiconductors and Semimetals. at (1998).

84. Reed-Hill, R. E., Abbaschian, R. & Abbaschian, R. *Physical Metallurgy Principles*. vol. 17 (Van Nostrand New York, 1973).

85. Gröger, R., Leconte, L. & Ostapovets, A. Structure and stability of threading edge and screw dislocations in bulk GaN. *Comput. Mater. Sci.* **99**, 195–202 (2015).

86. Nagakubo, A., Ogi, H., Sumiya, H., Kusakabe, K. & Hirao, M. Elastic constants of cubic and wurtzite boron nitrides. *Appl. Phys. Lett.* **102**, 241909 (2013).

87. Kim, D. Y. *et al.* Overcoming the fundamental light-extraction efficiency limitations of deep ultraviolet light-emitting diodes by utilizing transverse-magnetic-dominant emission. *Light Sci. Appl.* **4**, e263–e263 (2015).

88. Park, S.-H. High-efficiency BAlGaN/AlN quantum well structures for optoelectronic applications in ultraviolet spectral region. *Opt Express* **23**, 3623–3629 (2015).

89. Park, S.-H. & Ahn, D. Theoretical Studies on TM-Polarized Light Emission for Ultraviolet BAlGaN/AlN Optoelectronic Devices. *IEEE Photonics Technol. Lett.* **28**, 2153–2155 (2016).

90. Park, S.-H., Hong, W.-P., Kim, J.-J., Kim, B.-H. & Ahn, D. High-efficiency BGaN/AlN quantum wells for optoelectronic applications in ultraviolet spectral region. in *2017 International Conference on Numerical Simulation of Optoelectronic Devices (NUSOD)* 77–78 (IEEE, Copenhagen, Denmark, 2017). doi:10.1109/NUSOD.2017.8009999.

91. Xing, Z., Wang, F., Wang, Y., Liou, J. J. & Liu, Y. Enhanced performance in deep-ultraviolet laser diodes with an undoped BGaN electron blocking layer. *Opt. Express* **30**, 36446 (2022).

92. Abid, M. *et al.* Blue–violet boron-based Distributed Bragg Reflectors for VCSEL application. *J. Cryst. Growth* **315**, 283–287 (2011).

93. AlQatari, F. *et al.* Lattice-matched III-nitride structures comprising BAlN, BGaN, and AlGaN for ultraviolet applications. *Mater. Res. Express* **8**, 086202 (2021).

94. Winkelnkemper, M., Schliwa, A. & Bimberg, D. Interrelation of structural and electronic properties in InxGa1−xN ⁄ GaN quantum dots using an eight-band k · p model. *Phys. Rev. B* **74**, 155322 (2006).

95. Chaudhuri, D. *et al*. Multiscale simulations of the electronic structure of III-nitride quantum wells with varied indium content: Connecting atomistic and continuum-based models. *J. Appl. Phys.* **129**, (2021).

96. Adachi, S. III-V ternary and quaternary compounds. *Springer Handb. Electron. Photonic Mater*. 1–1 (2017).

97. Schulz, S. *et al.* Electronic and optical properties of nonpolar a-plane GaN quantum wells. *Phys. Rev. B* **82**, 125318 (2010).

98. Cheng, K.-Y. *III–V Compound Semiconductors and Devices*. (Springer, 2020).

99. Tanner, D. S. P. A study of the elastic and electronic properties of III-nitride semiconductors. (University College Cork, 2017).

100. Yan, Q., Rinke, P., Janotti, A., Scheffler, M. & Van de Walle, C. G. Effects of strain on the band structure of group-III nitrides. *Phys. Rev. B* **90**, 125118 (2014).

101. Dreyer, C., Janotti, A. & Van de Walle, C. Effects of strain on the electron effective mass in GaN and AlN. *Appl. Phys. Lett.* **102**, (2013).

102. Boresi, A. P. & Schmidt, R. J. *Advanced Mechanics of Materials*. (John Wiley & Sons, 2002).

103. Slaughter, W. S. *The Linearized Theory of Elasticity*. (Springer Science & Business Media, 2012).

104. Voigt, W. *Textbook of Crystal Physics: (Excluding Crystal Optics)*. vol. 34 (BG Teubner, 1910).

105. Povolotskyi, M., Auf der Maur, M. & Di Carlo, A. Strain effects in freestanding three-dimensional nitride nanostructures. *Phys. Status Solidi C* **2**, 3891–3894 (2005).

106. Schulz, S., Caro, M. A., Coughlan, C. & O'Reilly, E. P. Atomistic analysis of the impact of alloy and well-width fluctuations on the electronic and optical properties of InGaN/GaN quantum wells. *Phys. Rev. B* **91**, 035439 (2015).

107. Shimada, K., Sota, T. & Suzuki, K. First-principles study on electronic and elastic properties of BN, AlN, and GaN. *J. Appl. Phys.* **84**, 4951–4958 (1998).

108. Kim, K., Lambrecht, W. R. & Segall, B. Elastic constants and related properties of tetrahedrally bonded BN, AlN, GaN, and InN. *Phys. Rev. B* **53**, 16310 (1996).

109. Karch, K. & Bechstedt, F. Ab initio lattice dynamics of BN and AlN: Covalent versus ionic forces. *Phys Rev B* **56**, 7404–7415 (1997).

110. Levinshtein, M. E., Rumyantsev, S. L. & Shur, M. S. *Properties of Advanced Semiconductor Materials: GaN, AIN, InN, BN, SiC, SiGe*. (John Wiley & Sons, 2001).

111. Liu, K. *et al.* Wurtzite BAlN and BGaN alloys for heterointerface polarization engineering. *Appl. Phys. Lett.* **111**, 222106 (2017).

112. Shimada, K. First-principles determination of piezoelectric stress and strain constants of wurtzite III–V nitrides. *Jpn. J. Appl. Phys.* **45**, L358 (2006).

113. Moses, P. G., Miao, M., Yan, Q. & Van de Walle, C. G. Hybrid functional investigations of band gaps and band alignments for AlN, GaN, InN, and InGaN. *J. Chem. Phys.* **134**, 084703 (2011).

114. Yan, Q., Rinke, P., Scheffler, M. & Van de Walle, C. G. Strain effects in group-III nitrides: Deformation potentials for AlN, GaN, and InN. *Appl. Phys. Lett.* **95**, (2009).

115. Patra, S. K. & Schulz, S. Electrostatic built-in fields in wurtzite III-N nanostructures: Impact of growth plane on second-order piezoelectricity. *Phys. Rev. B* **96**, 155307 (2017).

116. Segura, A. *et al.* Nonreversible Transition from the Hexagonal to Wurtzite Phase of Boron Nitride under High Pressure: Optical Properties of the Wurtzite Phase. *J. Phys. Chem. C* **123**, 20167–20173 (2019).

117. Vanderbilt, D. *Berry Phases in Electronic Structure Theory: Electric Polarization, Orbital Magnetization and Topological Insulators*. (Cambridge University Press, 2018).

118. Rabe, K. M., Ahn, C. H. & Triscone, J.-M. *Physics of Ferroelectrics: A Modern Perspective*. vol. 105 (Springer Science & Business Media, 2007).

119. Bernardini, F., Fiorentini, V. & Vanderbilt, D. Spontaneous polarization and piezoelectric constants of III-V nitrides. *Phys. Rev. B* **56**, R10024–R10027 (1997).

120. Bechstedt, F., Grossner, U. & Furthmüller, J. Dynamics and polarization of group-III nitride lattices: A first-principles study. *Phys. Rev. B* **62**, 8003 (2000).

121. Bernardini, F., Fiorentini, V. & Vanderbilt, D. Accurate calculation of polarization-related quantities in semiconductors. *Phys. Rev. B* **63**, 193201 (2001).

122. Schulz, S., Caro, M. A., O'Reilly, E. P. & Marquardt, O. Symmetry-adapted calculations of strain and polarization fields in (111)-oriented zinc-blende quantum dots. *Phys. Rev. B* **84**, 125312 (2011).

123. Ivashchenko, V. I., Turchi, P. E. A., Shevchenko, R. V., Gorb, L. & Leszczynski, J. First-principles investigations of the pressure-induced phase transformations and properties of crystalline and amorphous AlN. *Phys Rev Mater* **4**, 113605 (2020).

124. Martin, R. M. Piezoelectricity. *Phys Rev B* **5**, 1607–1613 (1972).

125. Vanderbilt, D. Berry-phase theory of proper piezoelectric response. *J. Phys. Chem. Solids* **61**, 147–151 (2000).

126. Bonfiglio, A. *et al.* Well-width dependence of the ground level emission of GaN/AlGaN quantum wells. *J. Appl. Phys.* **87**, 2289–2292 (2000).

127. Craven, M., Waltereit, P., Speck, J. & DenBaars, S. Well-width dependence of photoluminescence emission from a-plane GaN/AlGaN multiple quantum wells. *Appl. Phys. Lett.* **84**, 496–498 (2004).

128. Ambacher, O. Growth and applications of group III-nitrides. *J. Phys. Appl. Phys.* **31**, 2653 (1998).

129. Gibart, P. Metal organic vapour phase epitaxy of GaN and lateral overgrowth. *Rep. Prog. Phys.* **67**, 667 (2004).

130. Watson, I. M. Metal organic vapour phase epitaxy of AlN, GaN, InN and their alloys: A key chemical technology for advanced device applications. *Coord. Chem. Rev.* **257**, 2120–2141 (2013).

131. Wang, X. & Yoshikawa, A. Molecular beam epitaxy growth of GaN, AlN and InN. *Prog. Cryst. Growth Charact. Mater.* **48**, 42–103 (2004).

132. Akasaki, I. Key inventions in the history of nitride-based blue LED and LD. *J. Cryst. Growth* **300**, 2–10 (2007).

133. Maruska, H. P. & Rhines, W. C. A modern perspective on the history of semiconductor nitride blue light sources. *Solid-State Electron.* **111**, 32–41 (2015).

134. Puebla, J. Spin phenomena in semiconductor quantum dots. (University of Sheffield, Department of Physics and Astronomy, 2012).

135. Herman, M. A. & Sitter, H. *Molecular Beam Epitaxy: Fundamentals and Current Status*. vol. 7 (Springer Science & Business Media, 2012).

136. Stringfellow, G. B. *Organometallic Vapor-Phase Epitaxy: Theory and Practice*. (Elsevier, 1999).

137. Crawley, J. Thomas Swan engineers for GaN's future. *III-Vs Rev.* **10**, 16–20 (1997).

138. De Croon, M. & Giling, L. Chemical Boundary Layers in CVD: I. Irreversible Reactions. *J. Electrochem. Soc.* **137**, 2867 (1990).

139. Yang, F. H. Modern metal-organic chemical vapor deposition (MOCVD) reactors and growing nitride-based materials. in *Nitride Semiconductor Light-Emitting Diodes (LEDs)* 27–65 (Elsevier, 2014). doi:10.1533/9780857099303.1.27.

140. Thomson, G. W. The Antoine equation for vapor-pressure data. *Chem. Rev.* **38**, 1–39 (1946).

141. Cho, E. *Gallium Nitride Based Heterostructure Growth and Application to Electronic Devices and Gas Sensors*. (University of Michigan, 2009).

142. Stock, A. & Zeidler, F. Zur Kenntnis des Bormethyls und Boräthyls. *Berichte Dtsch. Chem. Ges. B Ser.* **54**, 531–541 (1921).

143. Seshan, K. *Handbook of Thin Film Deposition*. (William Andrew, 2001).

144. Lilja, L. 4H-SiC epitaxy investigating carrier lifetime and substrate off-axis dependence. (Linköping University Electronic Press, 2018).

145. Briot, O., Alexis, J., Tchounkeu, M. & Aulombard, R. Optimization of the MOVPE growth of GaN on sapphire. *Mater. Sci. Eng. B* **43**, 147–153 (1997).

146. Irvine, S. & Capper, P. *Metalorganic Vapor Phase Epitaxy (MOVPE): Growth, Materials Properties, and Applications*. (John Wiley & Sons, 2019).

147. Jones, A. C. & Hitchman, M. L. *Chemical Vapour Deposition: Precursors, Processes and Applications*. (Royal society of chemistry, 2009).

148. Jiang, F. *et al.* Efficient InGaN-based yellow-light-emitting diodes. *Photon Res* **7**, 144–148 (2019).

149. SaifAddin, B. K. *et al.* AlGaN deep-ultraviolet light-emitting diodes grown on SiC substrates. *ACS Photonics* **7**, 554–561 (2020).

150. Kim, J. *et al.* Origins of unintentional incorporation of gallium in InAlN layers during epitaxial growth, part II: Effects of underlying layers and growth chamber conditions. *J. Cryst. Growth* **388**, 143–149 (2014).

151. Mrad, M. *et al.* Understanding and controlling Ga contamination in InAlN barrier layers. *J. Cryst. Growth* **507**, 139–142 (2019).

152. Taylor, E. *et al.* Structural and optical properties of Ga auto-incorporated InAlN epilayers. *J. Cryst. Growth* **408**, 97–101 (2014).

153. Lu, J. *et al.* Charge and mobility enhancements in in-polar InAl(Ga)N/Al(Ga)N/GaN heterojunctions grown by metal-organic chemical vapor deposition using a graded growth strategy. *Japanese Journal of Applied Physics* vol. 51 (2012).

154. Choi, S. *et al.* Origins of unintentional incorporation of gallium in AlInN layers during epitaxial growth, part I: Growth of AlInN on AlN and effects of prior coating. *J. Cryst. Growth* **388**, 137–142 (2014).

155. Zhu, J. J. *et al.* Contribution of GaN template to the unexpected Ga atoms incorporated into AlInN epilayers grown under an indium-very-rich condition by metalorganic chemical vapor deposition (MOCVD). *J. Cryst. Growth* **348**, 25–30 (2012).

156. Smith, M. D. *et al.* Determination of Ga auto-incorporation in nominal InAlN epilayers grown by MOCVD. *J. Mater. Chem. C* **2**, 5787–5792 (2014).

157. Mrad, M. *et al.* Solving the problem of gallium contamination problem in InAlN layers in close coupled showerhead reactors. *Appl. Phys. Express* **12**, 045504 (2019).

158. Deng, G. *et al.* Ga-free AlInN films growth by close-coupled showerhead metalorganic chemical vapor deposition. *Micro Nanostructures* **165**, 207191 (2022).

159. Li, X. *et al.* Large-Area Two-Dimensional Layered Hexagonal Boron Nitride Grown on Sapphire by Metalorganic Vapor Phase Epitaxy. *Cryst. Growth Des.* **16**, 3409–3415 (2016).

160. Kobayashi, Y. & Akasaka, T. Hexagonal BN epitaxial growth on (0001) sapphire substrate by MOVPE. *J. Cryst. Growth* **310**, 5044–5047 (2008).

161. Saito, T. Formation of Sharp Heterojunction Interface Between PSide Waveguide Layer/P-Electron Block Layer of AlGaN Based UV-B Laser Diodes by MOVPE Growth and Its Effect on Device Characteristics. (2024).

162. Ohba, Y. & Hatano, A. A study on strong memory effects for Mg doping in GaN metalorganic chemical vapor deposition. *J. Cryst. Growth* **145**, 214–218 (1994).

163. Xing, H. *et al.* Memory effect and redistribution of Mg into sequentially regrown GaN layer by metalorganic chemical vapor deposition. *Jpn. J. Appl. Phys.* **42**, 50 (2003).

164. Atar, A. Surface dynamics in III-V epitaxy and its device implications. PhD thesis. (University College Cork, 2024).

165. Bragg, W. H. & Bragg, W. L. The reflection of X-rays by crystals. *Proc. R. Soc. Lond. Ser. Contain. Pap. Math. Phys. Character* **88**, 428–438 (1913).

166. Moram, M. A. & Vickers, M. E. X-ray diffraction of III-nitrides. *Rep. Prog. Phys.* **72**, 036502 (2009).

167. Moram, M. A., Vickers, M. E., Kappers, M. J. & Humphreys, C. J. The effect of wafer curvature on x-ray rocking curves from gallium nitride films. *J. Appl. Phys.* **103**, 093528 (2008).

168. Vickers, M. E. *et al.* In-plane imperfections in GaN studied by x-ray diffraction. *J. Phys. Appl. Phys.* **38**, A99 (2005).

169. Kidd, P. XRD of Gallium Nitride and Related Compounds: Strain. *Compos. Layer Thick. Panalytical Almelo 2009* (2009).

170. Kanakamedala, K. Characterization of Tin-Oxide (SnO 2 -Ni) Based Sensors. **9**, 91–100 (2019).

171. Langford, R. M. & Clinton, C. In situ lift-out using a FIB-SEM system. *Micron Oxf. Engl. 1993* **35**, 607–611 (2004).

172. Pennycook, S. J. & Nellist, P. D. *Scanning Transmission Electron Microscopy: Imaging and Analysis*. (Springer Science & Business Media, 2011).

173. Perkowitz, S. *Optical Characterization of Semiconductors: Infrared, Raman, and Photoluminescence Spectroscopy*. (Elsevier, 2012).

174. Guénaud, C. *et al.* Photoluminescence excitation spectroscopy of GaN thin layers as a function of temperature. *Mater. Res. Soc. Internet J. Nitride Semicond. Res.* **2**, e10 (1997).

175. Gautier, S. *et al.* MOVPE growth study of BxGa(1−x)N on GaN template substrate. *Superlattices Microstruct.* **40**, 233–238 (2006).

176. Ebara, K. *et al.* Impact of growth temperature on the structural properties of BGaN films grown by metal-organic vapor phase epitaxy using trimethylboron. *Jpn. J. Appl. Phys.* **58**, SC1042 (2019).

177. Kadys, A. *et al.* Optical and structural properties of BGaN layers grown on different substrates. *J. Phys. Appl. Phys.* **48**, 465307 (2015).

178. Wei, C. H. *et al.* MOCVD growth of GaBN on 6H-SiC (0001) substrates.

179. Gunning, B. P., Moseley, M. W., Koleske, D. D., Allerman, A. A. & Lee, S. R. Phase degradation in BxGa1−xN films grown at low temperature by metalorganic vapor phase epitaxy. *J. Cryst. Growth* **464**, 190–196 (2017).

180. Możdżyńska, E. B. *et al.* Insights on boron impact on structural characteristics in epitaxially grown BGaN. *J. Mater. Sci.* **57**, 7265–7275 (2022).

181. Honda, T. *et al.* Band-Gap Energy and Effective Mass of BGaN. **39**, (2000).

182. Ueyama, K., Mimura, H., Inoue, Y., Aoki, T. & Nakano, T. Effect of substrate offcut angle on BGaN epitaxial growth. *Jpn. J. Appl. Phys.* **55**, 05FD05 (2016).

183. AlQatari, F., Liao, C.-H. & Li, X. Demonstration of MOCVD-grown BGaN with over 10% boron composition. *AIP Adv.* **12**, 085318 (2022).

184. Malinauskas, T. *et al.* Growth of BGaN epitaxial layers using close-coupled showerhead MOCVD: BGaN epitaxial layers by close-coupled showerhead MOCVD. *Phys. Status Solidi B* **252**, 1138–1141 (2015).

185. Zdanowicz, E. *et al.* Boron influence on bandgap and photoluminescence in BGaN grown on AlN. *J. Appl. Phys.* **127**, 165703 (2020).

186. Gautier, S. *et al.* Deep structural analysis of novel BGaN material layers grown by MOVPE. *J. Cryst. Growth* **315**, 288–291 (2011).

187. Cramer, R. C. *et al.* Growth of coherent BGaN films using BBr3 gas as a boron source in plasma assisted molecular beam epitaxy. *J. Vac. Sci. Technol. Vac. Surf. Films* **35**, 041509 (2017).

188. Teles, L. K., Scolfaro, L. M. R., Leite, J. R., Furthmüller, J. & Bechstedt, F. Spinodal decomposition in BxGa1−xN and BxAl1−xN alloys. *Appl. Phys. Lett.* **80**, 1177–1179 (2002).

189. Teles, L. *et al.* Phase separation and gap bowing in zinc-blende InGaN, InAlN, BGaN, and BAlN alloy layers. *Phys. E Low-Dimens. Syst. Nanostructures* **13**, 1086–1089 (2002).

190. Ougazzaden, A. *et al.* BGaN materials on GaN/sapphire substrate by MOVPE using N2 carrier gas. *J. Cryst. Growth* **298**, 316–319 (2007).

191. Akasaka, T. & Makimoto, T. Flow-rate modulation epitaxy of wurtzite AlBN. *Appl Phys Lett*.

192. Li, X. *et al.* 100-nm thick single-phase wurtzite BAlN films with boron contents over 10%. *Phys. Status Solidi B* **254**, 1600699 (2017).

193. Akasaka, T., Kobayashi, Y. & Makimoto, T. BGaN micro-islands as novel buffers for growth of high-quality GaN on sapphire. *J. Cryst. Growth* **298**, 320–324 (2007).

194. Nong, M. *et al.* Epitaxial AlN film with improved quality on Si (111) substrates realized by boron pretreatment via MOCVD. *Appl. Phys. Lett.* **124**, 172107 (2024).

195. Bai, J., Wang, T., Li, H., Jiang, N. & Sakai, S. (0001) oriented GaN epilayer grown on (11$\bar{2}$0) sapphire by MOCVD. *J. Cryst. Growth* **231**, 41–47 (2001).

196. Bai, J., Wang, T., Parbrook, P., Lee, K. & Cullis, A. A study of dislocations in AlN and GaN films grown on sapphire substrates. *J. Cryst. Growth* **282**, 290–296 (2005).

197. Wu, Y. *et al.* Effect of nitridation on polarity, microstructure, and morphology of AlN films. *Appl. Phys. Lett.* **84**, 912–914 (2004).

198. Shibata, T. *et al.* High-quality AlN epitaxial films on (0001)-faced sapphire and 6H-SiC substrate. *Phys. Status Solidi C* 2023–2026 (2003).

199. Paduano, Q. & Weyburne, D. Two-step process for the metalorganic chemical vapor deposition growth of high quality AlN films on sapphire. *Jpn. J. Appl. Phys.* **42**, 1590 (2003).

200. Sakai, M. *et al.* Growth of high-quality GaN films on epitaxial AlN/sapphire templates by MOVPE. *J. Cryst. Growth* **244**, 6–11 (2002).

201. Wang, X. L. *et al.* The effects of LT AlN buffer thickness on the properties of high Al composition AlGaN epilayers. *Mater. Lett.* **60**, 3693–3696 (2006).

202. Luo, W. *et al.* Influence of the nucleation layer morphology on the structural property of AlN films grown on c-plane sapphire by MOCVD. *J. Alloys Compd.* **697**, 262–267 (2017).

203. Balaji, M. *et al.* Effects of AlN nucleation layers on the growth of AlN films using high temperature hydride vapor phase epitaxy. *J. Alloys Compd.* **526**, 103–109 (2012).

204. Bouveyron, R., Mrad, M. & Charles, M. V-pit pinning at the interface of high and low-temperature gallium nitride growth. *Jpn. J. Appl. Phys.* **58**, SC1035 (2019).

205. Schneider, C. A., Rasband, W. S. & Eliceiri, K. W. NIH Image to ImageJ: 25 years of image analysis. *Nat. Methods* **9**, 671–675 (2012).

206. Chen, S.-W., Chang, C.-J. & Lu, T.-C. Effect of strains and v-shaped pit structures on the performance of gan-based light-emitting diodes. *Crystals* **10**, 311 (2020).

207. Kelly, A. & Knowles, K. M. *Crystallography and Crystal Defects*. (John Wiley & Sons, 2020).

208. Son, K. S. *et al.* Formation of V-shaped pits in GaN thin films grown on high temperature GaN. *J. Cryst. Growth* **261**, 50–54 (2004).

209. White, A. H. & Melville, W. The decomposition of ammonia at high temperatures. *J. Am. Chem. Soc.* **27**, 373–386 (1905).

210. Nord, J., Albe, K., Erhart, P. & Nordlund, Kjj. Modelling of compound semiconductors: analytical bond-order potential for gallium, nitrogen and gallium nitride. *J. Phys. Condens. Matter* **15**, 5649 (2003).

211. Schuster, M. *et al.* Determination of the chemical composition of distorted InGaN/GaN heterostructures from x-ray diffraction data. *J. Phys. Appl. Phys.* **32**, A56–A60 (1999).

212. Wallis, D. J., Keir, A. M., Balmer, R. S., Soley, D. E. J. & Martin, T. Composition measurement in strained AlGaN epitaxial layers using x-ray diffraction. *Appl. Phys. Lett.* **85**, 6359–6361 (2004).

213. Wallis, D. J. *et al.* Measuring the composition of AlGaN layers in GaN based structures grown on 150 mm Si substrates using (205) reciprocal space maps. *Semicond. Sci. Technol.* **28**, 094006 (2013).

214. Takano, T., Kurimoto, M., Yamamoto, J. & Kawanishi, H. Epitaxial growth of high quality BAlGaN quaternary lattice matched to AlN on 6H–SiC substrate by LP-MOVPE for deep-UV emission. *J. Cryst. Growth* **237**, 972–977 (2002).

215. Kurimoto, M. *et al.* Growth of BGaN/AlGaN multi-quantum-well structure by metalorganic vapor phase epitaxy. *J. Cryst. Growth* **221**, 378–381 (2000).

216. Yang, F. H. 2 - Modern metal-organic chemical vapor deposition (MOCVD) reactors and growing nitride-based materials. in *Nitride Semiconductor Light-Emitting Diodes (LEDs)* 27–65 (Woodhead Publishing, 2014).

217. Jenkins, F. A. & White, H. E. Fundamentals of optics. *Indian J. Phys.* **25**, 265–266 (1957).

218. Hecht, E. *Optics*. (Pearson Education India, 2012).

219. Amari, H., Ross, I. M., Wang, T. & Walther, T. Characterization of thickness, elemental distribution and band-gap properties in AlGaN/GaN quantum wells by aberration-corrected TEM/STEM. *J. Phys. Conf. Ser.* **371**, 012014 (2012).

220. Takemura, Y., Dosho, S., Konagai, M. & Takahashi, K. Optical properties of ZnSe ZnTe strained layer superlattices prepared by atomic layer epitaxy. *J. Cryst. Growth* **101**, 81–85 (1990).

221. Davies, J. J. Exciton trapping at tellurium iso-electronic centres in ZnSe-ZnTe superlattices. *Semicond. Sci. Technol.* **3**, 219–222 (1988).

222. Dhese, K. *et al.* Interpretation of the temperature-dependent behaviour of the emission from isoelectronic tellurium centres in epitaxial ZnSe1-xTex. *Semicond. Sci. Technol.* **7**, 1210 (1992).

223. Davydov, V. Yu. *et al.* Phonon dispersion and Raman scattering in hexagonal GaN and AlN. *Phys. Rev. B* **58**, 12899–12907 (1998).

224. DEMİR, İ. Growth temperature dependency of high Al content AlGaN epilayers on AlN/Al2O3 templates. *Cumhur. Sci. J.* **39**, 728–733 (2018).

225. Price, P. J. & Stern, F. Carrier confinement effects. *Surf. Sci.* **132**, 577–593 (1983).

226. Frankerl, C. *et al.* Carrier Dynamics in Al-Rich AlGaN/AlN Quantum Well Structures Governed by Carrier Localization. *Phys. Status Solidi B* **257**, 2000242 (2020).

227. Wang, T. *et al.* Effect of strain relaxation and exciton localization on performance of 350-nm AlInGaN quaternary light-emitting diodes. *J. Appl. Phys.* **97**, 083104 (2005).

228. Shan, W. *et al.* Optical properties of InxGa1−xN alloys grown by metalorganic chemical vapor deposition. *J. Appl. Phys.* **84**, 4452–4458 (1998).

229. Wu, J. *et al.* Small band gap bowing in In1−xGaxN alloys. *Appl. Phys. Lett.* **80**, 4741–4743 (2002).

230. Ponce, F. A. *et al.* Microstructure and electronic properties of InGaN alloys. *Phys. Status Solidi B* **240**, 273–284 (2003).

231. Islam, M. R., Kaysir, M. R., Islam, M. J., Hashimoto, A. & Yamamoto, A. MOVPE growth of InxGa1- xN (x 0.4) and fabrication of homo-junction solar cells. *J. Mater. Sci. Technol.* **29**, 128–136 (2013).

232. Nies, C.-L., Sheerin, T. P. & Schulz, S. Electronic and optical properties of boron-containing GaN alloys: The role of boron atom clustering. *APL Mater.* **11**, 091119 (2023).

233. Nies, C.-L. & Schulz, S. Impact of boron atom clustering on the electronic structure of (B, In) N alloys. *ArXiv Prepr. ArXiv240107623* (2024).

234. O'donnell, K., Martin, R. & Middleton, P. Origin of luminescence from InGaN diodes. *Phys. Rev. Lett.* **82**, 237 (1999).

235. Bellaiche, L., Mattila, T., Wang, L.-W., Wei, S.-H. & Zunger, A. Resonant hole localization and anomalous optical bowing in InGaN alloys. *Appl. Phys. Lett.* **74**, 1842–1844 (1999).

236. Jurkevičius, J., Mickevičius, J., Kadys, A., Kolenda, M. & Tamulaitis, G. Photoluminescence efficiency of BGaN epitaxial layers with high boron content. *Phys. B Condens. Matter* **492**, 23–26 (2016).

237. Jones, C. M., Teng, C.-H., Yan, Q., Ku, P.-C. & Kioupakis, E. Impact of carrier localization on recombination in InGaN quantum wells and the efficiency of nitride light-emitting diodes: Insights from theory and numerical simulations. *Appl. Phys. Lett.* **111**, 113501 (2017).

238. McMahon, J. M., Kioupakis, E. & Schulz, S. Atomistic analysis of Auger recombination in c-plane (In,Ga)N/GaN quantum wells: Temperature-dependent competition between radiative and nonradiative recombination. *Phys Rev B* **105**, 195307 (2022).

239. McMahon, J. M., Kioupakis, E. & Schulz, S. Erratum: Atomistic analysis of Auger recombination in c-plane (\mathrmIn,\mathrmGa)\mathrmN/\mathrmGaN

quantum wells: Temperature-dependent competition between radiative and nonradiative recombination [Phys. Rev. B 105, 195307 (2022)]. *Phys Rev B* **108**, 039901 (2023).

240. Barrett, R. M. *et al.* Disentangling the Impact of Point Defect Density and Carrier Localization-Enhanced Auger Recombination on Efficiency Droop in (In,Ga)N/GaN Quantum Wells. *ACS Photonics* **10**, 2632–2640 (2023).

241. Yoshiya, Y., Hoshi, T., Sugiyama, H. & Matsuzaki, H. Impact of selective thermal etching in mixed H2/NH3 atmosphere on crystal quality of AlGaN/GaN heterostructures. *Jpn. J. Appl. Phys.* **60**, SBBK11 (2021).

242. Kimura, T., Aoki, Y., Horibuchi, K. & Nakamura, D. Nanopipe formation as a result of boron impurity segregation in gallium nitride grown by halogen-free vapor phase epitaxy. *J. Appl. Phys.* **120**, 245703 (2016).

243. Bonef, B., Cramer, R., Wu, F. & Speck, J. Correlated Transmission Electron Microscopy and Atom Probe Tomography study of Boron distribution in BGaN. in *Microscopy and Microanalysis* vol. 23 668–669 (2017).

244. Zhou, W. & Greer, H. F. What Can Electron Microscopy Tell Us Beyond Crystal Structures? *Eur. J. Inorg. Chem.* **2016**, 941–950 (2016).

245. Leitherer, A., Yeo, B. C., Liebscher, C. H. & Ghiringhelli, L. M. Automatic identification of crystal structures and interfaces via artificial-intelligence-based electron microscopy. *Npj Comput. Mater.* **9**, 179 (2023).

246. Zhang, Q. *et al.* Selective control of fcc and hcp crystal structures in Au-Ru solid-solution alloy nanoparticles. *Nat. Commun.* **9**, 510 (2018).

247. Milner, P. *et al.* BAlGaN light-emitting diode emitting at 350 nm. *Electron. Lett.* **59**, e12976 (2023).

248. Orsal, G. *et al.* Effect of boron incorporation on growth behavior of BGaN/GaN by MOVPE. *J. Cryst. Growth* **310**, 5058–5062 (2008).

249. Miller, M. K. *Atom Probe Tomography: Analysis at the Atomic Level*. (Springer Science & Business Media, 2012).

250. Kelly, T. F. & Miller, M. K. Atom probe tomography. *Rev. Sci. Instrum.* **78**, (2007).

251. Baldereschi, A. Theory of isoelectronic traps. *J. Lumin.* **7**, 79–91 (1973).

252. Chichibu, S. F., Sota, T., Wada, K., DenBaars, S. P. & Nakamura, S. Spectroscopic Studies in InGaN Quantum Wells. *MRS Internet J. Nitride Semicond. Res.* **4**, 93–105 (1999).

253. Zubialevich, V. Z. *et al.* Enhanced UV luminescence from InAlN quantum well structures using two temperature growth. *J. Lumin.* **155**, 108–111 (2014).

254. Smith, G. D. *Numerical Solution of Partial Differential Equations: Finite Difference Methods*. (Oxford university press, 1985).

255. Thomas, J. W. *Numerical Partial Differential Equations: Finite Difference Methods*. vol. 22 (Springer Science & Business Media, 2013).